SPICAM on Mars Express: Observing modes and overview of UV Spectrometer data and scientific Results

Jean-Loup Bertaux, Oleg Korablev, Séverine Perrier, Eric Quémerais, Franck Montmessin, François Leblanc, Sébastien Lebonnois, Pascal Rannou, Franck Lefèvre, François Forget, et al.

SPICAM on Mars Express: Observing modes and overview of UV spectrometer data and scientific results

Jean-Loup Bertaux,[1,2] Oleg Korablev,[3] Séverine Perrier,[1,2] Eric Quémerais,[1,2] Franck Montmessin,[1,2] F. Leblanc,[1,2] S. Lebonnois,[4] P. Rannou,[1] F. Lefèvre,[1] F. Forget,[4] A. Fedorova,[3] E. Dimarellis,[1,2] A. Reberac,[1,2] D. Fonteyn,[5] J. Y. Chaufray,[1] and S. Guibert[1,6]

Received 30 January 2006; revised 18 April 2006; accepted 8 September 2006; published 28 October 2006.

[1] This paper is intended as an introduction to several companion papers describing the results obtained by the SPICAM instrument on board Mars Express orbiter. SPICAM is a lightweight (4.7 kg) UV-IR dual spectrometer dedicated primarily to the study of the atmosphere of Mars. The SPICAM IR spectrometer and its results are described in another companion paper. SPICAM is the first instrument to perform stellar occultations at Mars, and its UV imaging spectrometer (118–320 nm, resolution ~1.5 nm, intensified CCD detector) was designed primarily to obtain atmospheric vertical profiles by stellar occultation. The wavelength range was dictated by the strong UV absorption of CO_2 ($\lambda < 200$ nm) and the strong Hartley ozone absorption (220–280 nm). The UV spectrometer is described in some detail. The capacity to orient the spacecraft allows a great versatility of observation modes: nadir and limb viewing (both day and night) and solar and stellar occultations, which are briefly described. The absolute calibration is derived from the observation of UV-rich stars. An overview of a number of scientific results is presented, already published or found in more detail as companion papers in this special section. SPICAM UV findings are relevant to CO_2, ozone, dust, cloud vertical profiles, the ozone column, dayglow, and nightglow. This paper is particularly intended to provide the incentive for SPICAM data exploitation, available to the whole scientific community in the ESA data archive, and to help the SPICAM data users to better understand the instrument and the various data collection modes, for an optimized scientific return.

Citation: Bertaux, J.-L., et al. (2006), SPICAM on Mars Express: Observing modes and overview of UV spectrometer data and scientific results, *J. Geophys. Res.*, *111*, E10S90, doi:10.1029/2006JE002690.

1. Introduction

[2] Mars Express is the European Space Agency (ESA) mission aimed to recover most of the science lost with the Proton rocket launch failure in November 1996 of the Russian mission Mars 96, a 4.8 tons space probe aimed at orbiting planet Mars. The Mars Express orbiter (mass 1220 kg) was launched in June 2003 and injected into an elliptical polar orbit around Mars on 25 December 2003, with a pericenter altitude of 259 km, an apocenter altitude of 11,559 km, and a period of 7.57 hr.

[3] On board the Mars 96 Russian mission, the Spectroscopy for the Investigation of the Characteristics of the Atmosphere of Mars (SPICAM) instrument was dedicated to the study of the atmosphere of Mars from top to bottom, in a variety of observing modes, including stellar occultations. The star Spica, when occulted by the Moon in the 18th century, was carefully observed by astronomers: its light decreased abruptly when occulted by the dark limb of the Moon, and it was correctly concluded that there was no atmosphere around the Moon, because otherwise, refraction would have produced a progressive dimming of the star. The SPICAM acronym is a tribute to this early use of stellar occultation.

[4] The SPICAM instrument on board Mars 96 was composed of two instrument packages: one for solar occultations, one for stellar occultations and limb viewing. With the common electronic package, the total mass was 46 kg. Within the much more limited payload mass available on Mars Express, we had to radically change the design of the instrument to get on board. The SPICAM team made a strenuous design effort to propose a new instrument, called SPICAM Light, a 4.7-kg UV-IR instrument dedicated to recover most of the science of the SPICAM/Mars 96. The considerable mass saving from Mars 96 configuration to the new SPICAM Light was achieved by sacrificing all the visible part of the spectrum both in solar and stellar

[1]Université de Versailles Saint-Quentin-UVSQ, Service d'Aéronomie du CNRS/IPSL, Verrières-le-Buisson, France.
[2]Université Pierre et Marie Curie-Paris 6, UMR 7620, Paris, France.
[3]Space Research Institute (IKI), Moscow, Russia.
[4]Laboratoire de Météorologie Dynamique, Paris, France.
[5]Belgian Institute for Space Aeronomy, Brussels, Belgium.
[6]Now at Planetarium de Strasbourg, Strasbourg, France.

0148-0227/06/2006JE002690

occultation sensors, and by suppressing all redundancy between the two sensors. Also, the ability of the Mars Express orbiter to change the orientation and to point in a defined celestial direction makes the use of pointing platforms and devices used on Mars 96 unnecessary. SPICAM Light had been originally proposed including a separate solar occultation IR sensor (SOIR), inherited from so-called solar package of SPICAM/Mars 96. This sensor with a mass of 3.8 kg consisted of a grating spectrometer (1.2–4.8 μm, resolution 0.4–1 nm) for the vertical profiling during solar occultations of H_2O, CO_2, CO, aerosols, and exploration of carbon compounds like methane [*Bertaux et al.*, 2000]. Due to severe mass constraints of the mission this sensor was canceled out of the payload, the scientific recommendation of the selection committee being to include it "...if mass would be available." Mass did not become available. However, during the development phase of SPICAM, we figured out that we could still put, within our mass allocation, an extremely lightweight near-IR spectrometer based on AOTF technology, mainly dedicated to water vapor measurements at 1.38 μm, and designed and fabricated in Russia. ESA accepted the idea, and this new spectrometer was included as a part of SPICAM.

[5] Four other instruments on board Mars Express are also reflown from their Mars 96 counterpart: HRSC, OMEGA, PFS, and ASPERA. These instruments did not change their basic design, while SPICAM made some drastic changes and improvements [*Bertaux et al.*, 2000, 2004]. It is fair to note that PFS, HRSC and OMEGA did change their electronic packages from the elder design of Mars 96, with a mass saving larger than the mass of SPICAM Light (4.7 kg). While the very name of SPICAM Light was to emphasize its small mass, after 2 years of its successful operation in orbit around Mars, we have decided to drop the Light suffix and to call the Mars Express instrument as its older brother: SPICAM.

[6] An overview of a number of scientific results is presented, already published or found in more detail as companion papers in this special section. SPICAM findings are as follows:

[7] 1. The first vertical profiles of density/temperature of CO_2 (20–150 km) obtained ever from a planetary orbiter. About 1 or 2 profiles are obtained each day, with the objective of consolidation of climatic models needed for aerocapture, aerobraking, and EDL (Entry, Descent, Landing).

[8] 2. Numerous vertical profiles of ozone (only one was recorded before by the Phobos 2 mission) and cloud layers.

[9] 3. The systematic measurement of total vertical ozone along track on the dayside, from its UV absorption imprinted in the solar light scattered by the ground and atmosphere, providing the first climatic map of ozone on Mars, for validation of the chemical/transport models.

[10] 4. The discovery of nightglow NO bands in UV and implications for atmospheric transport.

[11] 5. The discovery of auroral activity near the crustal remnant magnetic field, and a thorough study of the ionosphere-upper atmosphere through high-altitude aeronomical observations of O, H, CO, CO^+, and CO_2^+.

[12] 6. The first measurement of H_2O and CO_2 ices UV albedo spectrum.

[13] All these successes are the result of a highly versatile SPICAM instrument, a highly capable spacecraft, and engineers and scientists dedicated to the design, building, testing of the instrument, integration on the spacecraft, and complex operations managed at ESTEC and ESOC. The instrument was built at Service d'Aéronomie du CNRS (France), BIRA (Belgium), and IKI (Russia), with management at Service d'Aéronomie.

[14] In this paper we present an overview of the SPICAM UV spectrometer, the various modes of observations, some statistics on the number of observations, and an aperçu of the main scientific results. These scientific results are discussed separately in much greater detail in several dedicated papers (this special section): the retrieval of occultation data is discussed by *Quémerais et al.* [2006], total ozone mapping is presented by *Perrier et al.* [2006], ozone vertical profiling is discussed by *Lebonnois et al.* [2006], dust and aerosols vertical profiles are discussed by *Montmessin et al.* [2006a], dayglow and nightglow are discussed by *Leblanc et al.* [2006], and dust measurements at limb are discussed by *Rannou et al.* [2006]. The description of the IR AOTF spectrometer, its operation, and overall results are described by *Korablev et al.* [2006]. Water vapor measurements (at 1.38 μm) are presented by *Fedorova et al.* [2006a], while observations of ozone emission at 1.27 μm are discussed by *Fedorova et al.* [2006b].

[15] This paper is organized as follows. First, an overview of SPICAM is presented, with a somewhat detailed description of the UV spectrometer. The various modes of observations are described. Then the in-flight performances are discussed, in terms of pointing, photometric calibration, stray light and dark charge corrections. Nadir looking and limb observations day side and night side are described, followed by star occultations results. The last section is devoted to an overview of SPICAM UV ozone measurements in both nadir and occultation modes.

[16] SPICAM data are fed regularly into the Mars Express (MEX) database in the PDS format (Planetary Data System), accessible to the whole scientific community. This paper is also intended to provide to SPICAM data potential users the necessary background information on the instrument and operations, and to attract them for further analysis of data.

2. SPICAM Instrument Overview and UV Spectrometer Description

[17] The SPICAM instrumentation consists of two blocks: a sensor unit (SU) with a total mass ~3.8 kg, which includes UV (SUV) and Near-IR (SIR) spectrometers, and a simple data processing unit (DPU, 0.9 kg) providing the interface of these two channels with the spacecraft. After the loss of SOIR at selection, both UV and IR channels acquired a solar occultation sounding capability, that helps to partly compensate (in a limited wavelength range) for the loss of the SOIR. Mass, power and telemetry budgets are summarized in Table 1. The optical axis of the SPICAM UV FOV is bore-sight with the other optical instruments (HRSC, OMEGA, PFS), and aligned with +Z axis of the spacecraft, usually maintained directed to nadir for imaging near pericenter.

[18] The summary of the characteristics of the UV spectrometer is given in Table 2. For better efficiency in the UV, the UV spectrometer includes only two reflective surfaces (Figure 1). The light flux is collected by an off-axis

Table 1. Mass, Power, and Telemetry Budgets

	Experiment Unit	Resource
Mass	Electronic block (DPU)	0.9 kg
	Sensor unit (SU)	3.8 kg
	Total	4.7 kg
Power	DPU + SUV	13 W
	DPU + SUV + SIR	18 W
Data volume, per measurement	SUV	3.1 kbit
(1 hz) per orbit	SIR	1.05 kbit
		~5 Mbit

parabolic mirror, which reflects the light toward the entrance of the spectrometer. At its focal plane, a mechanical slit system provides two configurations: with no slit at all, for stellar occultations, and with a slit for extended source observations. The slit is divided into two parts with different widths allowing two spectral resolutions when observing an extended source (Figure 4). The first part (50 μm wide) gives a good resolution with a lower flux; the second part (500 μm) gives more sensitivity at the expense of a coarser spectral resolution. The slit can be completely retracted, creating a hole corresponding to the total useful field of view of $2^\circ \times 3.16^\circ$. This configuration is used in the stellar occultation mode at dark limb when the spectrum of the star is recorded on a few lines of the CCD. The required pointing accuracy is 0.2°, but the actually achieved spacecraft pointing accuracy is often much better on Mars Express (MEX), after accounting for a small mechanical misalignment of SPICAM with XYZ spacecraft axis, that could be measured in flight from stars observations. It has been possible in some occasions to perform stellar occultations within the narrow part of the slit (0.02° wide only), allowing some vertical profiling even on the day side.

[19] A holographic concave toroidal grating from Jobin-Yvon, ion-etched for better efficiency feeds the detection block. The image ratio is ~1, which means that a monochromatic image in the entrance of the spectrometer is conserved in the plane of the detector (Figure 2). The spectral resolution for a point source determined by aberrations is about 1 nm. The CCD detector is a Thomson TH7863 with 288×384 useful pixels and a masked zone of equivalent size. Pixel size is 23 μm $\times$ 23 μm. The detector is electrically cooled to ~0°C, at this temperature the dark current equals 800 electrons per pixel per second, or a few ADU only at switch on, with a subsequent increase with time. By means of custom-made fiber optics the CCD is coupled with the output window of the image intensifier (from Hamamatsu, type 200M). A solar blind CsTe photocathode has zero quantum efficiency beyond 320 nm. The input window is made of MgF_2 to reach down to Lyman α wavelength (an important target of SPICAM instrumentation). An additional sapphire filter is glued above the window and covers it in part, preventing overlapping of diffraction orders and Lyman α stray light.

[20] For solar occultations, a small mirror (0.2 cm^2) looking at 90° from the main optical axis is implemented at the entrance pupil. During solar occultation measurements the detector operates at the lowest gain and integration time of 20 ms.

[21] The focal length of the UV telescope is such that one CCD pixel covers a FOV of $0.01 \times 0.01^\circ$. The narrow part (0.02° wide by 1.9° long) of the slit of the spectrometer achieves a spectral resolution of 1.5 nm (about 3 CCD pixels), while the wide part (0.2° wide by 0.98° long) has a higher photometric sensitivity for extended sources (factor ~8), at the expense of a reduced spectral resolution (6 nm). In principle SPICAM can record 288 spatially resolved spectra along its 2.88-degree long slit (i.e., each spatial element subtending 0.02×0.01 degrees on the sky). However, in practice, only 5 spectra are transmitted for each 1 second measurement in order to save data volume transmission. These spectra are formed differently for various modes of CCD readout (Figure 4). The most used mode is such that each of the 5 spectra is a sum of N individual CCD line spectra (binned on chip in the read-out line, before reading), with N = 2, 4, 8, 16, or 32, forming 5 adjacent spatial bins of variable extent (from 0.02° to 0.32°). Two other modes may be used for special purposes: a full imaging mode, when the whole CCD is read, 5 consecutive lines at each reading, with the first one of each reading displaced by 4 lines, and a "progressive binning" mode providing a higher dynamic, since 2, 4, 8, 16, 32 lines are binned together in the 5 spectra transmitted to TM (with the risk of saturation and over spilling of the register). This mode was useful at the beginning to optimize the gain level and integration time for nadir observations.

[22] The gain of the MCP (Micro Channel Plate) of the image intensifier may be adjusted by telecommand with a high voltage level from 500 to 900 volts, commanded by a digital level HT from 0 to 255. When a photo-electron is created in the photocathode (a photo-event), it results in a pulse of light from the phosphor, distributed over a few pixels of the CCD. It is detected by the CCD reading electronics by a number of ADUs (Analog to digital Units). At HT = 20 (a usual low gain level necessary to avoid saturation for dayside nadir observations), there are about 1.5 ADU created per photo-event, while for HT = 200, there are ~40 ADU per photo-event. The absolute calibration of the instrument is well characterized by numerous

Table 2. Characteristics of the SPICAM Light UV Channel

	Characteristics
Primary mirror	Off-axis parabola 40×40 mm^2
	Coated MgF_2, f = 120 mm
Slit	50 μm $\times$ 4.6 mm
	500 μm $\times$ 2.2 mm
FOV	of a pixel $0.7' \times 0.7'$
	$2^\circ \times 3.16^\circ$ no slit (stellar occultation)
	$0.24^\circ \times 0.95^\circ$ with double slit
Spectral range	118–320 nm
Grating	Holographic, concave, toroidal coated MgF_2
	290 l/mm, blazed 170 nm
Spectral resolution per pixel	0.51 nm
Resolving power (occultations)	120–300 stellar; small slit
Resolving power (extended source)	120–300 small slit, ≈20 large slit
Pointing accuracy	<0.2°
Detector	CCD Thomson TH7863 TE cooled at 270K. useful 288×384 pixels, 23×23 μm^2
Intensifier	Hamamatsu 200M, solar blind CsTe photocathode, input window MgF_2 + sapphire
Vertical resolution	<1 km (occultations)
	~10 km (limb)

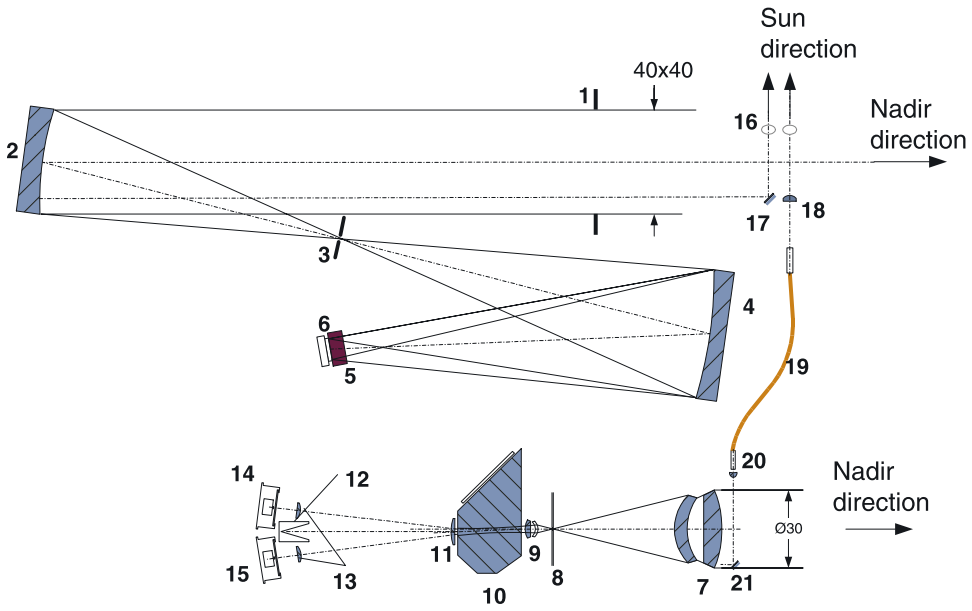

Figure 1. Optical scheme of the UV and IR channels of SPICAM Light. 1, aperture blend of the UV channel; 2, off-axis parabolic mirror; 3, slit (can be changed from wide to narrow by a mechanical actuator; see text); 4, concave UV grating; 5, intensifier; 6, CCD; 7, IR channel objective; 8, IR FOV diaphragm; 9 and 11, collimating lenses; 10, AOTF crystal; 12, light trap for undiffracted light; 13, detector proximity lenses; 14, "extraordinary" beam detector; 15, "ordinary" beam detector; 16, solar opening (closed by a shutter when not looking to the Sun); 17 and 21, flat mirror; 18, IR solar entry; 19, optical fiber; 20, fiber collimator.

observations of hot UV stars and comparison with previous IUE (International Ultraviolet Explorer) measurements (see below for further details).

[23] There is a potential danger to activate the intensifier at a large gain on an intense source of light. Therefore this high gain has to be used cautiously, on the day side but at high altitude, and then on the night side. One constraint of SPICAM operation is that during one observing period (ON-OFF), the parameters of the instrument may not be changed. In particular, when a fixed inertial attitude of the spacecraft is chosen, then one must be sure that the signal will not be too strong to damage the intensified detector, if one uses a high gain on a bright target.

[24] Figures 3 and 4 show an overall view of SPICAM, containing SPICAM UV and SPICAV IR, side by side. The wavelength reflectivity of each component was tested under vacuum before integration in the flight model. The whole instrument was tested in a vacuum chamber and exposed to the beam of synchrotron radiation at Station d'Etalonnage of IAS in Orsay. We could verify the optical adjustment, by measuring the monochromatic image of the beam at various wavelengths and positions on the CCD [*Guibert*, 2005]. The

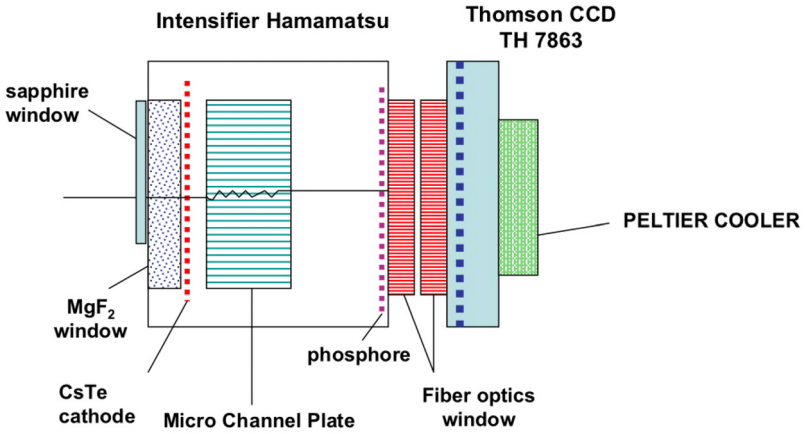

Figure 2. Sketch of the SPICAM UV detector. It combines a UV image intensifier from Hamamatsu, transforming each UV photon at the entrance into a pulse of green light generated by the phosphor. Then the image is conveyed through two blocks of fiber optics, one included in the Hamamatsu detector, the other one being attached to the Thomson CCD (by Bill Sandel at LPL). The sapphire window is placed to block second order of grating diffraction.

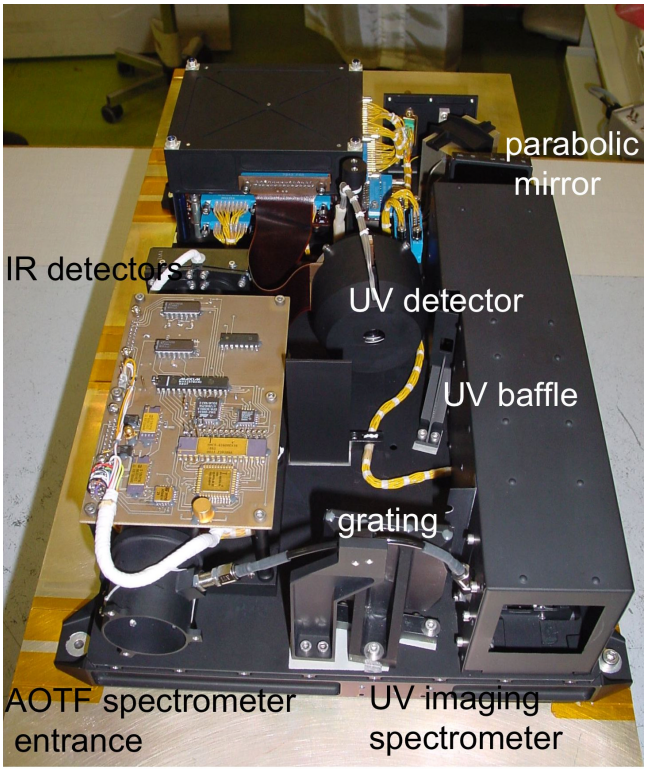

Figure 3. SPICAM sensor unit with the two UV and IR spectrometers, side by side. The entrance of the UV spectrometer baffle is on the right (5 × 5 cm, giving the scale), while the entrance of the AOTF IR spectrometer is on the left side.

detector was calibrated by using the method of photon transfer, which yields the number of ADUs generated in the CCD by one single photo-electron event, as a function of the high voltage applied to the MCP.

3. Modes of Observations for SPICAM

3.1. Mars Express Orbit Configuration and Evolution

[25] The orbit is eccentric: at insertion it was with a period 7.57 hr, pericenter 250 km, apocenter 11,559 km. Later on, it was modified to so-called G3-b configuration on 3 March 2005, with a shortened period of 6.72 hr, 298 km at pericenter and 10,107 km of altitude at pericenter. After 11 orbits, almost the same region is observed (for optimizing HRSC camera mosaic). The orbit is almost polar, allowing good views of both poles during summer. The orbital plane is precessing, and the latitude of the pericenter is moving rather fast in the orbital plane, yielding a large variety of geometries for night side and day side observations (Figure 5).

3.2. Pointing Capabilities of Mars Express

[26] The Mars Express spacecraft design by EADS/Astrium is a somewhat size-reduced version of Rosetta spacecraft, sent to a rendezvous with a comet. It was designed originally with two basic modes of orientation. For telecommunication, the antenna (−X axis) is directed to the Earth, while rotating solar panels (around the Y axis) may be turned perpendicular to the Sun to maximize power. The attitude is therefore constant in inertial space. In the nadir mode observation, the +Z axis (bore sight with viewing axis of optical instruments SPICAM, HRSC, OMEGA, PFS) is maintained to the center of Mars. There is no horizon sensor, but the position on the orbit is known in the software spacecraft, and command laws are fed to the rotating inertial wheels to achieve the desired law of orientation along the orbit to maintain +Z axis to the nadir.

[27] SPICAM takes advantage of the built-in capabilities of MEX AOCS (Attitude and Orientation Control System) to execute various modes of observations. They are described briefly below, while Table 3 indicates some statistics about their use during the MEX mission first 18 months. Their geometry is illustrated in Figure 6.

[28] The slew maneuver to go from one orientation to another is typically made at a slew velocity of 0.1–0.5 deg/s, which requires 20–30 minutes in average. In the *stellar occultation* mode, MEX +Z axis is oriented to the direction of a star, selected from a list of 50 stars (brightest in UV). The orbital motion will make the star disappear behind the limb. In the *solar occultation* mode, the side-port for Sun observations of SPICAM (Figure 1), which lies in the XY plane of the spacecraft, is oriented to the Sun. When entering eclipse, the solar occultation will occur.

[29] In the *limb* mode, the +Z axis is oriented in a precalculated orientation, in such a way that it will scan

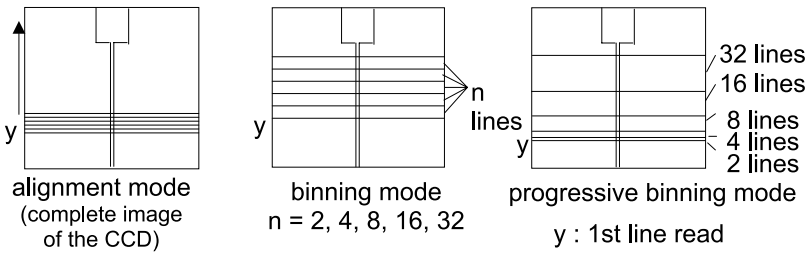

Figure 4. The various modes of SPICAM UV CCD reading. (left) A complete image of the CCD is obtained by groups of 5 lines (with 1 line overlap), in order to find the spectrum of the star (alignment mode, used very rarely). (center) The binning mode is the most often used, when 5 bins of 2, or 4, 8, 16, 32 lines are grouped together. The first line may be selected anywhere. (right) The progressive binning mode is used for higher dynamics: 32 lines for a weak signal, 2 lines for a strong signal. This mode was used at the beginning of MEX mission to explore the actual intensities observed.

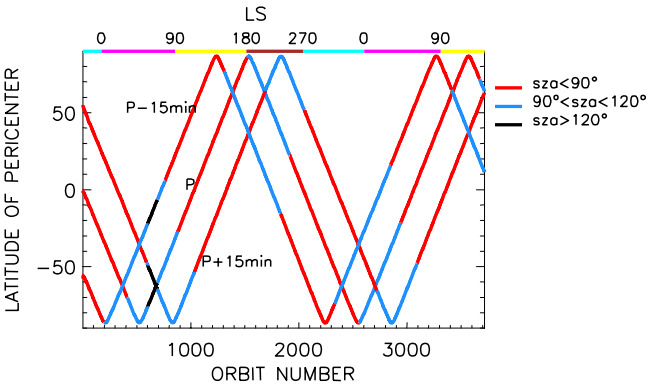

Figure 5. Evolution of the latitude of the pericenter and two other points (at pericenter ±15 min) as a function of time and orbit number. The color code indicates the solar illumination conditions at pericenter and the two other points, determined by the solar zenith angle (SZA). In black, periods when the pericenter is in the deep night side (SZA > 120°). In red, periods on the day side (SZA < 90°). In blue, period in the night, not far from the terminator (90° < SZA < 120°). The observing programme of MEX is discussed 3 months in advance by slices of 100 orbits which are planned together, as a compromise between the various investigations.

across the limb. Mainly two variants of this mode were used: the tangential limb mode (see below), and the limb crossing in the orbital plane. In this last case, the slit of SPICAM, the CCD scan line of HRSC, and the mirror scan of OMEGA may be put parallel to the limb. In such an orientation, the whole illuminated planet may be scanned in ~30 to 40 mn, a useful mode when the pericenter is not on the Sun side. In this last case, staying to the nadir over the whole sunlit portion of the orbit would require too long a nadir mode for the spacecraft. In addition, the UV spectrometer CCD camera electronic heats up, and its operations are limited to 40 mn to avoid too large temperatures that might be destructive.

[30] The slewing capabilities of MEX were used also during some observations of Phobos (to maximize the time of observation), and during a small number of EPF maneuvers (Emission Phase Function), where a particular geographical area is observed from various emission angles, to discriminate the emission from the ground from the airborne dust scattering. For Martian and interplanetary H Lα measurements, special observations were executed, to scan a large range of altitude, either with a large slew on the sky starting above the limb, or by letting drift the spacecraft along its orbit with a fixed inertial direction. The geometry of some of these modes is sketched in Figure 6.

[31] Spacecraft orientation is a resource which has to be shared between all the instruments. Additional spacecraft constraints add to the complexity of establishing a plan of observation in advance: solar panels are delivering only 70% of their nominal power (due to a faulty wiring), radiators to cool some instruments should not be illuminated by the Sun, a window of 4 hr per day is reserved for up-link telecommanding, and some other constraints. As a result, the plan adopted 3 months in advance of execution is a compromise between various contradictory requirements from the various instruments and the spacecraft, usually resolved during lively animated teleconferences between ESA and the PIs teams. Table 3 indicates the type and number of observations obtained with SPICAM since the orbit insertion (25 December 2003) to 4 April 2005.

3.3. Geometry of Nightglow/Dayglow Limb Observations: The Limb Grazing Mode

[32] Airglow spectroscopy and radiometry is a powerful method of investigation of the physics of upper atmospheres of terrestrial planets (Venus, Earth, Mars). After the pioneering work of UV spectrometers on board Mariner 6, 7, 9 [*Barth et al.*, 1971; *Barth et al.*, 1992, and references therein], this technique was somewhat neglected for the following 30 years around Mars, except for rare observations in the EUV with rockets and Earth orbiting observatories.

[33] While dayglow was clearly measured and identified in the Mariner 6, 7, 9 observations, the first detection of nightglow in the atmosphere of Mars was made with SPICAM [*Bertaux et al.*, 2005a]. These successful observations are the result of the high sensitivity of SPICAM and specially dedicated spacecraft operations to optimize the geometry of limb observations, yielding more signal than the MEX nominal nadir-looking geometry around pericenter. Their particular geometry is illustrated in Figure 7. The spacecraft is maintained in a fixed inertial attitude, a mode heavily used by SPICAM for star occultation measurements, but also for limb observations. In fact, on the day side, there are two reasons to observe the aeronomical

Table 3. Some Statistics for the Use of SPICAM in the Various Modes of Observation, Covering the Whole Year 2004 and the First Trimester of 2005[a]

Mode of Observation	January to December 2004	January 2005 to March 2005	4 January to 4 April 2005
Nadir looking	318	129	447
Star occultation	421	114	535
Limb observation	43	51	94
Solar occultation	129	156	285
Others	1	10	11
Number of observing orbits	911	450	1 361
Number of days of operation	256	92	348
Data volume, Gbit	24.2	11.5	35.7

[a]In spite of the difficulties associated to the planning operations, a fair number of observations were made in the various modes.

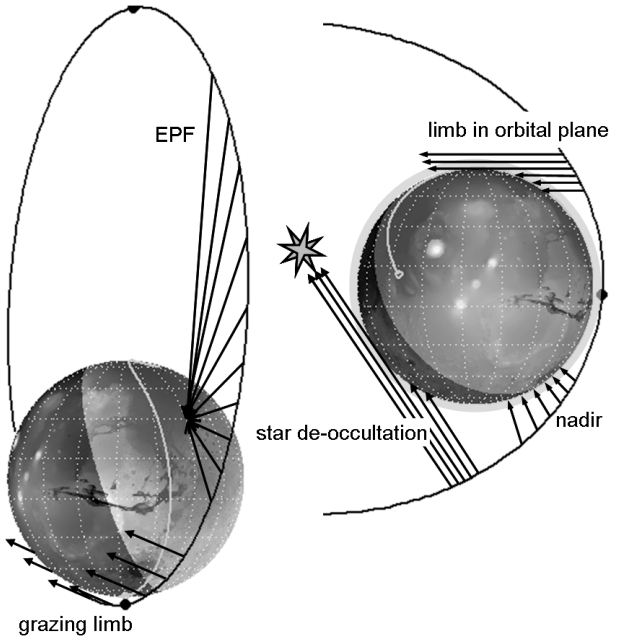

Figure 6. Sketch of various modes of observation of SPICAM. In all cases, the black line indicates the LOS of SPICAM to the target. Except for the usual nadir orientation and the special case of EPF (Emission Phase Function), the spacecraft is drifting along the orbit, keeping a constant celestial orientation, which allows us to scan across the target (limb) or to perform an occultation of star or Sun.

emissions at the limb rather than to nadir: maximizing the integrated emission (Chapman factor), and eliminating the strong UV background of solar light scattered by the surface and suspended dust of Mars.

[34] Planning a limb observation requires to find an inertial direction such that, during the orbital motion of MEX, the LOS will scan across the limb. In order to maximize the duration of the observation, we have designed a special type of observation in which the LOS does not cross vertically the limb, but rather skims the limb tangentially, with a minimum altitude which may be selected (so-called tangential, or limb grazing, mode). Geometry tells us that, for any point M of the eccentric orbit, there are two LOS directions which will skim the limb tangentially, with a specified minimum altitude Z_{min}. They are contained in the two planes tangent to the sphere $R_{Mars} + Z_{min}$ which contain also the tangent to the orbit at M (the velocity vector). One of them is selected to plan the observation, as well as the point M, according to the desired position of the tangent point at minimum altitude. One particularity of this kind of observations is that several geometrical parameters of the LOS tangent point are varying significantly and simultaneously during the observation (altitude, latitude, solar zenith angle (SZA)).

4. In-Flight Performances of UV Spectrometer

4.1. Pointing Quality

[35] For all SPICAM modes of operation the quality of the results depends somewhat on the pointing quality. The pointing accuracy of Mars Express is usually much better

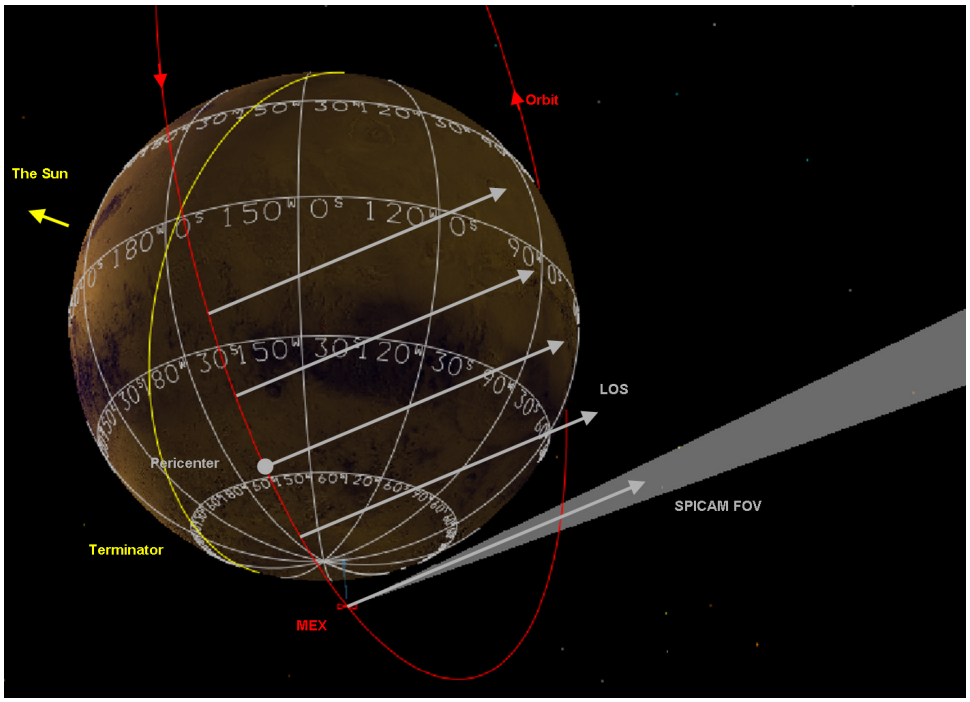

Figure 7. Geometry of grazing limb observations, which allows us to maximize the time spent to observe the limb. The spacecraft is oriented with the +Z axis (SPICAM LOS) fixed inertially, scanning the limb twice. In this case, the LOS was perpendicular to the velocity vector at pericenter, for an optimum vertical resolution at the limb.

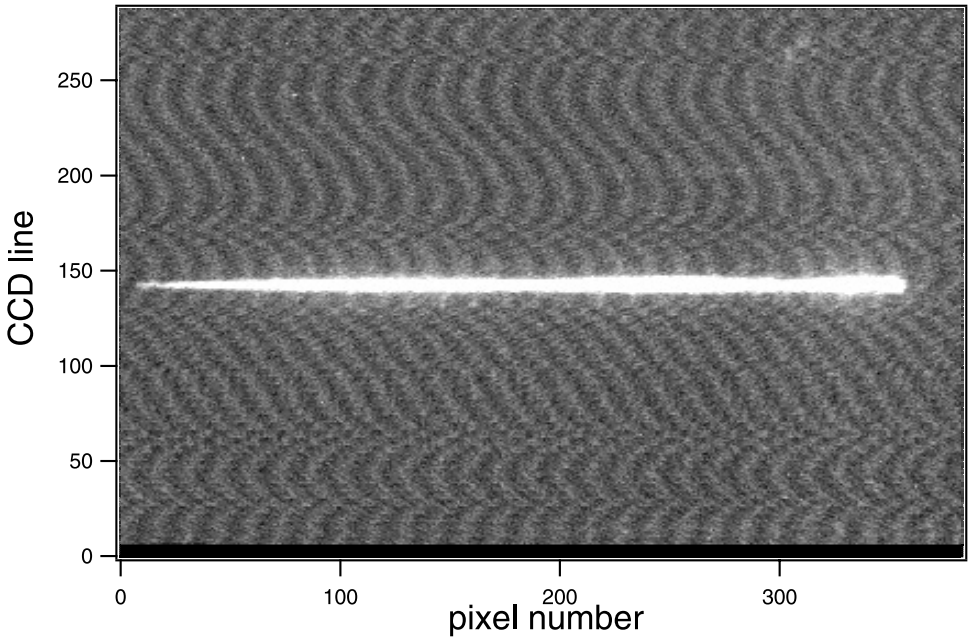

Figure 8. Distribution of light over the whole detector when a star (Delta Scorpii) is observed without the slit. The log of intensity in ADU is gray-coded, and the contrast is enhanced to emphasize low signals. The spectrum is horizontal, along the CCD lines, parallel to the Y axis of the spacecraft. Because of optical aberrations, the spectrum is spread over several lines of the CCD. The slit orientation is parallel to the X axis of S/C, along the column axis of the CCD (vertically in this figure). The ''tapestry'' effect is a residual electronic noise (pseudo-periodic), after subtraction of offset and Dark Charge.

than the 0.1° which is the spacecraft specification. There is some offset between the center of our CCD detector and +Z spacecraft axis, which in principle are bore sighted: 0.17° in one direction (along the wavelength axis, parallel to the Y spacecraft axis), and <0.01° in the perpendicular direction along the X axis, as determined by star spectra during the cruise and outside the atmosphere with the alignment mode, allowing us to get a full image of the CCD (Figure 8).

[36] For a star observation we ask the spacecraft to put the inertial direction of the star (α, δ), exactly along the +Z axis, or with some offset from +Z axis, along a direction defined by two angles θ, φ in the body axis reference frame: θ, the angle of the projection of this direction on the X, Y plane with the X axis, and φ the angle of this projection with the direction.

[37] We tried several offsets angles, and as a result the spectrum of a star was put at various places on the detector. Figure 9 illustrates the various recorded spectrum of the same star Sirius (41 in total) in ADU units, put on the same wavelength scale, obtained between orbits 906 and 1410 (spanning about 5 months). It shows the excellent stability of the instrument, with no sign of aging on this time frame. The curves are different between ~135 and 180 nm. This is the effect of the sapphire window, whose edge is placed in the middle of this wavelength interval for the nominal pointing. The sensitivity is larger outside the window than through the window, because its transmission is <1. There is no abrupt change on the curve at the place of the edge, because a point on the cathode at the edge or around the edge ''sees'' the grating over an angle of ~ 20°, partly through the window, and partly outside the window, providing a continuous response to a continuous spectrum.

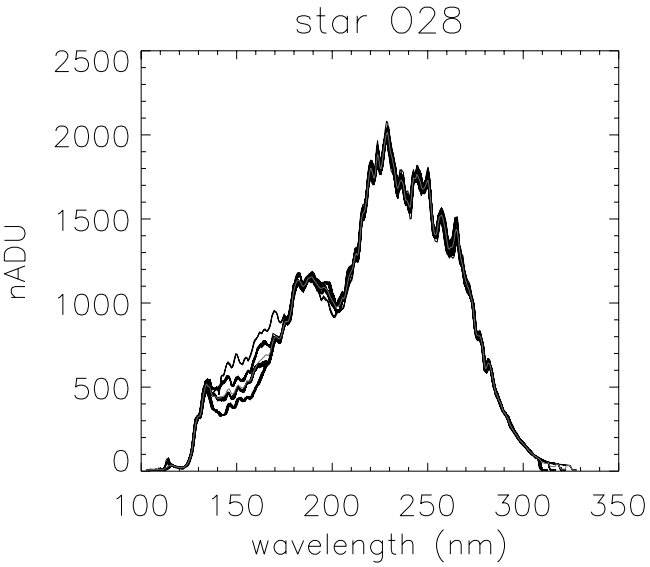

Figure 9. Overplot of 41 spectra of star Sirius (named O28 in the SPICAM star catalogue) recorded by SPICAM outside the atmosphere of Mars, between orbit 906 and 1410 (spanning 5 months). The various spectra were obtained with different offset pointings, resulting in various positions on the detector. They are in ADU units and are put on the same wavelength scale. It shows the excellent stability of the instrument, with no sign of aging over 5 months. The curves are different between ~135 and 180 nm, an effect of the sapphire window, which edge is placed in the middle of this wavelength interval for the nominal pointing (see text).

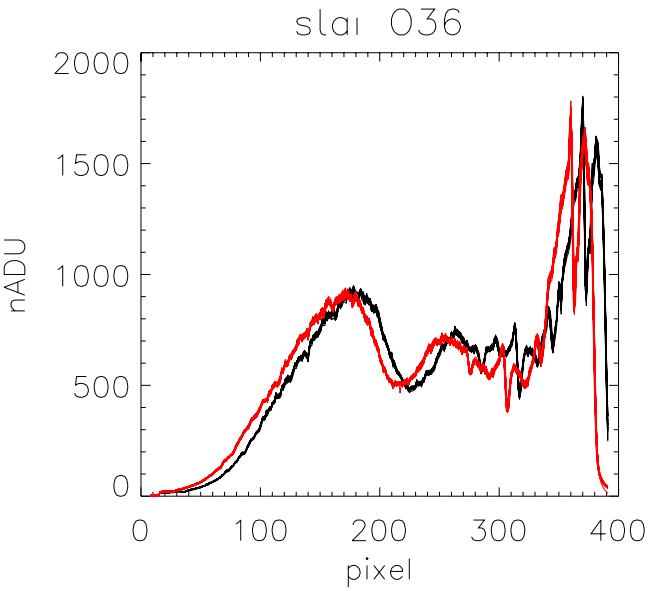

Figure 10. Overplot of 31 spectra of star Zeta Puppis (O36 in the SPICAM catalogue) recorded by SPICAM as a function of pixel position. 310 nm is at left, 110 nm is at right (reversed scale). They all fall on only two places. In red, 23 spectra (red curves) are falling at the expected position, which is determined by the star strong stellar Lα absorption line, centered on the same pixel as the atmospheric Martian line observed with the slit. In black, 13 spectra are shifted by about 12 pixels, corresponding to a pointing error of 0.12°, which is linked to the use of Star Tracker B (redundant) instead of the nominal one (Star Tracker A).

[38] We recently discovered that the pointing is not perfectly repeatable. With exactly the same offset angles θ, φ the spectrum of star Zeta Puppis should be at the same place on the detector, but it is not. As shown in Figure 10, there are two places where it can be seen, differing by about 0.1° (corresponding to about 6 nm in wavelength shift). On each of the positions, all spectra of one class are very well superimposed. This problem triggers two difficulties. The first is that we cannot rely on the commanded offset pointing to establish the wavelength assignment of each pixel of the star spectrum, and we have to examine carefully the star spectrum recorded outside the atmosphere to determine exactly its wavelength assignment (the wavelength of each pixel). The second is that a number of star occultations with the slit in place have failed.

[39] Usually the star occultations are made without the slit, unnecessary since a star is a point source. Some star occultations were performed on the day side with the slit, which allows us to eliminate at least partially the solar light scattered at the limb by dust and atmosphere. Some of them were successful: the star signal is about twice weaker than without the slit, because of optical aberrations of the off-axis parabolic mirror. But several others have failed because of the nonperfect repeatability of pointing. This problem has been recently traced back to the use of either the Star Tracker A or redundant star tracker B, whose offsets with the XYZ body axis of the spacecraft are not identical, and only the offsets of nominal Star Tracker A are taken into account in the spacecraft on-board software to orient MEX to a given direction. This problem should be corrected in the future.

[40] The pointing stability seems to be quite good. When a star is observed outside the atmosphere, the signal is usually recorded in 5 bands of 16 CCD lines, the central band collecting >90% of the total star signal (computed from Figure 8). The signal in the central band does not show periodic fluctuations (at least before the deployment of Marsis radar antennas), which would be a sign of angular oscillations. All slews maneuvers of the spacecraft (at a maximum angular rate of 0.5°/s) are followed by a "tranquilization" period of about 10 mn, before the spacecraft may be considered as stable, and SPICAM is switched ON only after this time. Actually, in order to monitor the small motions of the spacecraft, we have analyzed some observation of the Sun, with the slit in place and 5 bands of 4 lines, after the deployment of Marsis radar antennas. One could then analyze the signal and determine the oscillations in the two directions, across the slit (the total signal in all bands fluctuates together) and along the slit (the distribution of the signal among the 5 bands fluctuates also). We determined a small oscillation of 8 second period, not detrimental for star occultations, because the flux is collected in a band of 16 lines, and the signal remains constant in spite of the oscillations. For solar occultations, a special analysis should be performed.

4.2. Absolute Photometric Calibration From Star Observations

[41] The absolute photometric calibration was first done on the ground. All optical elements were measured separately, and the whole instrument was calibrated, but with a limited accuracy, because of inherent difficulties in the vacuum UV. Fortunately, we can use stars to obtain a more accurate determination of the sensitivity as a function of wavelength. We used the measurements obtained by IUE (International Ultraviolet Explorer, ESA/NASA/UK project) as a reference. However, we encountered two problems. Initially we used the star Delta Scorpii, but then it was found that this was a bad choice, since this star experienced recently (in 2002) a large surge brightness in the visible, and no one knows if its UV flux changed since IUE time. The second problem is that IUE measurements of the same star may show variations which are not intrinsic to the star, but rather to the quality of IUE pointing, since the FOV of IUE was 20 arc sec, and centering was not always perfect. Therefore different IUE exposures may give different answers. We found out that HST calibration in the UV was performed also with IUE collected spectra, and 4 stars used by HST are indeed SPICAM targets: Zeta Puppis (O36), Beta Cen (O60), Eta Uma (O57), Zeta Oph (O77). The number between parentheses is a reference number of the star in the SPICAM star catalogue. Therefore, assuming that the HST calibration is correct, we are now basing the SPICAM absolute calibration on this quatuor of stars, and have used the IUE data selected for HST calibration (which slightly differs from what is found in the IUE database in some wavelength regions).

[42] The IUE spectrum, given in erg/(cm^2 s Å), is converted in a photon flux Φ in photons/(cm^2.s.nm). On the

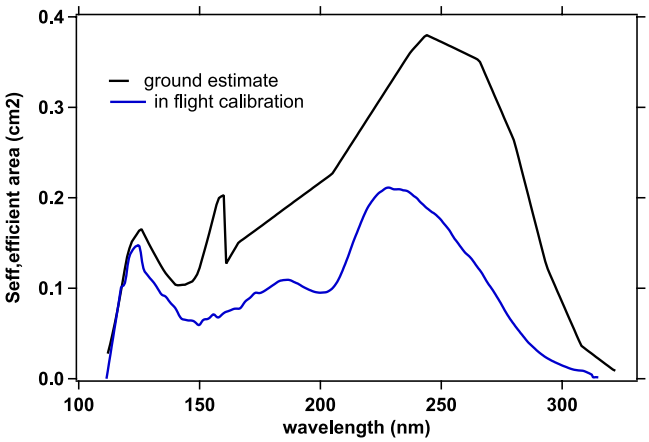

Figure 11. Sensitivity of SPICAM to a stellar source, expressed in cm^2. Black curve: estimation from ground calibration of the various optical elements. Blue curve: sensitivity determined by comparison of the measured spectrum (in ADU) of star Zeta Puppis to the IUE absolute spectrum of the same star. The gain level used was defined by HT = 20, and the gain was determined to be 1.55 ADU per photo-event from an independent statistical analysis of observed fluctuations of the star signal. The long wavelength decrease is due to the CsTe response, while the short wavelength decrease is due to the cutoff of MgF_2 window of the detector. The sharp transition in the black curve near 160 nm was taking into account the transmission of the sapphire window, which has a sharp cutoff below 160 nm. The actual curve has a smooth transition, because a point of the photocathode near the mechanical edge is seeing a part of the grating through the sapphire window and another part without the sapphire window.

other hand, SPICAM data is in ADU units, the output of CCD reading. As described above, the High Voltage of the image intensifier may be adjusted to give more or less ADUs per photo event (one photo-electron created at the cathode of the image intensifier, creating a pulse of light in the CCD), a parameter that we call G, the gain of our detector system.

[43] The calibration factor of SPICAM is therefore the product $G \times S_{eff}$, where S_{eff} is the so-called "efficient area" expressed in cm^2, and defined in the relation

$$N_{photev} = \Phi\ S_{eff}$$

where N_{photev} is the number of photo-event detected by SPICAM per second and per nanometer. Also we have the relationship

$$N_{ADU} = G\ N_{photev}$$

resulting in the calibration equation:

$$G \times S_{eff} = N_{ADU}/\Phi$$

[44] The gain G was determined on the ground for various levels of the High Voltage of the image intensifier. It varies from 1.0 to 79 in the whole range of possible commanded levels of HV, defined by the instrument parameter HT (from 1 to 255). The gain may be was also checked in flight by a statistical method, by determining the mean number of photo-events contained in the whole band devoted to the star signal outside of the atmosphere. The total ADU signal fluctuations are analyzed, and the gain G is determined as

$$G = Var(S_{ADU})/(2\ S_{ADU})$$

where S_{ADU} is the mean value of a series of measurements, Var (S_{ADU}) is the variance of the series, and the factor 2 comes from the non-Gaussian distribution of the number of electrons coming from a single photo-event [*Sandel and Broadfoot*, 1986].

[45] In Figure 11 is displayed the sensitivity of SPICAM to a stellar source, S_{eff} (in cm^2), as a function of wavelength. The drop at short wavelength cutoff is due to the opacity of MgF_2 window, while the drop at long λ is due to the drop-off of the CsTe cathode (so-called solar blind behavior).

[46] It should be understood that this curve is representing the sensitivity of the instrument for a star source placed at the "right" position, defined as the center of the spectrometer slit. The nominal wavelength assignment is also defined as such, making it valid for all extended source measurements collected with the slit in place. Figure 9 indicates that, when the star is at other places, the sensitivity across the detector is quite similar (at least in the small region explored), except near the edge of the sapphire widow. This curve is also only valid when the star signal is integrated over 8 CCD lines (centered on CDD line 144), collecting 90% of the total signal.

[47] When using this S_{eff} curve for the calibration of extended source measurements (filling the whole slit), one has to take into account this 90% factor (because the whole signal is collected with an extended source), and the actual FOV of one CCD line: 50 (slit width) $\times$ 23 (CCD pixel size) μm and a focal length of 120 mm of the parabolic mirror. The solid angle dω subtended by one CCD line is therefore 7.986×10^{-8} steradian. For those more familiar with Rayleigh (a unit used for airglow), remember the definition:

[48] One Rayleigh (1 R) = $10^6/4\ \pi$ Photons/(cm2.s. steradian). Therefore an extended source with a brightness B expressed in R/nm would give

$$N_{ADUB} = G\ B\ d\omega\ S_{eff}/0.9 = 1.06 \times 10^{-2}\ S_{eff}\ B$$

in ADU per second and per nm, for each line of the detector, at gain G = 1.5.

[49] Transporting the instrument calibration for a star to the calibration for an extended source may sometimes be a problem. Therefore we compared the Lα interplanetary sky background (extended source) measured by SPICAM in some directions, and the SWAN measurements on board SOHO obtained simultaneously in a similar direction. The SWAN calibration is based also on HST calibration at Lα on interplanetary sky background [*Quémerais and Bertaux*, 2002], and indeed a full consistency was found between the calibration factors found by comparing HST and SPICAM on stars, and SWAN and SPICAM at Lα with an extended source.

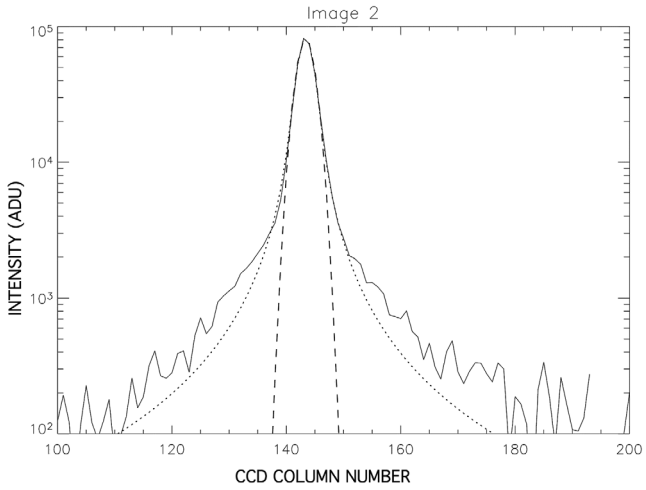

Figure 12. Solid line: distribution of light along the column axis of the CCD (perpendicular to the dispersion direction) of a stellar image taken in the Imaging mode, during the cruise to Mars, displayed in Figure 8. All wavelengths are summed together. The dashed line is a Gaussian fitted to the central part, while the dotted line is a Lorentz profile fitted also to the external part.

[50] When a star is observed without the slit, the star light is seen to be spread over many CCD lines, with a distribution perpendicular to the dispersion axis (along CCD columns) displayed in Figures 12 and 13. When the usual configuration of 5 bands of 8 CCD lines each is used, the relative content is 1, 3, 90, 5, 1% for bands 1 to 5, respectively. This spreading is most likely due to scattering on the surface of the grating, or within the MgF_2 window of the detector; it is a sign of the existence of some stray light, called internal, because it is generated after the slit or focal plane of the mirror. Some photons are detected away from their nominal position, both vertically and in wavelength position. The analysis of some solar light scattered at the limb (see below) allowed us to determine the level of stray light, mainly coming from the large part of the slit, and to make a systematic correction for it.

[51] In some rare occasions, we have found some evidence of external stray light also, defined as detected photons coming from outside the nominal FOV defined by the slit at the focal plane of the parabolic mirror. We are still in the process of characterizing of this external stray light.

4.3. CCD Dark Charge Correction

[52] The CCD generates some dark charge electrons, at a rate which is a function of its temperature. The CCD may be cooled by a Peltier cooler which is not systematically activated. Some CCD pixels are masked, and are sensitive only to dark charge (DC) and to the electronic offset which is present to avoid a negative value at the entrance of the A/D electronic converter. When the Peltier cooler is activated, the detector is cooled and the DC is decreasing first, but after a few minutes, the temperature is increasing again, and

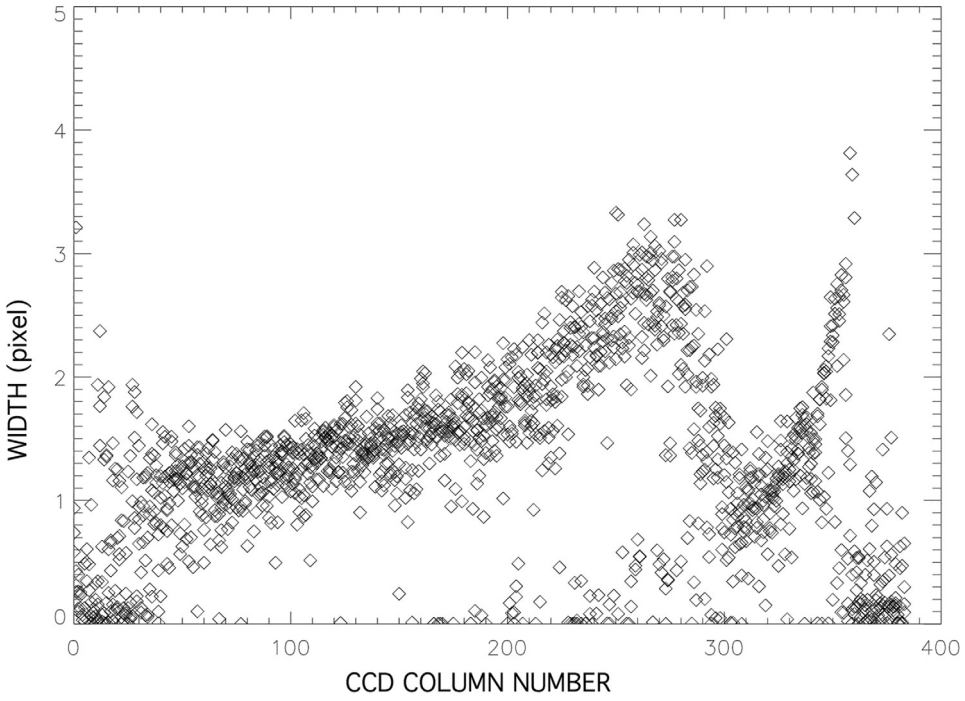

Figure 13. For each column of the CCD, the vertical width of the stellar spectrum recorded in Figure 8 is displayed in pixel units as a function of pixel number in the wavelength direction, increasing from right to left. The rapid change around pixel 290 is due to the effect of the sapphire window glued on the MgF_2 window of the image intensifier, combined with the rapidly changing index of refraction with λ of MgF_2 at short wavelength. The absence of the window (pixels > 270) improves the focusing for a while. The optical adjustment made on the ground is a compromise to get a good focus over the whole wavelength range. It may be assumed that the spectral resolution is also changing accordingly as a function of λ.

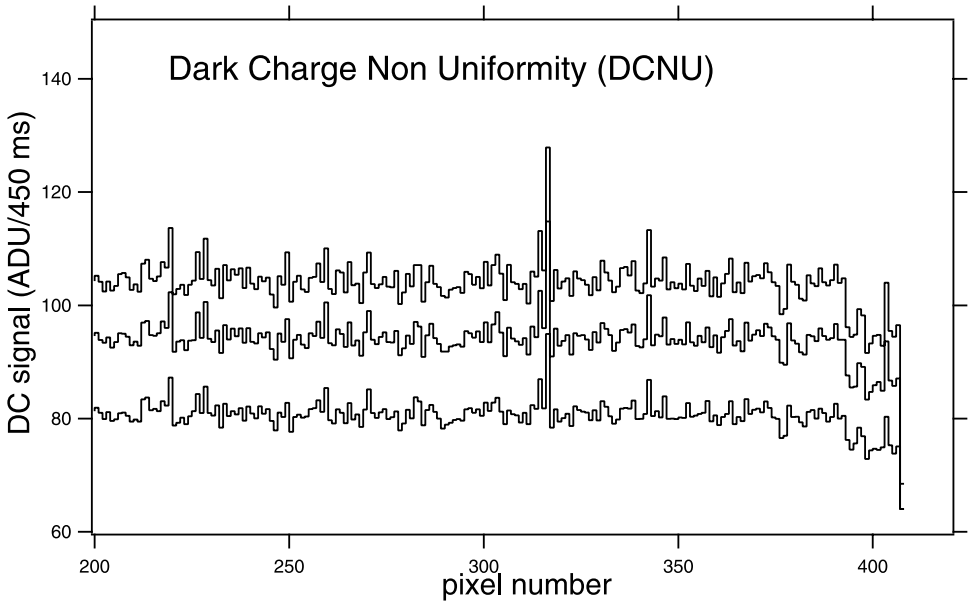

Figure 14. CCD Dark Charge (offset also included) as a function of pixel number, during a special observation (orbit 1789) with the intensifier off and no Peltier cooler. The three curves were taken at the beginning, after 10 mn and 18 mn of switch ON (the later, the warmer the CCD is, the higher is the DC signal, in ADU per pixel per 450 ms integration time, 4 CCD lines binned together, 100 spectra averaged for 100 s). The structure is identical, called the DCNU (Dark Charge Non Uniformity). The masked pixels (from 392 to 406) have a smaller signal. Still, a linear relationship between the DC+offset of each pixel and the masked pixels may be established from such observations, allowing corrections of normal observations. The DC due to the UV intensifier is neglected in the correction process.

the DC is also increasing. This is possibly due to an imperfect evacuation of the heat from the backside of the cooler. Special observations were performed with the intensifier off, to characterize the CCD output. It was verified that the signal (offset +DC) of measuring pixels was a linear function of the signal of masked pixel (also offset +DC). But the slope is different for each pixel, because the DC is different for each pixel (so-called DCNU, Dark Charge nonuniformity). In Figure 14 are displayed three spectra at three different temperatures of the CCD, showing the same pixel-to-pixel structure. The variation with temperature is due only to the variation of the DC, and not the offset, assumed to be constant. One important limitation of SPICAM UV is in the heating of the CCD camera electronics; possibly destructive temperatures might be reached if the camera is let ON for more than 40 minutes.

4.4. Internal Stray Light Correction

[53] Knowing from star observations that the light from the star is spread over a large area (Figure 12), we suspected that, when the whole slit is illuminated, the light entering the slit at other places than the lines of the CCD readout will spread over the whole CCD. In particular, we might expect a large contribution from the wide part of the slit, but not only.

[54] This problem was resolved with the study of the limb observation during orbit 1788 (date 7 June 2005, solar longitude LS = 225.7 degrees, distance to Sun ~1.39 AU), for a duration of about 20 minutes. 1181 spectrum were recorded. The observation was made with inertial pointing, and a grazing geometry, with a minimum altitude of 50 km below the Mars body limb. Therefore the limb crossing was slow. The measuring lines were binned by four, covering lines 134 to 153 which are all on the narrow part of the slit, near the center of the CCD (line 144). The idea of this observation was that we may consider that the distribution of dust scattered light at the limb is a "knife edge" in first approximation: very bright below a certain altitude, with a very rapid drop above. The spacecraft was oriented with X axis (and slit direction) perpendicular to the limb, with the wide slit looking at lower altitudes than the narrow slit (Figures 15a and 15b). Scanning the whole limb up to 200 km (duration 200 s from 0 to 200 km), there are times at which only the wide slit is illuminated by the bright limb.

[55] Figure 16 represents the mean light detected on the CCD as a function of time. The signals of the five bands are very similar, with a shift in time which corresponds to a shift in altitude at the limb. The limb is expected to decrease very rapidly, but there is still some signal decreasing slowly after the fast decrease (here between times 700 and 900 s. after the beginning of the observation): this light is suspected to be stray light from the wide slit. Indeed, when the spectrum of this emission is examined (Figure 17), it is completely different from the usual nadir or limb spectra (Figure 20). We do not see the strong UV features of the solar UV spectrum. The 5th band, located nearer the wide slit, detects more light than band 1, which is further away from the part of the CCD where is the wide slit. This also confirms that the closer we get from the wide slit, the more stray light is collected on the observed bands. This stray light represents around 10% of the signal. A precise study was performed by S. Perrier (unpublished report, 2005),

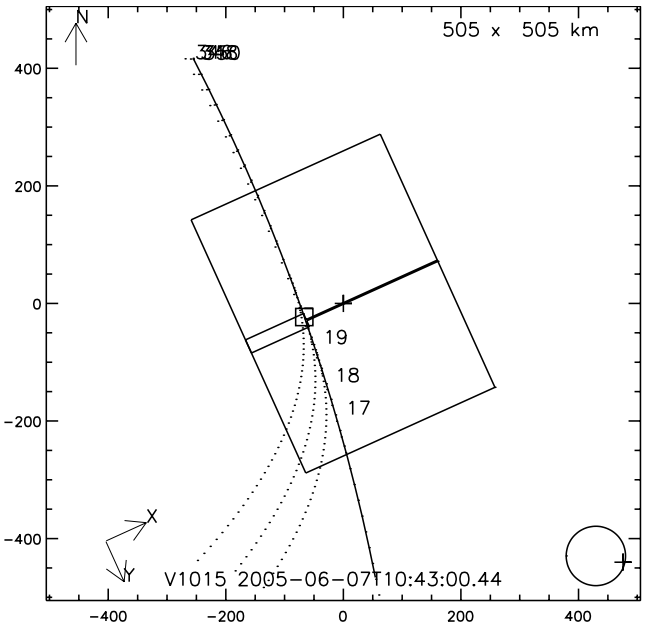

Figure 15a. Geometry of a special limb observation to study stray light generated in the spectrometer. The limb of the planet was Sun illuminated and is represented as a curved solid line. The full rectangle represents the whole CCD FOV, with the contours of the slit in the middle. The slit was placed perpendicular to the limb of the planet, with the large part of the slit on the bright part of the limb.

yielding the contribution of stray light of all parts of the slit to the read bands. Assuming that the whole slit is illuminated by the same spectrum, it is then possible to subtract from each measurement the spectrum of stray light of Figure 17 scaled by an appropriate factor, depending on the actual intensity recorded. This was done for the correction of the nadir data for the extraction of ozone content. When the scenery is not uniform over the slit FOV on the ground at a scale of a few kilometers (as it is the case over the polar caps), the correction of the stray light might be less accurate.

5. Nadir UV Observations

5.1. Measurement of UV Surface Albedo on Olympus Mons

[56] The summit of Olympus Mons is the highest point of the planet, with therefore the lowest atmosphere and dust content. We have used observations at Olympus Mons to build a reference spectrum, containing the solar flux, the sensitivity curve of SPICAM, and the albedo of the ground of Mars. We will use this reference spectrum by dividing other spectra by this reference spectrum, a classical method in spectroscopy, to concentrate on the variations of the spectra from one site to another.

[57] When looking to nadir, the measured light in the UV is a sum of several contributions: (1) solar light scattered by the atmosphere (Rayleigh scattering) and by dust/aerosols and (2) solar light scattered by the ground. Then, one may distinguish, for both sources, photons which have been scattered once by the ground, and once by the atmosphere, and in which order, before emerging at top of atmosphere. In the UV, where the ground albedo is weak, according to some HST data and Phobos 2 mission [*Wuttke et al.*, 1997], it is not obvious to predict a priori if an increase of dust and gas above the ground will increase or decrease the emerging quantity of light. The increase of gas will increase the Rayleigh scattering and decrease the radiation reaching the surface and backscattered upward, but the increase of dust may increase or decrease the light, depending on the quantity of dust and the single particle albedo. Data collected across Olympus Mons, offering a wide range of altitudes and atmosphere/dust quantities, offers a good opportunity to actually determine this. Figure 18 show the raw data for the five bands at orbit 1437 across Olympus Mons, the highest Martian volcano. Figure 19 shows the intensity in ADU/CCD line as a function of latitude (the ground track is climbing northward) for three different wavelengths: 210, 250 and 300 nm. In black is plotted the MOLA altitude of the ground, showing the strong relief of Olympus Mons around 17° latitude North. There is a strong decrease of the intensity when the ground point is at larger altitudes, relatively stronger at 210 nm than at 250 nm and then at 300 nm, which is consistent with a decrease of Rayleigh scattering with higher altitudes.

[58] Figure 20 shows an example of SPICAM recorded spectra in ADU on the same orbit: the shape of the spectra represents the solar flux scattered by the ground and atmosphere/dust of Mars, multiplied by the detector sensitivity and affected by the instrumental spectral resolution (both wavelength dependent). Strong solar spectral features structure the observed spectrum. It is seen that the recorded intensity decreases below ~220 nm and above ~290 nm.

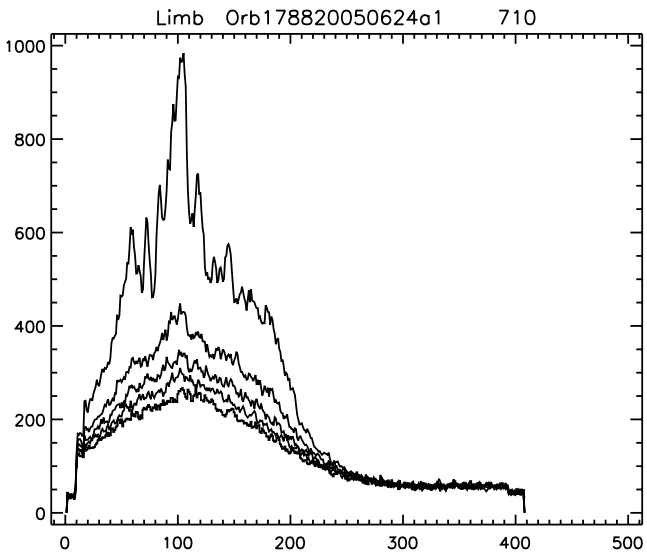

Figure 15b. During the one second exposure corresponding to the geometry of Figure 15a, the 5 spectra recorded at 5 points of the narrow slit are represented. The nearest point to the limb sees a normal solar spectrum (scattered by dust at the limb), while the others, further away, see only stray light generated through the large portion of the slit. A series of such measurements allowed us to characterize the stray light and correct for it.

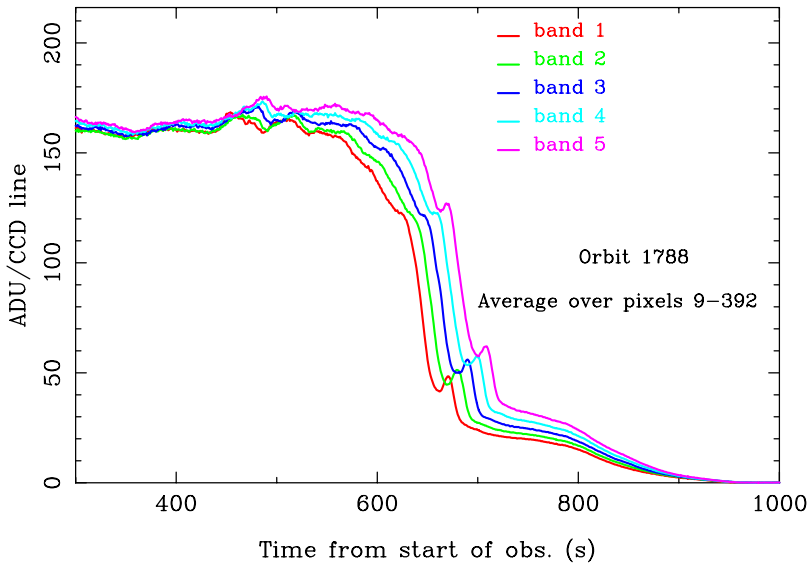

Figure 16. Light detected when the LOS is crossing the bright limb at orbit 1788. The observation was made with inertial pointing and limb grazing geometry, starting below the limb and ending with a limb-crossing configuration. The measuring lines were binned by four, covering lines 134 to 153, which are all on the narrow part of the slit, near the center of the CCD (line 144). The Integration time (per spectrum): 320 ms; HT = 1 (hence total gain of 1.005). All curves are alike, with a time shift corresponding to the difference of angle/observed altitude at the limb. There is evidence of a detached layer at time 700 for band 3. We would expect the signal to continue to decrease fast above the limb, while there is some signal for a long time. This is interpreted as internal stray light entering the spectrometer through mainly the wide part of the slit and scattered everywhere. The spectrum observed (Figure 17) does not have the standard shape of the solar spectrum (Figure 20).

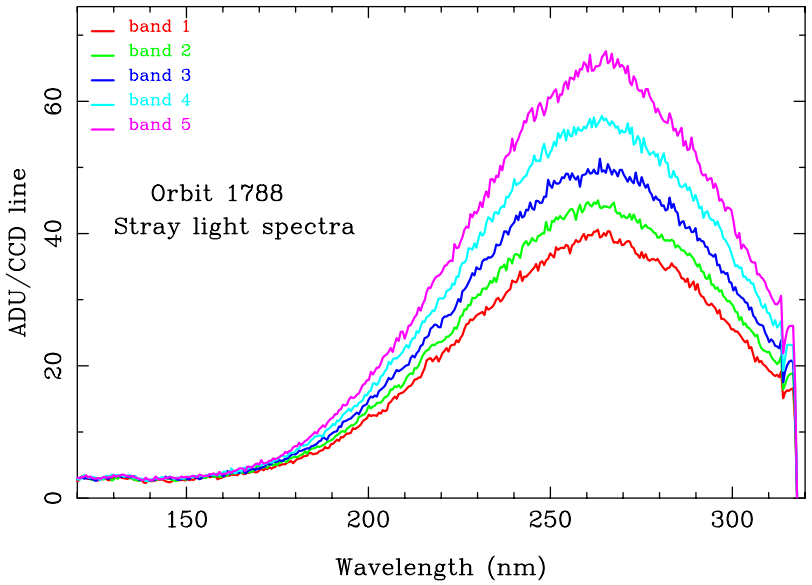

Figure 17. For each band, the spectrum displayed was averaged from t = 750 to 800 s (Figure 16). With the associated geometry file, we know that the 5 bands are observing between 80 and 200 km high in altitude, where the limb is normally very dark. At the same time, the wide slit is still illuminated by altitudes below the limb upper limit. The spectral shape does not show any solar spectrum features (see Figure 20). For these two reasons we assign the observed signal to internal stray light coming from the wide part of the slit. Internal refers to photons which have gone through the slit, coming from the corresponding FOV but which are detected at a position on the detector different from their nominal position (both in the spectral and vertical direction).

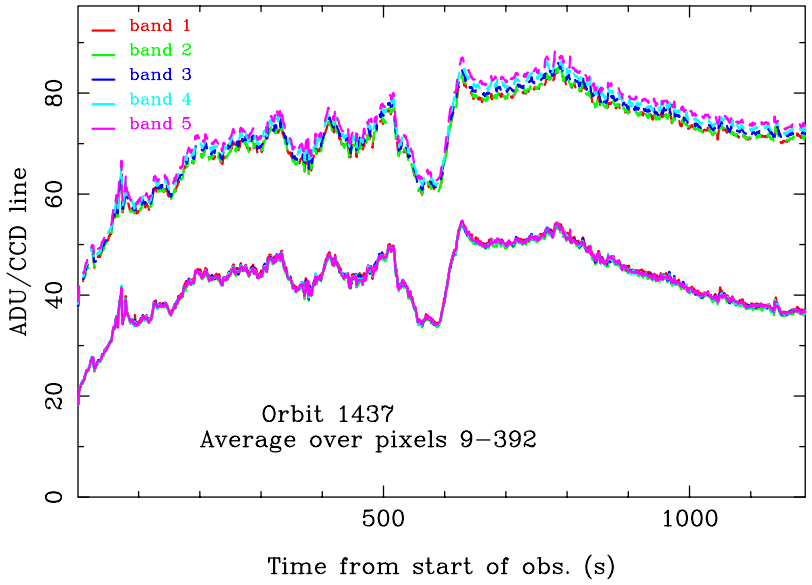

Figure 18. The upper curves (dashed lines) are raw data for the five bands at orbit 1437 across Olympus Mons (intensities integrated over the whole spectrum). They are slightly different. The lower curves (solid lines) are the same data after subtraction of offset, Dark Charge, and internal stray light. After the correction, the five bands have exactly the same intensity, which was not the case before the correction.

We therefore kept only the 220–290 nm wavelength range to retrieve ozone quantities.

[59] One way to derive the surface albedo is to study orbits during which large topographic variations are observed, corresponding to large variations of the surface pressure. This is the case for instance above Olympus Mons: the surface pressure at its summit is ~1 mbar, while it is ~6 mbar at the base of the volcano. This was done and is described by *Perrier et al.* [2006].

5.2. Early South Pole Observations

[60] During the Mars Express mission, early observations of the South polar cap allowed for the first time identification of the clear spectral signature of H_2O ice at the South Pole (simultaneously with OMEGA [*Bibring et al.*, 2004]) and for the first time measurement of the UV albedo of Martian ice. We present here the results which were obtained when flying over the south residual cap, on orbit 30 (18 January 2004). The residual south polar cap is well identified in Figure 21 (a Viking image) by its higher visible albedo: it does not contain the geographic pole, and is rather centered on 87.5° latitude, 320° East longitude. The Mars Express spacecraft was pointed to nadir, and Figure 21 shows the footprint of the fields of view (FOV) of the two spectrometers: circular, one degree diameter for the IR AOTF spectrometer, and rectangular, 0.02 × 0.08° for the UV spectrometer, which project in 42 km and 0.8 × 3 km, respectively. One UV spectrum is taken each second, with light integrated for 0.64 s: the FOV has moved by about 2 km during this time. A full IR spectrum is acquired in 24 s, but each of the 3984 wavelength samples is acquired during 6 ms, giving a negligible spatial lag: each individual IR sample corresponds to a one degree circle, but since the AOTF is sweeping sequentially the wavelengths, the FOV is moving accordingly along the trajectory represented in Figure 21. The circles are represented for the longest wavelength of each IR spectrum. The SPICAM IR spectrum shows clearly the water ice signature, as discussed by *Korablev et al.* [2006].

[61] The Martian season of the SPICAM observation is represented by the solar longitude Ls = 336°, which corresponds to late summer for the southern hemisphere: the seasonal cap of CO_2 has completely disappeared since a long time, and the south pole is still illuminated by the Sun, which allows us to analyze the spectrum of the backscattered solar light. In Figure 22 is plotted the UV reflectance recorded to nadir as a function of acquisition time, showing very strong fluctuations only on the permanent polar cap, with deep troughs corresponding to low albedo channels apparent in the Viking polar cap image (Figure 21), identified by letters a, b, c, d, e, f, g in both Figures 21 and 22.

[62] Over the permanent cap, the UV reflectance is rather high (0.11), much higher than at any other place on Mars, away form polar caps. This is to be compared to the low UV albedo of 0.02–0.03 recorded outside the polar cap. The high value of the reflectance is still much lower than laboratory measurements of pure H_2O or CO_2 ices [*Hapke*, 1981] which indicates that there is also some dust mixed with the icy material of the polar cap, as could be expected from the ubiquitous dusty character of the Martian atmosphere.

[63] Outside the polar cap (from around 210 seconds to 500 seconds after start of observation (Figure 22), the reflectance at 230 nm and at 270 nm is almost the same, which means that ground albedo or dust do not cause strong variation in the spectral reflectance. Over the bright regions, the reflectance increases by a factor 1.6 from 230 to 270 nm. We can assume that the dust/atmospheric conditions are the same between the bright region number 6 and region g just outside the cap: this implies that the strong reflectance variation between 230 and 270 nm is due to ground ice albedo variation with wavelength. Indeed, laboratory mea-

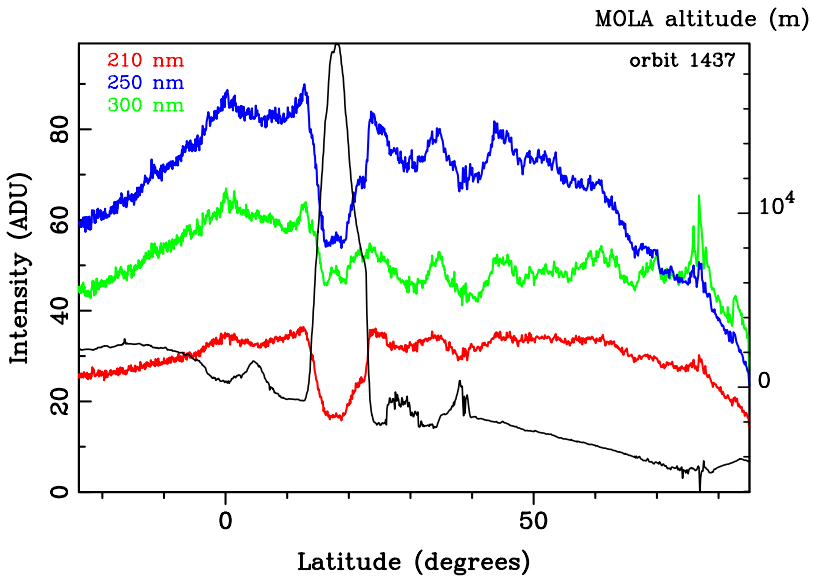

Figure 19. Intensity measured by SPICAM UV (in ADU/CCD line) as a function of latitude during orbit 1437 passing above Olympus Mons at three wavelengths: 210, 250, and 300 nm. In black (right scale) the MOLA altitude of the ground observed at nadir. The signal is decreasing at all wavelengths with increasing altitude on the flanks of Olympus Mons, but the relative decrease is larger at shorter wavelength, which is explained by more Rayleigh scattering at low altitudes (an effect clearly seen from plane on Earth: the ground looks bluish, except over high mountains).

surements of pure H_2O or CO_2 ices UV reflectance [*Hapke*, 1981] indicate a decrease of reflectance between 270 and 230 nm, for both types of ice (which unfortunately does not help to discriminate the type of ice from the UV reflectance spectrum). We can notice that the reflectance at both wavelength is the same in the holes a, b, c, d, e, f, which means that we do not see any ice in these regions, most likely because it is ground similar to outside the cap, where

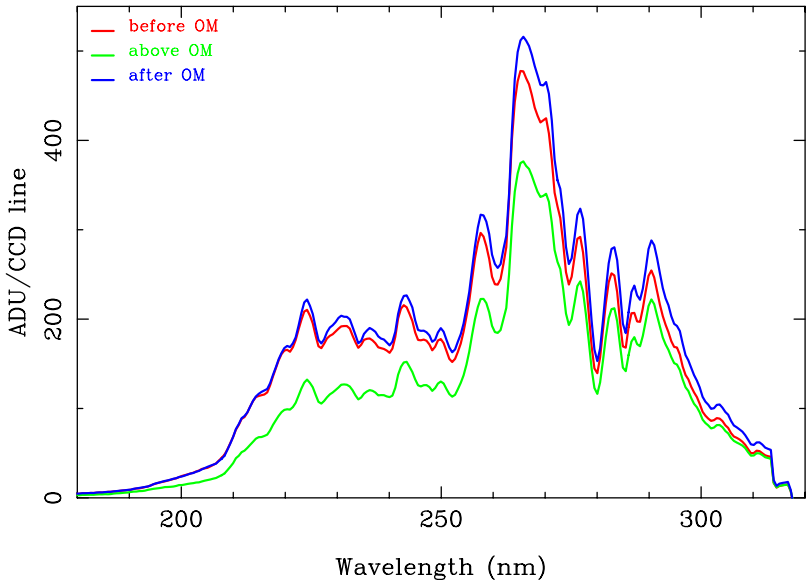

Figure 20. Example of SPICAM recorded spectra in ADU: the shape is dictated by solar spectrum features (the light comes from the solar flux scattered by the ground and atmosphere/dust of Mars), multiplied by the detector sensitivity and affected by the instrumental spectral resolution (both wavelength dependent). These spectra were averaged over the five bands and 20 seconds, i.e., one hundred spectra averaged. They were collected over a crossing of Olympus Mons (OM). The spectrum at the summit (in green) is less intense and less "violet" than those recorded at lower altitudes, before and after Olympus Mons; there is more Rayleigh scattering when observing lower altitudes.

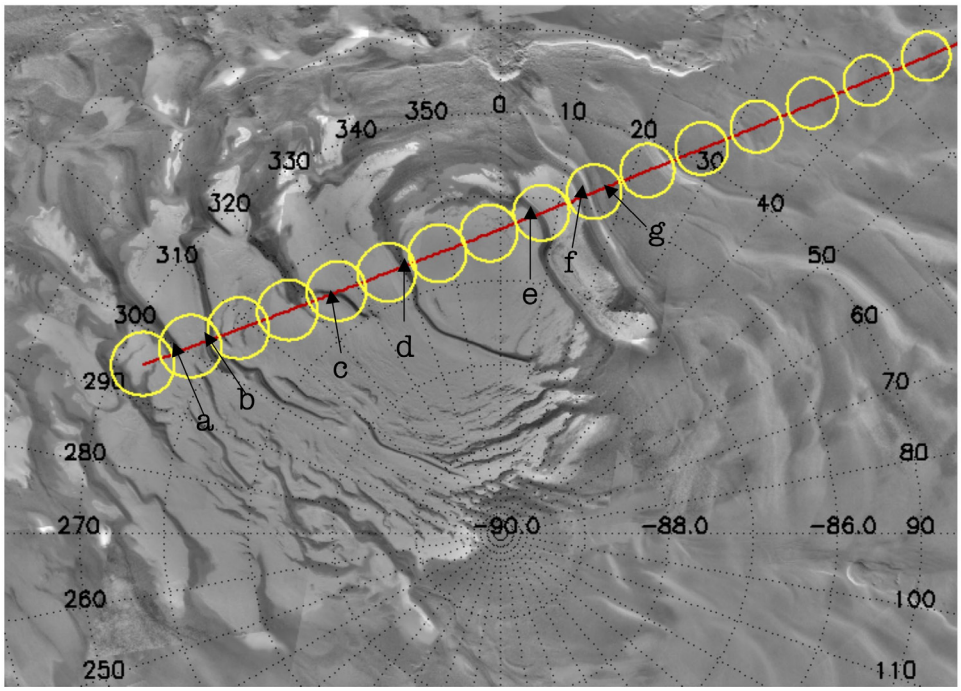

Figure 21. Viking map of South Polar cap. The red line represents the FOV ground track of UV spectrometer, and the yellow circles represent the FOV of IR spectrometer during the nadir observation on 18 January 2004.

also the ground albedo is the same at these two wavelengths. Further systematic UV studies will extend to the North Pole, and to the seasonal caps.

6. Limb Observations by SPICAM UV Spectrometer

6.1. UV Dayglow Observations

[64] They are analyzed in detail by *Leblanc et al.* [2006]. They were obtained with the limb grazing observation geometry on the day side. One difficulty encountered is that these aeronomical emissions are much fainter than the limb emissions of solar light scattered by dust and atmospheric Rayleigh scattering, extending up to ~80 km of altitude. The MCP gain necessary to measure them correctly is high, and might damage the MCP if used also on the dusty bright limb. Therefore two types of limb grazing were scheduled: for the dust limbs, the LOS is such that the minimum Mars Nearest Point (MNP) altitude during the whole observation is 0 km, and the MCP gain is set at a low value. For the aeronomical limbs, the minimum MNP altitude is 80 km, and the MCP is operated at a high gain.

[65] The Mars upper atmosphere/thermosphere/ionosphere (~100–250 km) is an intermediate atmospheric region strongly coupled with the lower atmosphere and coupled above via the ionosphere with the solar wind. The observation of the airglow emission of the upper atmosphere is the only remote sensing method that allows identification of the main parameters of Mars' thermosphere and exosphere and derivation of some elements on Mars' ionosphere (the stellar occultation give CO_2 density measurements up to 150 km only). Figure 9 of *Leblanc et al.* [2006] provides an average of more than 1000 spectra measured in the Martian dayglow obtained by SPICAM, using several selected orbits with limb grazing of the dayglow emissions. Such set of orbits covers a large range of solar longitude, solar activity, local time and solar zenith angle. This averaged dayglow spectrum illustrates the main emissions already identified during Mariner 6 and 7 missions which constitute the dayglow between 120 and 300 nm. The different emissions, their names, sources and spectral range are detailed by *Leblanc et al.* [2006]. Some of them allow us to reconstruct the temperature and density profiles for the CO_2 species, for comparison with thermospheric model.

[66] We also obtained several probings of the atmosphere above 200 km in altitude observing the two main constituents of this region namely H I at 121.6 nm and O I (130.4 nm) atomic species, from resonance scattering of solar photons. O atomic species is typically detected below 500 km, whereas H species can be observed up to several thousands kilometers above the Martian surface. With increasing SZA, the O I emission intensity is decreasing (therefore the density is decreasing much more, because of an optically thick medium), while the scale height is increasing, a rather surprising behavior. Such observations will be analyzed with a global 3D model of the Martian corona [*Leblanc and Johnson*, 2001; *Chaufray et al.*, 2005] and used to constrain models describing the interaction of Mars with the solar wind [*Modolo et al.*, 2005].

[67] For H Lα measurements, the thermal escape, or Jeans escape, is easy to compute, once the exobase density and the exospheric temperatures are determined by SPICAM UV from vertical altitude distribution of H atoms. In theory, it should also be possible to estimate the non-thermal escape, by comparing the exobase density of H at

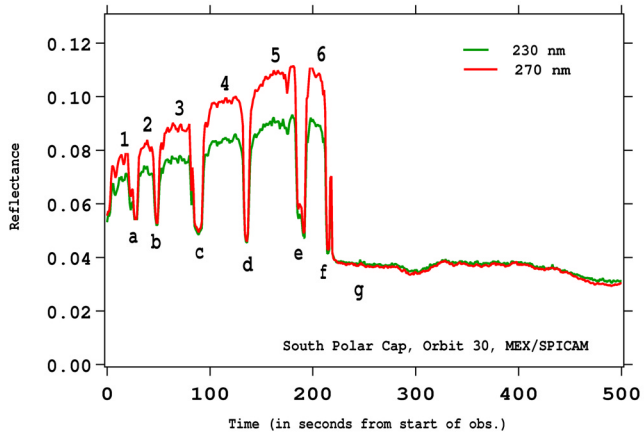

Figure 22. Nadir UV reflectance (radiance/cos SZA) at 230 nm and 270 nm along track over the South Polar cap and farther north (on the left). Letters a, b, c d, e, f, and g indicate regions of low reflectance, both in UV SPICAM data and in the Viking image of the polar cap. The UV albedo is much larger on lobes 1, 2, 3, 4, 5, and 6 of ice identified on the Viking images than outside the cap (region beginning at letter g). While the reflectance at 230 and 270 nm is equal outside the cap and between the lobes, it is lower at 230 than at 270 nm on the lobes, typical of the known signature of ices.

250 km to the vertically integrated quantity of H. Special observations are scheduled in the future to scan the whole exosphere from the apocenter regions. An essential tool to interpret the H and O intensity data is a good radiative transfer model, such as the one developed at Service d'Aéronomie by J.-L. Bertaux and which is presently maintained and improved by E. Quémerais and J. Y. Chaufray, and a model of the interplanetary Lα emission, in order to subtract it from measurements above the limb. For Lα, the limb is defined as the altitude at which the optical thickness of CO_2 (absorbing Lα radiation) is equal to 1, and was found to be at 102 ± 2 km on the night side (see next section). There is also a significant increase of Lα emission when the LOS rises above this limb altitude on the day side, demonstrating that the H Mars corona is not optically thick at this altitude (otherwise, we should see no increase, while a factor of 2 increase is expected for an optically thin atmosphere above a limb).

6.2. NO Bands Emission on the Night Side

[68] In spite of the previous UV spectrometers flown to Mars, up to now nightglow had escaped detection. Thanks to the high sensitivity of SPICAM UV spectrometer, and to the MEX ability to perform grazing limb observations as described above, we have discovered the first Martian night emissions [*Bertaux et al.*, 2005a]. Except for the occasional aurora (see below), the UV spectrum of this nightglow is composed of Hydrogen Lyman α emission (121.6 nm), and of the γ and δ bands of nitric oxide (NO, 190–270 nm, transitions $A^2\Sigma^+ - X^2\Pi$ and $C^2\ \Pi - X^2\Pi$, respectively) produced when N and O atoms combine to produce the NO molecule. This is fully reminiscent of the Venus night side emission. While some UV Venus nightglow had been detected with Mariner 5 [*Barth et al.*, 1967] and Pioneer Venus [*Stewart et al.*, 1979], the first spectrum was acquired with International Ultraviolet Explorer (IUE) and identified as NO radiative recombination [*Feldman et al.*, 1979; *Stewart and Barth*, 1979]. It was proposed that N and O atoms are produced by EUV photo-dissociation of O_2, CO_2 and N_2 in the dayside upper atmosphere, and transported to the night side where recombination occurs, a mechanism later supported by 3D modeling [*Bougher et al.*, 1990] and discussed thoroughly in terms of atmospheric circulation. It is clearly the same mechanism on Mars, with important implications for the Martian atmospheric circulation.

[69] At the time of this observation (orbit 734, 16 August 2004, 07:00 UT), the orbit of MEX had its pericenter on the night side, at an altitude of 266 km, and latitude −16°. The orbit is almost polar, and MEX was descending from north to south (Figure 7). The attitude was fixed in an inertial system so that the line of sight (LOS), aligned with the +Z body axis of the spacecraft, provided a grazing view of the limb while MEX was passing through its pericenter (±10 mn). As a result, the altitude of the tangent point of the LOS (Mars Nearest Point, MNP) changed from 375 km, to a minimum of 15 km and back to 422 km. At the same time, the latitude changed from −11° to −70°. The whole altitude range at the limb was therefore scanned twice, but at different latitudes on the descending and ascending branches. The observations were taken around pericenter of orbit 734, Mars was at a solar distance of 1.66 AU (astronomical units), and the season was L_s = 74°, near the northern summer (southern winter). The spectrometer slit was maintained parallel to the limb at the lowest tangent point. Five band spectra (numbered from 1 to 5, 32 CCD lines binned together) were acquired: the first two with the narrow slit (spectral resolution of 1.5 nm), and 3 other band spectra with the wide slit during each second.

[70] Figure 23 (top) is a color-coded image of the time series of spectra of Band 5 (low resolution). The most obvious spectral features are the H Lα emission, visible at all times, and a broad band emission in the region 190–270 nm, of variable intensity, only present when the MNP altitude is lower than ∼80 km (Figure 23, top). The higher resolution of Band 1 (Figure 23, bottom) reveals a well structured band, whose shapes looks constant. By summing a number of spectra, we obtained the calibrated spectrum (Figure 24), where we identify the γ and δ bands of nitric oxide NO (transitions $A^2\Sigma^+ - X^2\Pi$ and $C^2\ \Pi - X^2\Pi$, respectively).

[71] The light curves of the NO emission rate (Figures 25 and 26) displays two peaks, 350 s and 770 s after the beginning of the observation, the second peak being about 10 times brighter than the first one. Both correspond to a LOS altitude of ∼70 km, but to different latitudes, −35° and −60°, respectively. This behavior can be explained by assuming a locally spherically symmetric NO emitting layer confined to a spherical shell of thickness ∼20 km centered at 70 km altitude, but with a much more intense emissivity rate (photons/cm^3.s) at latitude −60° than at −35°. The emission seen at a tangent altitude below 60 km is essentially produced within the portion of the 60–80 km shell, along the LOS, before or after the MNP point [*Bertaux et al.*, 2005a].

[72] The local emissivity rate of NO UV bands (in photons/cm^{-3}s^{-1}) is proportional to the N and O abundan-

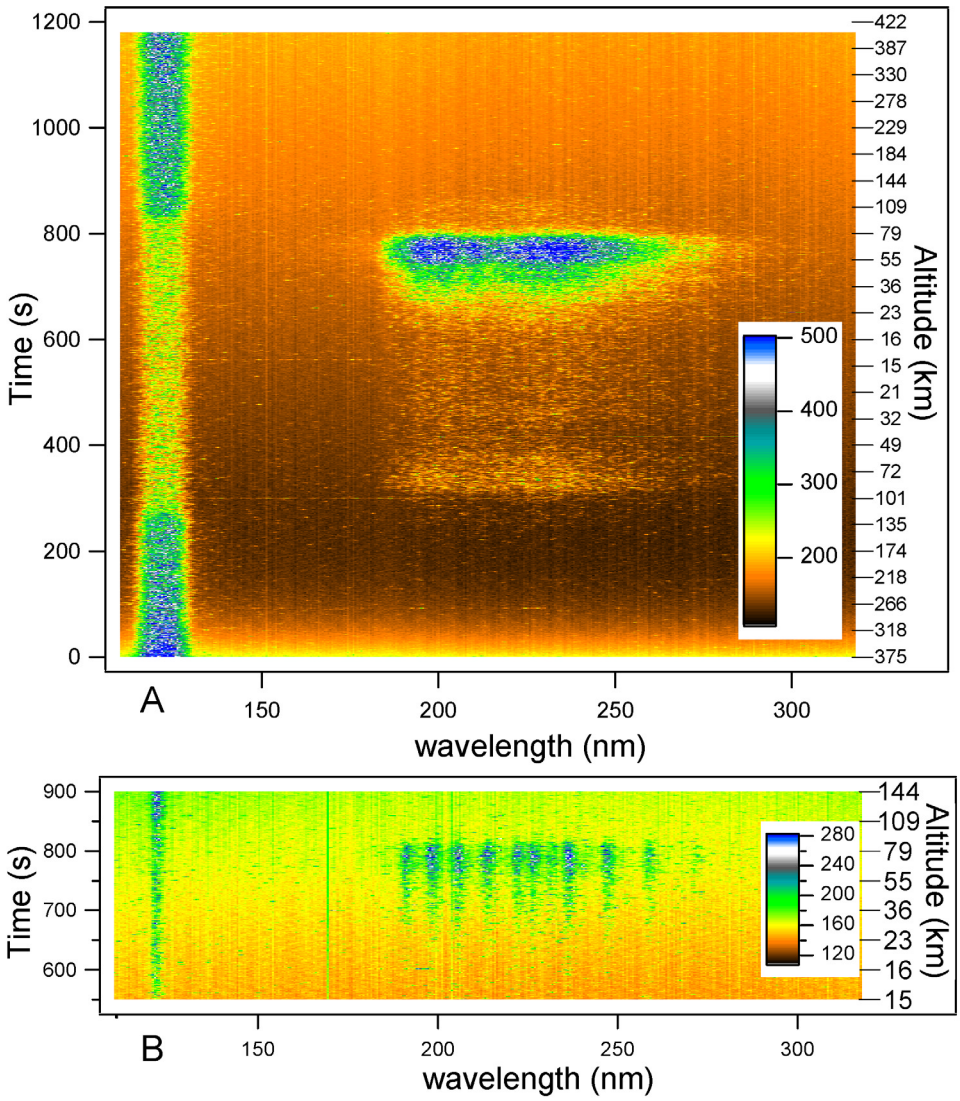

Figure 23. Time variation of the Martian nightglow spectrum along the grazing limb observation. In both figures the intensity is color-coded: these are raw data (ADU/pixel), uncorrected for dark current and radiometric sensitivity. (top) low spectral resolution band 4 (large slit), containing only L emission at 121.6 nm and a broad band extending over the range 190–270 nm. The observation point is going toward southern latitudes, while altitude is going down and up again as a function of time (right scale). (bottom) A subset of simultaneously recorded data at high spectral resolution (~1.5 nm) band 1 (narrow slit), containing only La emission at 121.6 nm and a well-structured band (190–270 nm), identified as NO gamma and delta bands (Figure 24). Some single-pixel vertical lines are artifacts due to pixels with larger dark current (taken from *Bertaux et al.* [2005a]).

ces, [N] and [O]. At the altitude of their formation on the day side, [N] and [O] are too small to give rise to detectable recombination. But when a gas parcel descends, both concentrations increase, and the emissivity rate (photons/cm^3 s) will increase as the product [N] [O], until a significant fraction of [N] (or [O]) atoms are recombined (according to models, the abundance of O is larger than N atoms, so [N] is the limiting factor for the NO emission). This leads to a layer of emission centered at an altitude of 70 km, corresponding to a CO_2 density of 2×10^{14} cm^{-3}.

[73] The NO δ band peak intensity of 2.2 kiloRayleigh (kR) may be used to estimate the downward flux of N atoms in the polar night, found to be $2.5 \times 10^8/cm^2$.s through the z = 80 km altitude level (at the place of the observation [*Bertaux et al.*, 2005a]). Our observations were obtained at L_s = 74°, shortly before southern winter solstice. At this season, the part of the atmosphere where the maximum emission intensity was observed at 70°S is never illuminated by the Sun. Any N and O present there must have been transported from lower latitude where sunlight was available to photo-dissociate N_2, O_2 or CO_2. The observed NO intensity can only be explained by a vertically descending flow in the upper polar atmosphere. This circulation pattern is consistent with prediction from general circulation model of the Martian atmosphere [*Forget et al.*, 1999]. However, this model shows that, at this particular season,

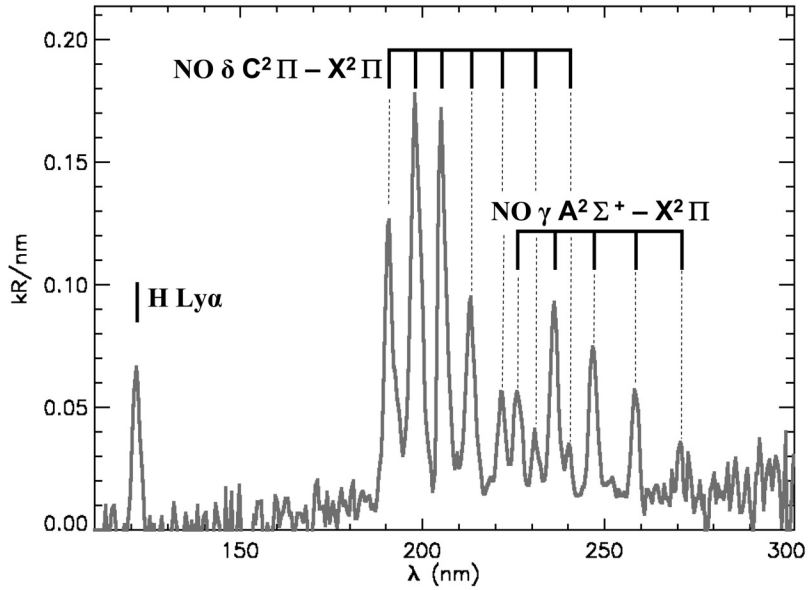

Figure 24. Spectrum of the Martian nightglow obtained during Orbit 734. Except for Lα at 121.6 nm, all the observed lines coincide precisely with the main NO gamma and delta vibrational state transitions responsible for the Venus NO nightglow. The absolute radiometric calibration comes from SPICAM observations of hot UV stars. The total NO intensity is 2.33 kiloRayleigh (kR), with a 74% contribution of the delta band (and 26% from gamma bands). The (0,1) line of the delta band alone is, at 475 R, 27% of the total delta bands. Spectral features above 280 nm could be attributed to the O_2 Herzberg I system, also expected from the recombination of O+O (taken from *Bertaux et al.* [2005a]).

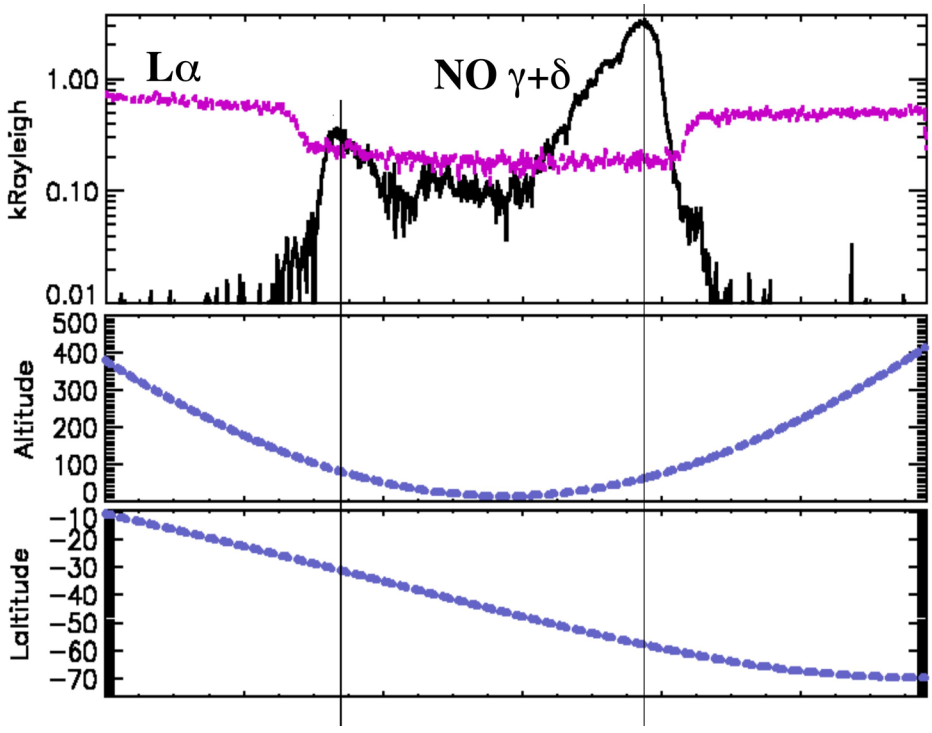

Figure 25. (top) Integrated intensity (wide slit band corresponding to Figure 23, top) of both the Lα emission and the whole NO band from 190–270 nm, as a function of time. (center) Altitude of the tangent point MNP. The NO emission displays two peaks, each time the LOS crosses the 70 km altitude. The second peak is brighter by a factor $\sim$10 and is at high southern latitude. (bottom) Latitude of the tangent point MNP (adapted from *Bertaux et al.* [2005a]).

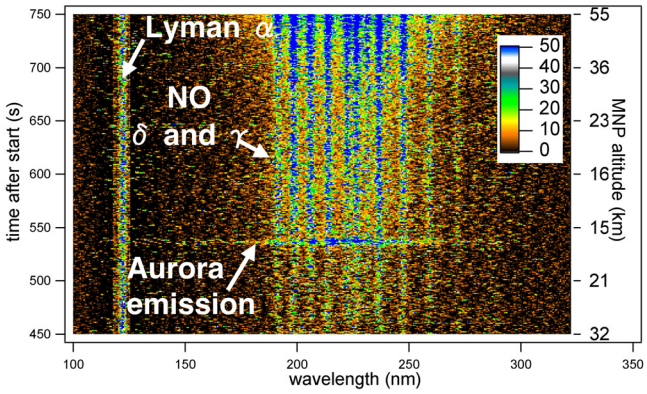

Figure 26. Time variation of the Martian nightglow intensity spectrum recorded during the grazing limb observation with spatial bin 2 (narrow slit, spectral resolution ~1.5 nm, one spectrum per second, data subset from 450 to 750 s after the start of observation). It contains the H Lα emission at 121.6 nm and a well-structured band (190–270 nm), identified as NO gamma and delta bands (Figure 24). The intensity in ADU/pixel (Analog to Digital Units) is color-coded. Altitudes of the Mars Nearest Point of the line of sight are indicated at the right. At the time of the peak marked "aurora" in Figure 27, the spectra are obviously different from the typical NO spectrum.

the circulation around 60 km is modulated by thermal tide waves that propagate from the lower atmosphere and modified by the in situ heating due to the absorption of near infrared radiation by CO_2. These processes are of key importance for our understanding of the upper atmosphere dynamics (and thus for future aeroassistance maneuver, for instance), but they remain poorly understood: numerical simulations results are model dependent [*Forget et al.*, 1999] and few observations are available. Within this context, the NO emission process identified here provides a powerful way to constrain GCM models behavior above 60 km, in conjunction with spacecraft drag measurements [*Keating et al.*, 2003].

[74] In Figure 25 it is seen that the Lα emission is decreased when the LOS is below $\approx$ 100 km, and we may use this information to determine the quantity of CO_2 around this level. The interplanetary Lα emission and the Martian corona Lα emission from H atoms contribute to the observed emission. The Martian Lα emission is solar Lα radiation scattered by H atoms on the day side and transported to the night side by multiple scattering. CO_2 is a strong absorber at Lα, and the atmosphere of CO_2 is opaque to Lα below the altitude at which $\tau = 1$ (optical thickness of CO_2 along the LOS at Lα). Therefore, when the tangent point of the LOS is below this Lα horizon, only the part of the LOS between the spacecraft and this opaque sphere will contribute to the recorded emission. The disappearance of the interplanetary emission and possibly some contribution of the Martian corona beyond the tangential point is seen at times 280 and 820 s. after start of observation, corresponding to the same altitude of 102 ± 2 km, and to a 1.64×10^{19} cm^{-2} CO_2 slant density for $\tau = 1$. This corresponds well to slant density estimates derived from SPICAM stellar occultations (see below) around this altitude; this type of observation is a new method for retrieving the CO_2 density and temperature at each night side limb crossing.

6.3. Discovery of Auroral Emission on Mars

[75] The potential of SPICAM UV spectrometer to monitor weak emissions is illustrated by the first observation of an aurora in the Martian atmosphere, discovered by SPICAM on board Mars Express [*Bertaux et al.*, 2005b]. It corresponds to a new type of aurora not seen before in the solar system: it is unlike auroras at Earth and the giant planets, which lie at the foot of the intrinsic magnetic field lines near the magnetic poles, and unlike aurora at Venus, which is diffuse, sometimes spreading over the entire disc. Instead the Martian aurora is a highly concentrated and localized emission controlled by the crustal magnetic field anomalies.

[76] In the observation quoted here at orbit 716, the SPICAM line of sight (LOS) was permitted to drift slowly across the night side limb to search for any weak emission, as sketched in Figure 7 and similarly to NO observations reported above. Figure 26 is a color-coded image of the time series of high resolution intensity spectra, quite similar to NO observations. The most obvious spectral features are the H Lyman α emission at 121.6 nm, and the well-structured band in the region 190–270 nm of the nitric oxide (NO) molecule.

[77] In Figure 27 the nightglow signal integrated over the wavelength range of the NO bands (181–298 nm) is displayed as a function of time for the 5 spatial bins. The signal is more intense for spatial bins 3, 4 and 5 than for spatial bins 1 and 2 because the FOV is wider and the source is extended. All curves show the same behavior, almost identical to the variation of the NO emission observed six days later at orbit 734 (see above), which is explained by the variation of the altitude and the latitude of the MNP when the LOS scans across the NO emitting layer, confined in the altitude range 60–80 km, and more intense at large southern latitudes (around time 750 s). There is, however, also a strong peak in all spatial bins between times 533 and 540 (increase by a factor 3 to 4) which has no equivalent during orbit 734. The location of the emission could be located by a kind of "triangulation," using the 5 simultaneous FOV of SPICAM UV. It coincides (Figure 28) precisely with the region of strongest crustal magnetic field B reported by Mars Global Surveyor [*Acuña et al.*, 2001], and is the sign of electrons moving along the magnetic field lines, possibly connected to the interplanetary magnetic field at this location and time. The detected horizontal extent of this aurora is 30 km minimum, but it could be more extended along the line of sight. The altitude of the observed emission is 129 ± 13 km. Still, it could extend more vertically, since it was scanned horizontally during the tangential limb geometry. The emissions in the auroral Mars spectrum are the CO $a^3\pi - X^1\Sigma^+$ Cameron band between 180 and 240 nm (694 ± 50 Rayleigh), long observed on the Martian dayside [*Barth et al.*, 1971], as well as emissions associated with atomic carbon resonances and with the CO $A^1\pi - X^1\Sigma^+$ Fourth Positive Group between 135 and 170 nm, emissions associated with the CO_2^+ $B^2\Sigma^u - X^2\pi_g$ doublet at 289 nm (71 ± 42 Rayleigh). Since this first discovery observation, other aurorae have been detected by

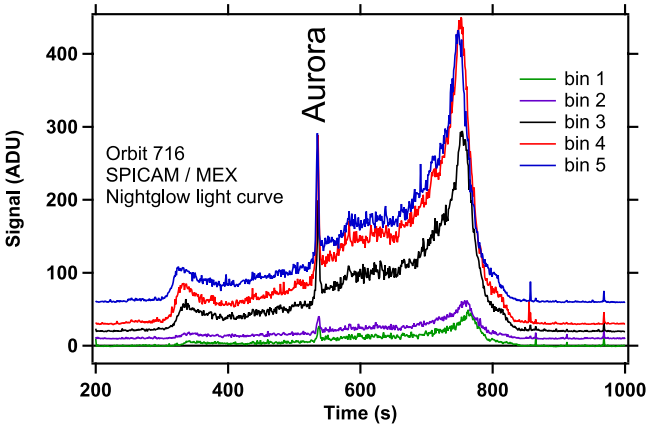

Figure 27. Signal intensity for all 5 spatial bins as a function of time between 200 and 900 s. after the start of observations. Units are ADU per spectral pixel = 0.54 nm, averaged from 181 to 298 nm. There are 40 ADU per detected photon for the particular high voltage used here. The curves for spatial bins 2, 3, 4, and 5 have been vertically displaced for clarity (by 10, 20, 30, and 60 ADU, respectively). Spatial bins 3, 4, and 5 have low resolution but high sensitivity, and bins 1 and 2 are less sensitive but have higher spectral resolution. A conspicuous spike marked Aurora is observed in all bins at time 535 s. This is the time at which the spectra in Figure 28 differ from the usual NO spectrum (adapted from *Bertaux et al.* [2005b]).

SPICAM in several instances, all located in the same region of high crustal anomalies.

7. Atmospheric Vertical Profiling by Stellar Occultation in UV

7.1. General Principles

[78] In the Earth's atmosphere, the occultation technique has been used to measure O_3 since the 1970s. In the early attempts only one or two wavelengths where observed at a time, making the identification of the absorber species uncertain. With the advent of multipixel detectors, in a multispectral occultation the absorbing species can be safely identified due to their spectral signatures. It also offers the potential to discover new, unexpected species in the atmosphere. The method of absorptive occultation spectroscopy was reviewed by *Roscoe et al.* [1994] and *Smith and Hunten* [1990]. In the field of Earth stratospheric research, it has become the most advanced method for long term monitoring of ozone. In the infra-red the most remarkable results are those of ATMOS/Atlas experiment which provided a set of high-resolution IR spectra of the terrestrial atmosphere. In the UV-visible, SAGE-3 from NASA uses a full wavelength coverage on the Sun. On board ENVISAT (ESA, 2001) SCIAMACHY (Scanning Imaging Absorption Spectrometer for Atmospheric Chartography) performs solar occultation and nadir observations, and the GOMOS (Global Ozone Monitoring by Occultations of Stars) instrument is fully dedicated to the monitoring of ozone and other species by stellar occultations (more than 400,000 ozone, NO_2, NO_3 profiles collected up to now [*Hauchecorne et al.*, 2005]).

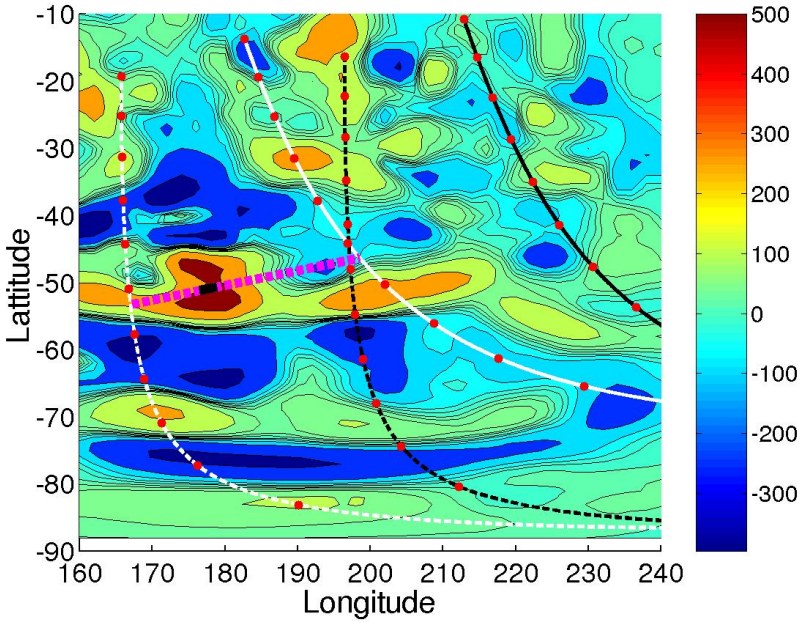

Figure 28. Radial B field component (nT) at 200 km altitude of the crustal field deduced from MGS aerobraking and science phasing orbits [*Acuña et al.*, 2001]. White dashed line: satellite position during Orbit 716 (start at the top and end of the orbit at the bottom of the figure); white solid line: position of the MNP. Dark solid and dashed lines: orbit 734, during which no such emission has been recorded. Magenta dashed line: line of sight of SPICAM at 535 seconds after start. The dark rectangle on the magenta dashed line is our estimate of the extended emitting region (taken from *Bertaux et al.* [2005b]).

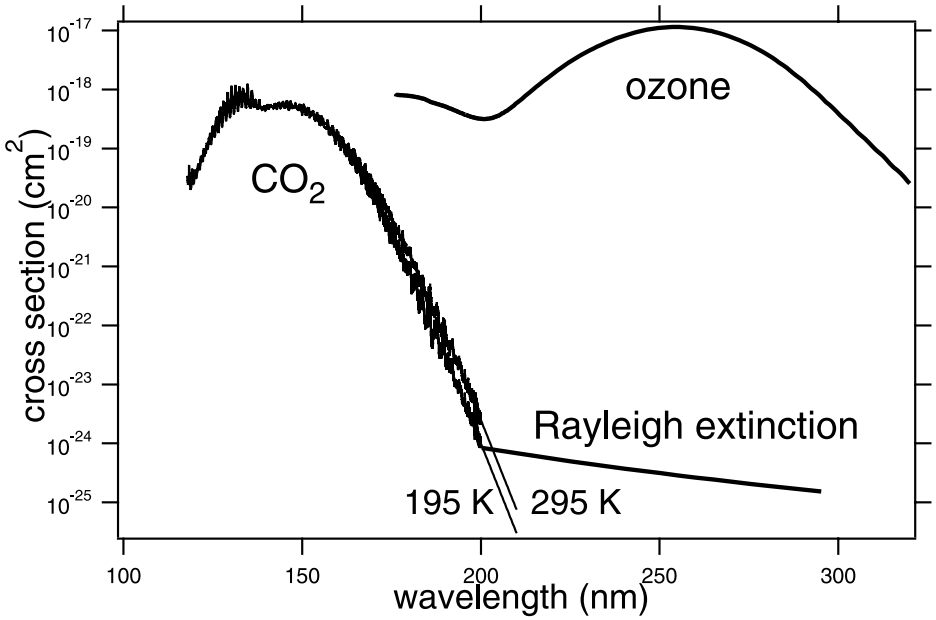

Figure 29. Absorption cross sections of CO_2 and ozone, with Rayleigh extinction of CO_2 in the UV spectral range of SPICAM. The CO_2 cross sections are shown for two temperatures. At 200 nm, it is larger for 295 than 195 K. Aerosols/dust would add to the absorption.

Therefore the methodology of SPICAM is in line with the most advanced instrumentation deployed for the study of the atmosphere of the Earth.

[79] The first and only solar occultation measurements on Mars from spacecraft were performed during Phobos mission with the Auguste instrument [*Blamont et al.*, 1989; *Krasnopolsky et al.*, 1989]. Though the Phobos mission was not fully successful, the solar occultation studies were performed during a period of more than one month, resulting in an important impact on our knowledge about Martian water vapor profile [*Krasnopolsky et al.*, 1991; *Rodin et al.*, 1997], aerosol vertical distribution [*Chassefière et al.*, 1992; *Korablev et al.*, 1993], and ozone distribution [*Blamont and Chassefière*, 1993]. The promising results provided by the Phobos mission were not fully developed because of the failure of the Mars 96 mission.

[80] SPICAM is the first instrument to perform stellar occultations on Mars, and it routinely delivers vertical profiles of CO_2 density, temperature, ozone (O_3), aerosols, by measuring the atmospheric transmission as a function of wavelength in the occultation geometry, as it was originally planned on Mars 96 with SPICAM. The methodology is to use the spectral absorption properties of atmospheric components to retrieve their vertical distributions, as described by *Korablev et al.* [2001] with simulated data and inversions. The SPICAM UV spectrometer covers the wavelength range 110–300 nm, which encompass the whole CO_2 absorption band (110–200 nm), and the ozone Hartley band centered at 250 nm (Figure 29). Dust is absorbing everywhere, but is easier to see above 200 nm, clear of the CO_2 absorption.

[81] The principle of a star occultation to measure the atmospheric transmission is quite simple (Figure 30). Along its orbit, stars are occulted one after the other by the planetary limb opposite to the velocity vector. At a predetermined time, the spacecraft MEX is oriented in such a way that the line of sight (LOS) of SPICAM UV is pointed toward a given star. Its spectrum recorded above the atmosphere (say, at 200 km), unaltered by atmospheric absorption serves as a reference spectrum $F_0(\lambda)$. Then, while the spacecraft is maintained on a 3-axis, inertial attitude, the line of sight S/C to the star intersects deeper and deeper parts of the atmosphere, down to total occultation. Each second, the spectrum $F(\lambda, z)$ is recorded when the line of sight goes through the atmosphere, at a tangent altitude z. The atmospheric transmission at altitude z is

$$T(\lambda, z) = F(\lambda, z)/F_0(\lambda)$$

[82] The first step of the data processing is to establish the transmission by correcting from instrumental effects (i.e., the CCD Dark Charge) and some background light sometimes present at the limb.

[83] The second step is to fit the measured transmission at each altitude by a simple forward model (spectral inversion):

$$T_{mod}(\lambda, z) = \exp(-\sigma_{CO2}(\lambda) * N(CO_2) - \sigma_{O3}(\lambda) * N(O_3) - \tau_{dust}(\lambda)) \quad (1)$$

where $\sigma_{CO2}(\lambda)$ and $\sigma_{O3}(\lambda)$ are the cross sections of CO_2 and ozone, respectively, $N(CO_2)$ and $N(O_3)$ are their slant density (local density integrated along the line of sight), and $\tau_{dust}(\lambda)$ is the optical thickness of dust, described by one or two parameters as a function of λ.

[84] The third step is to perform the vertical inversion of the slant densities, to retrieve the local densities by a modified onion peeling technique, including Tikhonov's regularization inspired from GOMOS work.

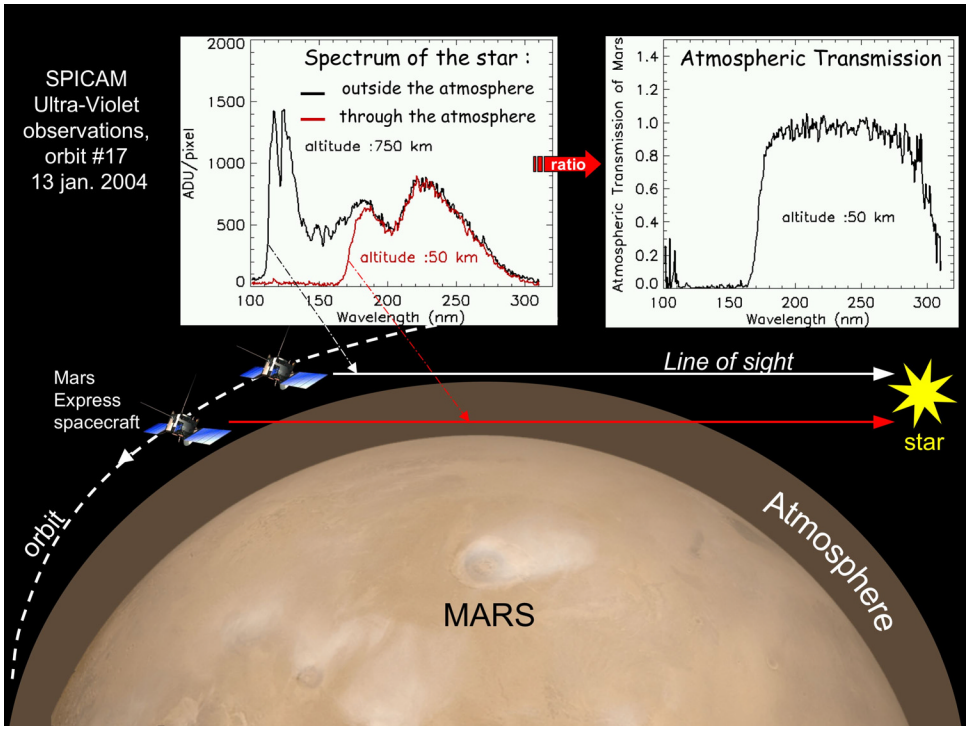

Figure 30. Schematic sketch of an occultation. From the two spectra obtained outside and through the atmosphere, an atmospheric transmission can be derived. Displayed spectra come from the very first stellar occultation made by SPICAM at the beginning of the mission, which is also the very first made by any instrument orbiting around Mars. Shortward of 180 nm, the signal is completely attenuated by CO_2.

[85] From the retrieved CO_2 density, the vertical profile is integrated from the top to yield the pressure, and the law of perfect gases is applied to determine the temperature. The CO_2 density is retrieved from about 150 km down to 10–30 km, depending on the dust load in the lower atmosphere, where the star signal disappears. For solar occultations, a lateral viewport is used, and 5 points on the Sun are recorded together, allowing retrieval of 5 profiles at each occultations which can be merged together.

[86] We will present some details of each of the three steps, both for stellar occultations and solar occultations, and some statistics on the observations which have been obtained so far with Mars Express. An expected finding is that star occultations on the deep night are preferred, because of minimal limb light background.

[87] The stellar occultation technique offers three decisive features:

[88] 1. An absolute concentration derived from a relative measurement (no need of instrument calibration, self calibrated method).

[89] 2. Excellent vertical resolution, whatever is the distance to the planet (because the star is a point source).

[90] 3. The accuracy of altitude knowledge, at variance with limb emission methods, is independent of the attitude of the spacecraft. The LOS is entirely determined by the direction of the star in the sky (known) and the position of the S/C on its orbit.

[91] Stellar occultations are done preferably on the night side of the orbit, and do not affect the operation of dayside mapping instruments. The spacecraft is commanded in order that the line of sight of SPICAM UV is oriented toward a bright UV star and maintained with this fixed orientation during the whole occultation which lasts typically 1–4 minutes (SPICAM is ON for 20 mn).The factor limiting the number of occultations is the spacecraft orientation as a resource to be shared between the various MEX investigations.

[92] Several features must be mentioned:

[93] 1. When a star is occulted at one orbit, the same star will be occulted during the following orbits at about the same latitude, but at a different longitude.

[94] 2. The vertical profiling is not at all restricted along the track of the spacecraft, at variance with other instrumental methods.

[95] 3. Hot stars are preferred, because they are brighter in UV. Their spectrum is flatter in UV than the solar spectrum, with more UV than the Sun below 200 nm, and stellar occultations may probe therefore higher altitudes than solar occultations.

[96] 4. De-occultation (stellar rise) is also possible, since there is no closed-loop star tracking system.

7.2. Observation Description

[97] Since the very first occultation sequence made on 13 January 2004, more than 500 profiles have been collected by SPICAM. Some sequences were lost due to a contamination of the star signal by the proximity of the Sun illuminated terminator. Indeed night side occultations are made without the spectrometer slit. It was found that contamination was too severe when the SZA at the point of occultation (the MNP) was <105–110°. When the contamination is small, it may be subtracted from the star signal,

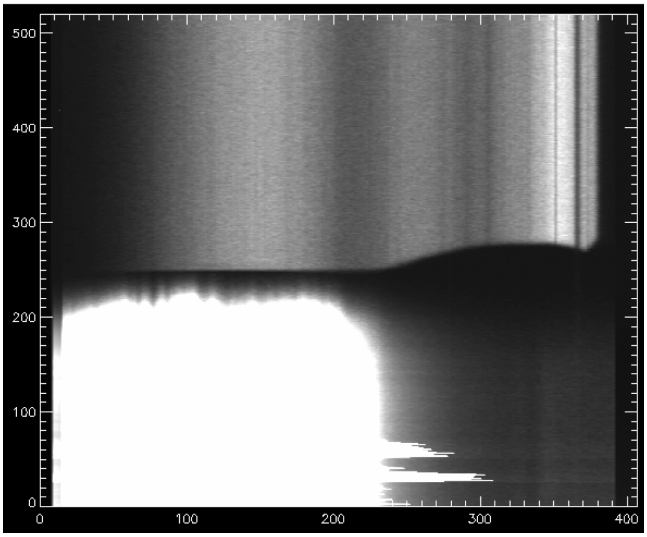

Figure 31. Data obtained in the central band during a day side de-occultation at orbit 1113. The observed star was Delta Scorpii, and its image was put in the narrow slit of the UV spectrometer. The data are presented as a tempo-spectrum image: each line (1 Hz sampling) is the spectrum recorded in the detector band containing the star. Time and altitude are increasing upward. Signal intensity is gray-coded from dark to white. Horizontal scale is in pixel number (wavelength goes from 310 nm at left to 110 n at right). At low altitudes, the bright limb signal is saturating the detector in the near UV, but the star is not seen either in the far UV, because of CO_2 and dust absorption. The star signal appears above $\sim$70 km of altitude and is no longer contaminated by the bright limb, providing useful information. Narrow vertical dark stripes are Fraunhofer lines of the star spectrum, the most conspicuous being at Lyman α. The CO_2 absorption shape is distinctly seen below 200 nm (pixels 250 to 390). Note the increased absorption shortward of 122 nm (pixel number 370), which is a known feature of CO_2 absorption cross section (not represented in Figure 29).

since it is measured in 4 bands, 2 above and 2 below the star spectrum [see *Quémerais et al.*, 2006]. A number of 412 other occultations could still be treated and yielded vertical profiles of atmospheric species, CO_2, ozone, and aerosols. The data set spans a period comprised between the end of northern winter (at Ls = 330°, which corresponds to the arrival of Mars Express at Mars) and the beginning of northern fall (Ls = 200°). More observations have been performed in the southern hemisphere, as shown in Figure 3 of *Montmessin et al.* [2006a], illustrating the latitude-season distribution. This bias is due to the uneven distribution of UV bright stars in the sky and to the MEX orbit geometry.

[98] We have proven that the pointing accuracy and stability of MEX (at least, before the Marsis antennas deployment) is usually so good that we can put the star image inside the 50 μm slit of SPICAM (0.02°),while the specified absolute accuracy was 0.1°. Figure 31 illustrates one of the few occultations performed on the day side, with the spectrometer slit in place. While the bright limb is saturating the detector at low altitudes, it is seen that useful transmission measurements may be obtained above $\approx$50 km.

[99] Results of stellar occultations from MEX have been presented at a number of conferences. *Quémerais et al.* [2006] describe the actual data and inversion processes, *Montmessin et al.* [2006a] describe the cloud and dust distributions, *Forget et al.* [2006] describe the CO_2 density and temperature measurements, and *Lebonnois et al.* [2006] describe the ozone results. A brief summary of these three topics are presented below.

7.3. CO_2 Density and Temperature Profile

7.3.1. Thermal Structure of the Atmosphere of Mars

[100] Theory tells us that the temperature structure of the thermosphere above 120 km is dominated by the balance between EUV heating, non-LTE cooling, and molecular diffusion. In the middle atmosphere (40–120 km) the vertical structure is determined primarily by non-LTE solar heating and radiative cooling in the absorption bands of CO_2, and by solar EUV heating at higher levels. The thermal structure is modified by the circulation driven by this forcing, and by tides and gravity waves that propagate from the lower atmosphere, break, and deposit their energy in this region. Lower and upper circulation models (including GCMs) have recently been extended into the middle atmosphere, and need adequate temperature/density data to be validated.

[101] Until recently, there were few temperature profiles in the upper atmosphere of Mars: Viking Landers entry profiles [*Seiff and Kirk*, 1977], and an indirect derivation above 120 km from Mariner 9 airglow [*Stewart et al.*, 1972]. New profiles were derived from Mars Pathfinder (MPF) entry accelerometry [*Magalhães et al.*, 1999] and Mars Global Surveyor (MGS) aerobraking data [*Keating et al.*, 1998]. Thermal Emission Spectrometer (TES) on MGS produces 3-D fields of temperature up to 35 km in nadir mode and up to 65 km in the limb-viewing mode [*Conrath et al.*, 1998, 1999]. Radio occultation studies from Mars probes (including Mars Express RadioScience) result in profiles below 20 km (see *Hinson et al.* [1999] for some MPF radio profiles). Ground-based microwave observations based on CO lines profiling [*Clancy et al.*, 1989] constrain temperature profile on large (planetary) scales up to $\approx$50 km. Yet, the thermal structure and the circulation of this part of the atmosphere is of primary importance on Mars: unlike on Earth, where the circulation in the troposphere is somewhat decoupled from the circulation in the stratosphere, the vertical extension of the meteorological phenomenon on Mars appears to be considerable. In some case, this extension probably reaches the top of the neutral atmosphere around 120 km (e.g., the Hadley cell during northern winter). The circulation there may even affect the meteorology at much lower altitude [*Forget et al.*, 1996]. For instance, the strong warming of the polar night atmosphere during dust storm is thought to result from an enhancement of the meridional wind between 60 and 100 km [*Wilson*, 1997]. In fact, this behavior of the Martian atmosphere may limit the performance of the general circulation models and thus our understanding of the Martian meteorology. How can we account for these upper atmospheric processes? Is the lower thermosphere circulation of importance? Because of their limited vertical cover-

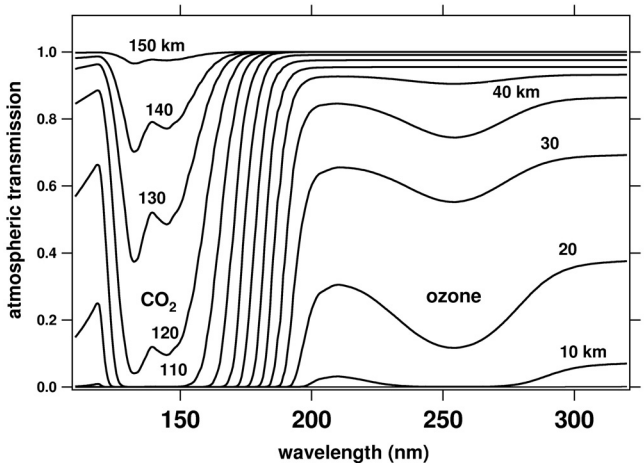

Figure 32. Synthetic spectra of Mars atmosphere transmission in occultation for various grazing altitudes. Dust is taken into account here, most visible as a continuous and sloppy absorption above 210 nm, and ozone is present as an absorption trough clearly visible at 30 and 40 km of tangential height. The curve at 30 km may be compared to the actual measurements of Figure 45.

age (<65 km), TES and similar instruments cannot solve the problem, leaving SPICAM to be a single optical spectroscopy experiment covering this altitude range.

7.3.2. Data Analysis

[102] Because the CO_2 cross section presents a very large dynamic range in the UV, the CO_2 absorption may be detected already up to an altitude of 150 km. For decreasing tangential heights, CO_2 manifests itself by a sharp cutoff which increases in wavelength, up to ≈200 nm at z = 80 km (Figure 32). Longward of 200 nm, the transmission spectrum is dominated by dust and CO_2 Rayleigh extinction, with the additional trough at 255 nm due to ozone when present. The depth of this trough is a direct measure of ozone line density. The Rayleigh extinction above 200 nm can be computed from the CO_2 line density determined below 200 nm, and the remaining continuous absorption above 200 nm may be attributed to ozone if present and to dust/aerosol for a determination of its vertical distribution and spectral characteristics in the UV, as illustrated by SPICAM/MEX actual measurements (Figures 33 and 34) for two different altitudes.

[103] Once the slant density of CO_2 is determined from the transmission spectra for each altitude (one altitude per second), the local density n(z) is determined from an Abel vertical inversion of the slant density vertical distribution during one single occultation. Then, the hydrostatic equation allows temperature to be determined [*Quémerais et al.*, 2006]. Figure 35 is an example of density retrieval in the atmosphere of Mars, where the PFS/MEX data have been also plotted (courtesy D. Grassi and V. Formisano), illustrating the good agreement, but also the complementarity of both sets of measurements as a function of altitude. There is some dependence of the CO_2 absorption cross section on temperature T; the retrieval process in this case is more complicated, and we have ignored this effect up to now.

[104] Though nighttime stellar occultations are preferred, it is important to keep in mind that some daytime occultations may also be performed on especially bright stars on the bright limb. SPICAM is thus offering a fair cover of density/temperature profiles as a function of local time, latitude, geography and solar activity: a sampling which is a crucial test for the validity of sophisticated thermospheric GCM models. Once validated (or invalidated, and modified accordingly), such models could be used as a predictive tool for managing aerocapture/aerobraking operations in future.

[105] Figures 36 and 37 are examples of two slant density profiles compared to the prediction of the GCM model from LMD [*Forget et al.*, 1999] run for the same time and location. We note in Figure 36 a significant drop in the data at altitudes >100 km, not predicted by the model, while in Figure 37 the agreement with the model is much better at high altitudes. For a while, we suspected that the discrepancy could come from our neglect of the variation of CO_2 cross section with temperature for this very cold region (a small scale height of the slant density implies a low temperature). However, in such a case, there would be a systematic discrepancy, which is not the case. In addition, high altitude clouds have been detected in some occasions (see below), always correlated with low temperatures at high altitude. Therefore we estimate that the profile of Figure 36 is real.

7.3.3. The Case for Molecular Oxygen O_2

[106] This molecule is one end product of CO_2 photodissociation, by recombination of O atoms in the lower atmosphere. Its abundance is about 0.13% at the surface [*Owen et al.*, 1977], but nothing is known about its vertical distribution, which would be an excellent test of chemistry-dynamic models. In principle, one expects a constant mixing ratio of O_2, in altitude and over the planet, inasmuch as we understand the chemical reactions that control this molecule. The O_2 Schumann-Runge bands (170–210 nm) provide an additional absorption that should be detectable in stellar/solar occultations. Calculations show that the difference of transmission between an atmosphere with O_2 ($O_2/CO_2 = 10^{-3}$) and an atmosphere without O_2 amounts to 2% around 80 km, in a bandwidth of about 20 nm around 190 nm. The amount of absorption decreases somewhat below. The UV occultation technique is one way to access this important molecule. Though on Mars there is a conspicuous O_2 emission at 1.27 μm, this emission is produced by photo-dissociation of ozone. It does not trace the density distribution of O_2 as would the UV absorption seen in occultation. However, we have not yet processed the data in sufficient detail to detect O_2 so far.

7.4. Stellar Occultation Results: Aerosol Vertical Profiles

7.4.1. Impact of Aerosols on Martian Climate

[107] An important component of the Martian atmosphere is dusty and volatile aerosol (water ice and CO_2 ice cloud particles). Because of the strong involvement of the aerosols in basic climate fields, the lower Martian atmosphere may be considered as a "dusty climate" system. A permanent haze exists with a column optical depth from 0.1 to 1 in the visible, depending on season, with sporadic increases up to several units during great dust storms, and it is known to control temperatures in the troposphere and lower stratosphere. Heating and cooling by aerosols drive dynamical phenomena, varying on scale from general circulation to

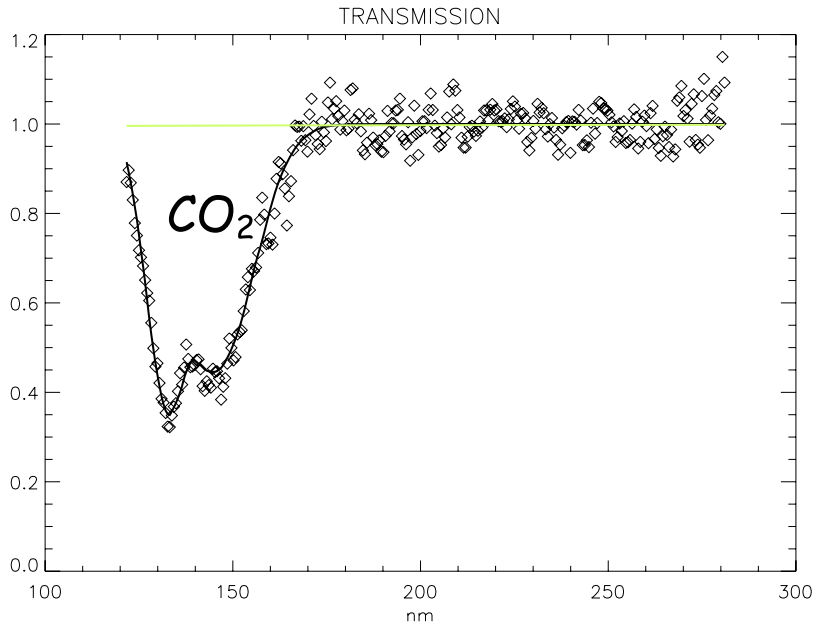

Figure 33. SPICAM/MEX measurements of spectral atmospheric transmission during one stellar occultation at high altitude, where only CO_2 absorption is present.

local waves that give rise to the atmospheric turbulence. The content and distribution of aerosols in the atmosphere are in turn controlled by atmospheric motions, being included in the complex feedback that makes current climate of Mars extremely variable. Volatile aerosols also affect the thermal field by changing optical properties and settling rates of particles, and therefore provide strongly nonlinear thermal feedback determined by saturation curve, which effect is expected to be most significant during aphelion period [*Clancy et al.*, 1996; *Rodin et al.*, 1999]. Water vapor may be often saturated, and may experience a diurnal cycle as the temperature profile does in the lower atmosphere [*Hinson et al.*, 1999], with a substantial decrease at night, possibly yielding water ice condensation. However, even above saturation, the potential formation of icy grains (cloud particles) may depend on the abundance, the size and the nature of dust particles serving as condensation nuclei. A companion paper [*Montmessin et al.*, 2006a] analyzes the main findings of SPICAM stellar occultations about dust and cloud particles. Only a short summary is

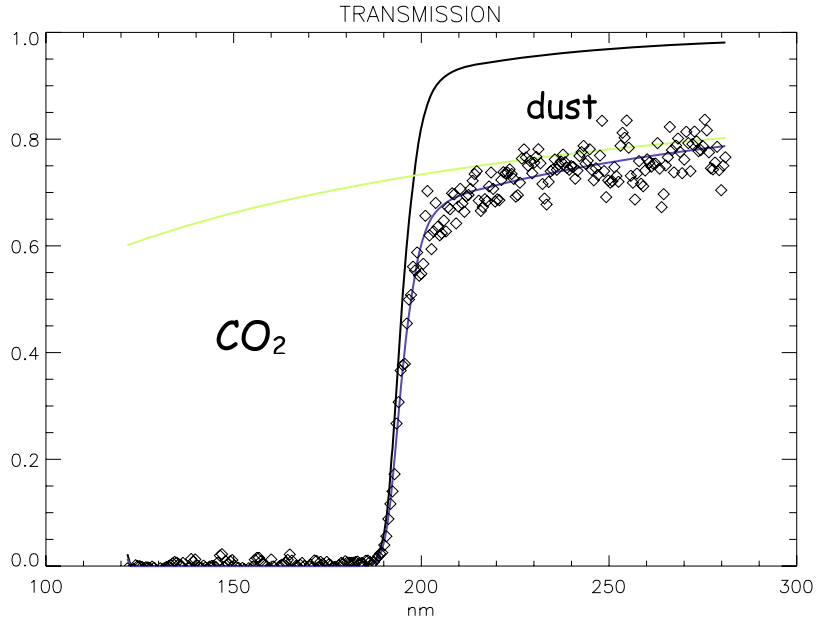

Figure 34. Same as Figure 33, but lower in the atmosphere. The green curve is the absorption attributed to aerosols necessary to fit the data, in addition to CO_2 absorption and Rayleigh extinction. In this particular case, there is no ozone.

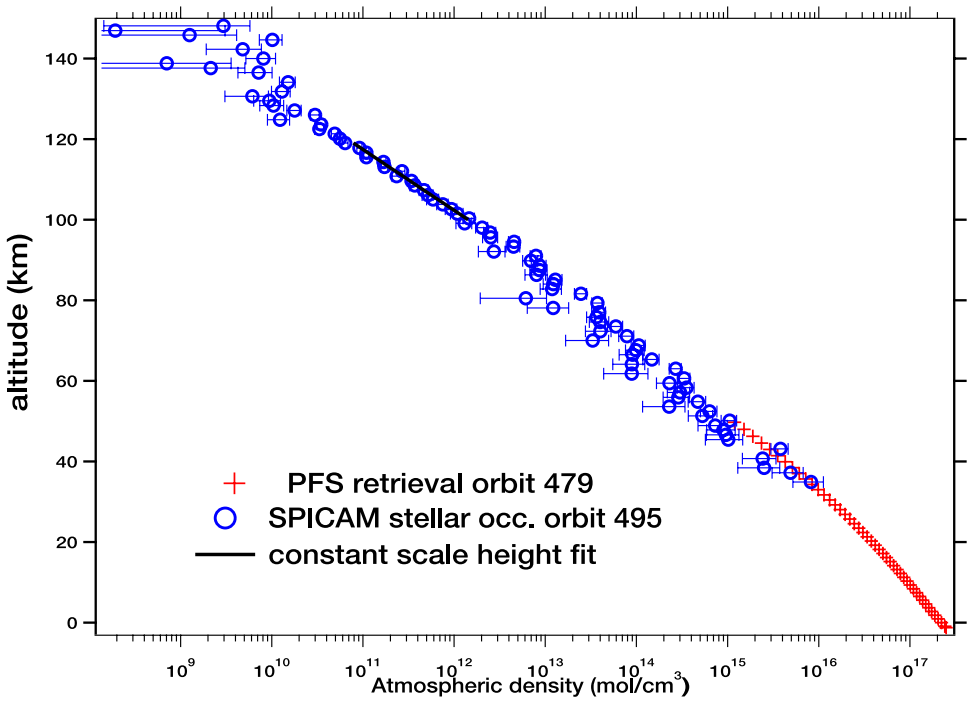

Figure 35. Example of density retrieval in the atmosphere of Mars, where the PFS data have been also plotted (courtesy D. Grassi and V. Formisano), illustrating the good agreement, but also the complementarity, of both sets of measurements. The PFS air temperature fields are retrieved in the range 3–45 km above the surface by means of numerical inversion of the radiance observed in the CO_2 15 μm band, performed on a single-spectrum basis. Resulting profiles have a vertical resolution in the order of some kilometers, intimately limited by the nature of radiative transfer. The SPICAM vertical profile is obtained by stellar occultations at a nearby orbit. The vertical profiles of PFS and SPICAM are overlapping in the region 30–60 km, showing a good agreement of both retrievals.

presented below, following a short description of the observations.

7.4.2. Observation Description and Data Analysis

[108] While aerosols/dust may be observed on the day side from their emission of scattered solar light [*Rannou et al.*, 2006], the stellar occultation technique remains unique to detect condensation clouds during the night, in addition to plain dust particles. For each occultation, the ratio of spectra taken through and outside the atmosphere gives an atmospheric transmission at each altitude (the altitude being referred to the distance of the MNP to the reference ellipsoid of Mars, and not the altitude above the point on the surface that is closest to the slant). If there is any absorbing or/and scattering species along the optical path between the star and the spacecraft, photons are lost and resulting transmissions are lower than 1. In many occasions, there is an altitude at which the transmission goes through a local minimum at all wavelengths simultaneously. This is the distinct signature of an enhanced layer of dust or cloud particles. Figure 38 shows an extreme example, where 4 discrete layers may be readily identified in the transmission data. At high altitude (z > 150 km), there is no absorption. The structure of CO_2 absorption is clearly visible in the range 120–180 nm.

[109] As previously mentioned, each transmission spectrum is fitted by the representation of equation (1), where the retrieved parameters are the LOS integrated (slant) molecular concentrations of carbon dioxide, ozone and the opacity created by aerosols along the line of sight, mostly visible between 200 and 300 nm. We found out that the spectral signature of the dust extinction was variable: therefore the slope between 200 and 300 nm was fitted by a power law of the form [*Montmessin et al.*, 2006a]

$$\tau_{\mathrm{dust}}(\lambda) = \tau_{250}(250/\lambda)^{\alpha} \qquad (2)$$

where the exponent α on the left side of equation (2) is the Angström coefficient (empirically connected to the particle's size in Mie scattering simulations), λ is expressed in nanometers and $\lambda = 250$ is a reference wavelength, chosen in the middle of the interval of observation of the dust (or cloud particle) extinction (the fact that ozone absorption is maximum around this wavelength is of no relevance here). Figure 39 shows the measured spectral transmission at 3 altitudes, a high altitude cloud being detected at 98 km, where the transmission is lower than at 96 km. Each spectrum is fitted by the formula (2), and there is here an obvious variation of the slope of the aerosol extinction versus wavelength.

[110] Values returned for each parameter (τ_{250} and the Angström coefficient α for aerosol) are plotted as a function of altitude, allowing already a comprehensive picture of the variety of profiles [*Montmessin et al.*, 2006a, Figure 8]. They can also be inverted to determine the resulting vertical

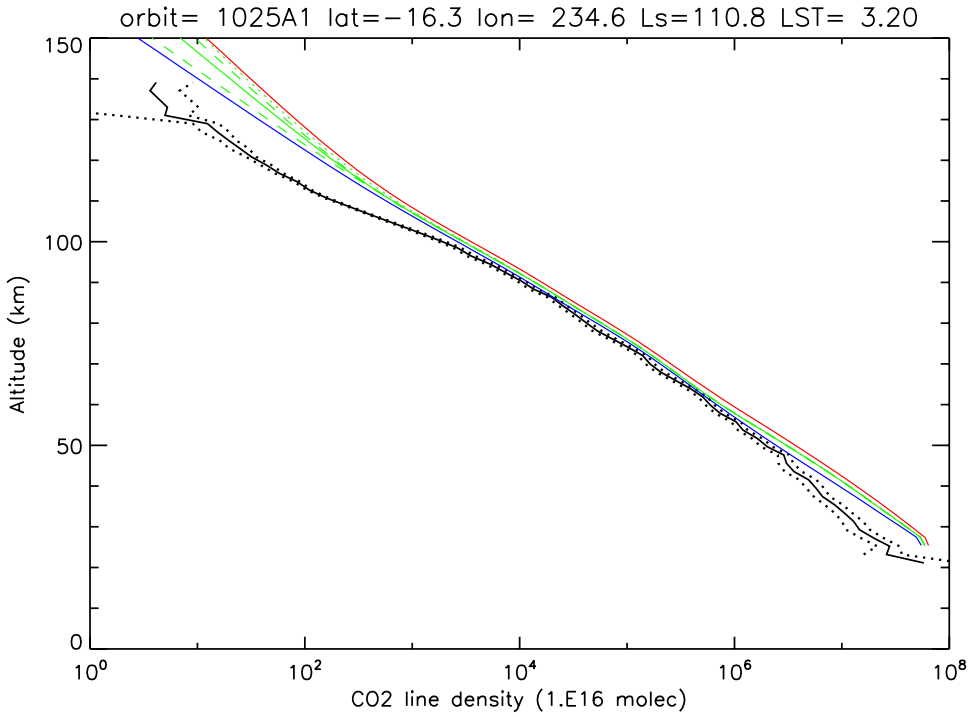

Figure 36. Comparison of measured slant density profiles with the prediction of the GCM model from LMD [*Forget et al.*, 1999] run for the same time, geometry, and location. The black line is the SPICAM data, with dotted lines at ± error bar. Several models are compared. Blue: clear (no dust); green: MGS scenario; and red: dusty atmosphere. There is a significant deficit of CO_2 above 100 km in the data, which is usually not present on other orbits (Figure 37), indicating a low temperature in the region 100–110 km.

distribution of local extinction by aerosols: the concentration of aerosol can then be derived, if a cross section is assumed.

7.4.3. Summary of SPICAM Findings for Aerosols in Stellar Occultations

[111] In Figures 40a and 40b we present two different profiles of dust opacity, together with Angström coefficient. The vertical structure of the opacity is quite different, each of them being typical of its class. On the left, the profile taken at 17° of latitude is typical of equator and mid latitudes. The haze opacity is high (>4) up to 30 km and then decreasing with increasing height, with a substantial detached layer peaking at 55 km. At some other points, there may be several detached layers (up to 3). On the contrary, all profiles captured in the polar region show no detached layer (Figure 40b, right), a much lower opacity at all measured altitudes (∼1 at 20 km), and a profile decreasing rather fast with increasing altitude. As discussed by *Montmessin et al.* [2006a], this type of vertical profile is consistent with a lack of convective activity, while some studies conducted in a theoretical framework have concluded on the possibility of CO_2 storms in the polar night due to the brutal release of latent heat during atmospheric condensation episodes. The SPICAM observations do not support the existence of such meteorological phenomena. It should be recognized that while limb imaging allows us to detect dust and clouds on the day side, the stellar occultation technique uniquely allows us to monitor dark regions. This is of particular interest since a most important feature of Mars climate happens in the deep polar night, when a substantial fraction of the whole atmosphere condenses on the ground. Unfortunately, this aspect of the Martian climate is incompletely documented. Temperatures have been retrieved from IR measurements, but almost no observation could be used to infer the haze vertical structure in these regions. Yet, modeling show the importance of aerosols in the polar nights to control the intensity of planetary-scale waves propagating in the midlatitudes of both hemispheres during fall and winter. The SPICAM data is therefore unique in the polar night regions, and will be of great value for climate models which predictions are strongly sensitive to assumptions on the aerosol loading and vertical structure in these regions.

[112] In addition, we have analyzed the seasonal evolution of the Martian haze top (maximum height at which particles can still be observable) as observed with SPICAM stellar occultations. The presence of a strong seasonal signal is clearly detected, with the haze gradually losing altitude as one penetrates deeper into colder-regions. This is the result from two separate, yet combined, effects: (1) the stronger convection prevailing over sunlit terrains and (2) the lower altitude of the hygropause following the cooling of air masses. With the second effect, the formation of water ice clouds is favored at lower heights, and the subsequent scavenging of dust particles above the hygropause results into the visible lowering of the whole haze layer. A more complete discussion is presented by *Montmessin et al.* [2006a], who find also an interesting relationship between the vertical gradient of Angström coefficient α and the vertical gradient of the slant opacity. It indicates that layers

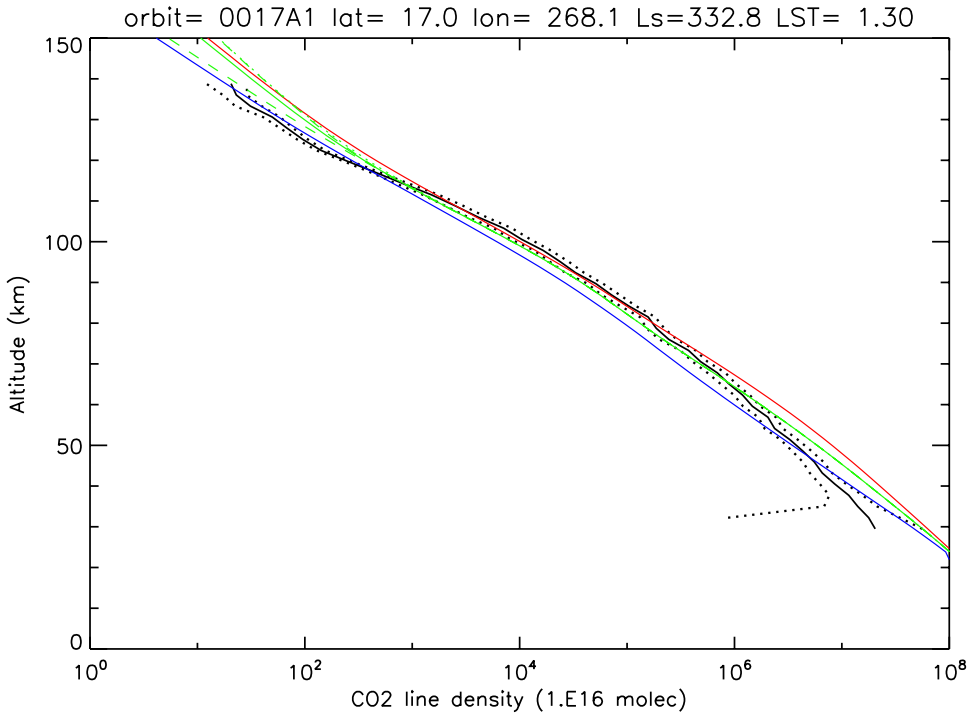

Figure 37. Same as Figure 36, but for another star occultation. Data and models agree much better than for the case of Figure 36 above 100 km.

of stronger opacity are made of larger particles, as could be expected if they are coated with ice.

7.4.4. Detection of Cloud Layers in the Mesosphere

[113] The notion that carbon dioxide clouds would frequently appear in the Martian mesosphere was suggested on the basis of Mars Pathfinder images of the sky showing bright, bluish morning clouds possibly resulting from CO_2 condensation at high altitude. However, no CO_2 condensate has ever been observed simultaneously with supercold temperatures (i.e., lower than the condensation temperature) until recently. Indeed, SPICAM has just detected the highest clouds ever recorded in the Martian atmosphere at more than 100 km of altitude [*Montmessin et al.*, 2006b] (see Figure 41). Simultaneous retrievals of aerosol and temperature profiles reveal very large portions of atmosphere where CO_2, the main gaseous compound, is supersaturated. This clearly suggests these mesospheric clouds are made of CO_2 ice.

[114] These Martian high altitude clouds match the description of terrestrial noctilucent clouds (NLC) which appear in the mesosphere of the polar regions. Our inferred UV opacities are typically very low (<0.01 when integrated over the vertical) and clouds would probably not be seen from the surface, unless perhaps after sunset or before sunrise when cloud particles can scatter sunlight coming directly from below the horizon. Surprisingly, observed clouds systematically stretch below the supercold zone where they formed. A similar trend is observed for NLCs on Earth with respect to the saturation conditions of water vapor. It is, however, likely that CO_2 ice particles can fall over significant distances into warmer, unsaturated air before their complete sublimation. In a rarefied atmosphere, condensation and sublimation processes are theoretically slower and must therefore compete with the short timescales of sedimentation. Using our estimates on cloud opacity and particle size (about 0.1 μm radius), we can derive a value for the cloud particle population, which is about a few millions per cubic meter on the average. Assuming CO_2 ice particles are formed heterogeneously, then a question stems about the origin of the cloud condensation nuclei. Could they be supplied by a flux of meteoritic debris like on Earth, or by an upward flux of submicronic mineral dust particles stripped from the Martian regolith? Vertical propagation of thermal waves appears only partly buffered by the release of latent heat induced by CO_2 condensation, as illustrated by the recurrent presence of supercold air pockets. As a result, the role played by microphysical processes, which control CO_2 ice particle formation and evolution, is critical in regulating the thermal state of the upper atmosphere. It should be emphasized that, in usual Martian GCM atmospheric models, CO_2 is forced to condense whenever the atmospheric temperature is below the saturation point, which is obviously not the case in reality, as shown by Figure 3 of *Montmessin et al.* [2006b], showing slices of $\sim$10 km thick atmospheric layer with a temperature below the saturation temperature. As a result, the atmosphere above this saturation level is compressed downward in the model: all the densities above this point are lower in the model than in reality. It may be important if aerobraking is used for orbit adjustment of a spacecraft. This is clearly an area where models could be improved.

7.4.5. Dust Particle Size

[115] From the surface of Mars, the observation by the Imager for Mars Pathfinder of solar light scattered as a

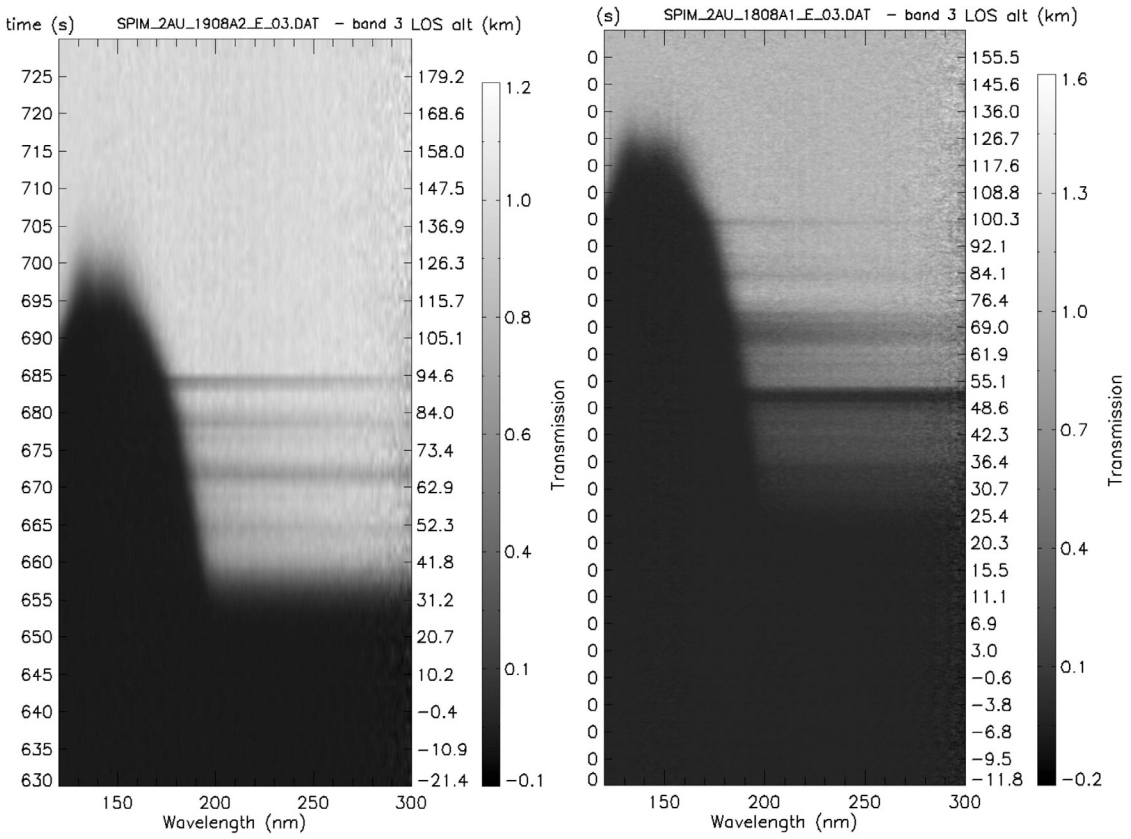

Figure 38. Two examples of star de-occultations (star rising) on the night side showing multilayers of dust or cloud particles, at orbits (left) 1908 and (right) 1808. All recorded spectra have been divided by the star spectrum outside the atmosphere to yield the spectral transmission as a function of time after the star of the observation (left scale) and altitude of the MNP (right scale). On this transmission tempo-spectrum, the CO_2 absorption trough is seen below 200 nm, with a width decreasing with increasing altitude. On these profiles there was no ozone at high altitude.

function of scattering angle allowed determination of the mean size of dust particles and the (variable) vertical optical thickness [*Markiewicz et al.*, 1999]. This was done at several wavelengths in the visible and near IR (from 444 to 965 nm), and resulted in a mean size of about 1.7 μm radius. From the occultation measurements performed with SPICAM, dust particles are found with an effective radius $r_{eff} < 0.1$ μm above 60 km of altitude and at all latitudes [*Montmessin et al.*, 2006a]. Below 50 km, extinction measurements are more difficult to interpret in terms of particle sizes, while solar UV radiation scattered and observed at the limb yields a more precise description of size distribution [*Rannou et al.*, 2006]. In particular, the mean size is found to be in the range from 0.01 to 0.1 μm, at all altitudes above 20 km. It does not mean that larger particles do not exist; but since they are also active in UV, it means that the UV radiation field is totally dominated by small particles, much smaller than the value of 1.7 μm, at least at altitudes >20 km. It is reasonable to think that larger and heavier particles are sedimenting much faster than lighter particles, while uplift by vertical wind is more efficient on small particles than on large particles. These two effects will yield a steady state situation with smaller particles at higher altitudes, as found by SPICAM.

[116] The nature of these tiny particles is not known. It may be nonunique. The recent discovery of clay minerals by OMEGA on the ground of Mars [*Poulet et al.*, 2005] suggests that very fine dust grains could be made of clay, as it happens also on Earth.

8. Ozone: Summary of SPICAM Findings and Future Prospects

8.1. Overview

[117] On Earth, ozone is a by-product of oxygen, which itself is a by-product of life. Ozone protects life from solar UV radiation, a damaging agent of DNA molecules. Early life on Earth was limited to oceans (liquid water is also opaque to UV), and it was not until 500 Myr ago that there was enough O_2 and O_3 in the atmosphere of the Earth for life to creep its way on the continents. In the context of Mars habitability, it is important to characterize the Martian ozone: average quantity, seasonal/latitude variations, diurnal variations, year to year variations, coupling with H_2O and dust. It is also important to understand the detailed mechanisms controlling ozone, from which a full predictive model may be built. In this respect, the unique capability of SPICAM to obtain the ozone vertical distribution is vital. By comparison of the various ozone and H_2O SPICAM

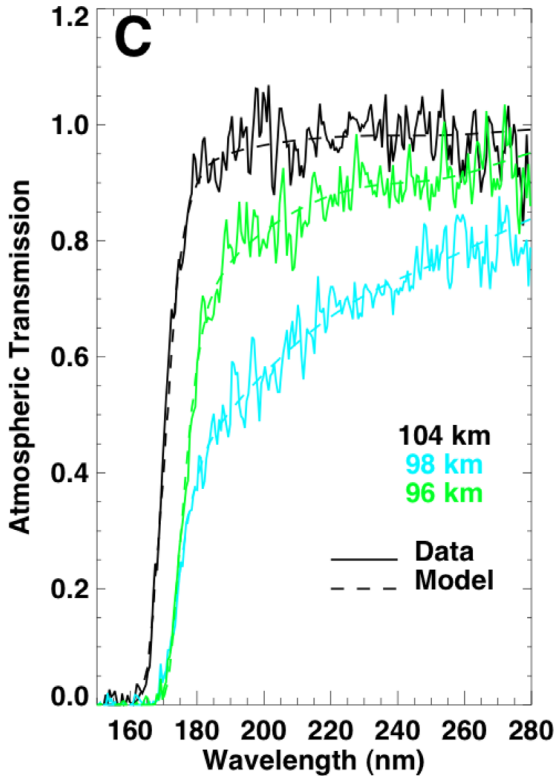

Figure 39. The measured spectral transmission recorded at three altitudes during a stellar occultation is fitted by a simple spectral extinction law, defined by the Angström coefficient. During this occultation, a high-altitude cloud of CO_2 ice particles was detected (see section 7.4.4). The transmission is smaller at 98 km than at 96 km, revealing the presence of the absorbing layer. The spectral slope is also different at the altitude of the cloud.

measurements, models may be validated, and adjusted for a better representation of the results where there are discrepancies. Once fully validated, models can be used to derive some atmospheric constituents which are very difficult or impossible to measure: H_2O_2, HO_x radicals (H, OH, HO_2), O atoms, all oxidizer ingredients impossible to measure remotely (except H_2O_2 [*Encrenaz et al.*, 2004]) and that would be detrimental to living organisms at the surface of Mars. One can also compute directly some quantities from the data: as an example is shown (Figure 42) the actinic UV solar flux reaching the ground of Mars, for the measured maximum quantity of ozone of 25 μm-atm.

[118] On the other hand, studying ozone on Mars is a useful reminder that the catalytic destruction cycle triggered by HOx, which dominates on Mars, is also present in the upper stratosphere of the Earth. It is less important than NOx and ClOx catalytic destruction cycles, because the stratosphere is very dry. With the forthcoming global climatic change, the situation may deteriorate with a warmer tropopause and more H_2O injection in the stratosphere, the source of HOx radicals. Martian research offers the opportunity to study in great detail the ozone equilibrium, and we may find some applications to the case of ozone on Earth; for instance, the importance of heterogeneous chemistry could be assessed more easily on Mars and transposed to Earth.

[119] Ozone was detected for the first time on Mars by the Mariner 7 and 9 UV spectrometers in 1969 and 1971 [*Barth and Hord*, 1971; *Barth et al.*, 1973]. Seasonal variations indicated an anti-correlation with temperature, correctly interpreted as linked to the presence of H_2O, the source of HO_x family, similar to the situation of the Earth upper stratosphere. This was confirmed by 1D photochemical models [e.g., *Parkinson and Hunten*, 1972; *Krasnopolsky*, 1993; *Nair et al.*, 1994]. SPICAM provides the first simultaneous global view of ozone and H_2O, offering a unique opportunity to study directly the detailed coupling between these two species.

[120] The first 3D modeling of ozone on Mars [*Lefèvre et al.*, 2004] included state-of-the-art chemistry, with dynamics provided by the LMD GCM [*Forget et al.*, 1999]. The resulting model distribution of ozone on Mars may be described simply by the existence of two ozone layers, instead of one on Earth. The upper layer in the altitude range 30 to 70 km exists mostly at night [*Lefèvre et al.*, 2004, Figure 4; *Lebonnois et al.*, 2006, Figure 9], and only at certain seasons, when the hygropause is low enough to prevent the scavenging role of HOx radicals (Figures 43a and 43b). Around aphelion season (L_s = 71°), the hygropause is low, and this model ozone nocturnal layer is predicted to be quite stable during all northern spring and summer. When it exists, this layer appears at sunset from recombination of O atoms, but is destroyed by ultraviolet photons when the Sun rises. On the contrary, the lower layer has its maximum density at the surface, and experiences only a weak diurnal cycle. The maximum quantities of ozone are found in the polar regions in winter. A comparison of the model prediction with ozone results obtained previous to SPICAM/MEX, from ground and from limited Hubble Space Telescope [*Clancy et al.*, 1999] is discussed by *Lefèvre et al.* [2004].

[121] SPICAM is using four methods of ozone measurements which are complementary rather than redundant. On the dayside, the strong Hartley absorption band (Figure 29) is imprinted on the solar radiation backscattered from surface, atmosphere, dust and clouds (if any). Only the total vertical column may be retrieved. Therefore this method addresses almost exclusively the lower, surface layer of ozone. Stellar occultations are restricted to the night side; one can probe the upper layer, and the top of the lower layer. The horizontal opacity of dust limits the useful measurements to $z > 20-40$ km, except in some rare occasions (polar night, where the dust load is smaller). The same limitation also applies to solar occultations, which probe ozone at the terminator. One would expect more ozone at sunrise than at sunset. And finally, the 1.27 μm emission is easily measured by SPICAM IR [*Fedorova et al.*, 2006b]. In the atmosphere of Mars, this emission is due to the photo-dissociation of ozone, producing an O_2 molecule in an excited state ($^1\Delta$ O_2), which de-excites spontaneously by emitting a photon at 1.27 μm. However, de-excitation by collisions is a competing mechanism (quenching), preventing the IR emission. It is therefore applicable only to the dayside, with contributions of the upper part of the lower surface layer, and from the upper layer, which is weak on the dayside.

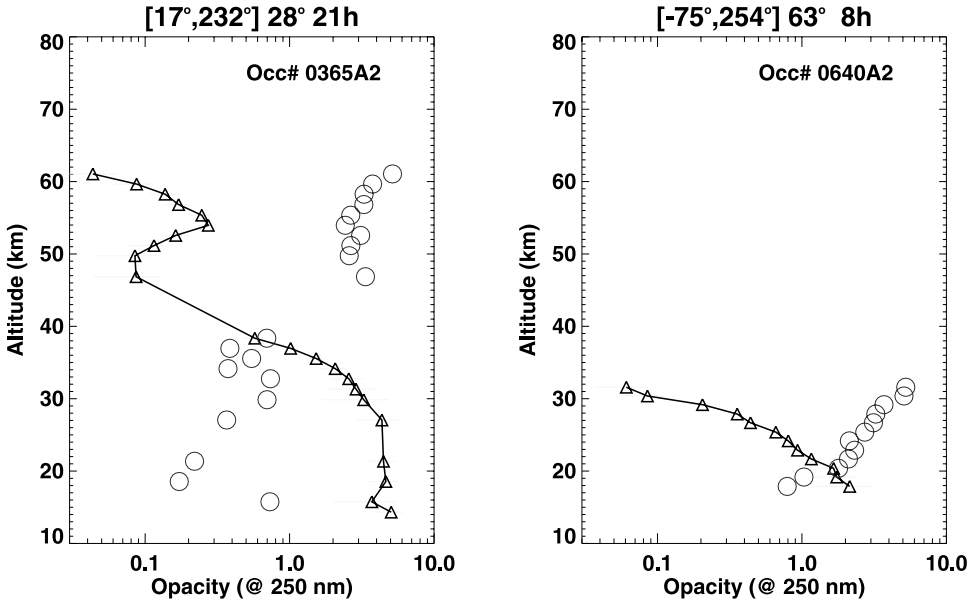

Figure 40. (left) A typical aerosol profile retrieved from SPICAM stellar occultations. Triangles show the aerosol opacity along the line of sight at 250 nm as a function of altitude. Open circles give the value of the Angström coefficient α (opacity varies as $\lambda^{-\alpha}$; α is a parameter indicative of the particle size), same scale as opacity. The higher the coefficient α is, the smaller the particles are. This is a typical profile near the equator, displaying a cloud layer at 50–60 km of small particles ($\alpha \sim 3$). The orbit number is printed in the graph (upper right). Above the plot are indicated the latitude and longitude of occultation point and solar longitude Ls and the local time. (right) Same as Figure 40b, but for a typical profile obtained in the south polar night. The atmosphere is clear above 30 km; dust is much less extended in altitude than at any other place.

[122] In order to get an overview of SPICAM ozone measurements, we will briefly summarize below the results obtained so far by three methods, detailed in companion papers [*Perrier et al.*, 2006; *Lebonnois et al.*, 2006; *Fedorova et al.*, 2006b]. Solar occultation SPICAM data will be presented elsewhere.

8.2. Nadir Looking

[123] Ozone absorption cross section is maximum around 250 nm, showing a broad absorption band with a characteristic shape (Figure 29). This is the Hartley's band, which on Earth protects life from solar UV radiation. On Mars, the ozone absorption is imprinted in the solar UV radiation backscattered by the surface, the gas and atmospheric dust. Because of the highly structured shape of the solar spectrum (Figure 20), it is not easy to evaluate visually the goodness of a fit of the recorded data by a model of what should be seen by SPICAM. Rather, the ratio of two recorded spectra will display much more clearly the absorption of ozone if their ozone content is different. Therefore all SPICAM nadir UV spectra have been divided by a data reference spectrum, to yield an ensemble of relative spectra, to be fitted by a model. This method was also used by *Barth et al.* [1973] for ozone retrieval from Mariner 9 UV spectrometer. The advantage of this "relative" method is to avoid the issue of the exact absolute calibration efficient area S_{eff} and the gain G of the detector, and also the details of the instrument spectral resolution, variable with wavelength.

[124] As explained by *Perrier et al.* [2006], a data reference spectrum is first established by averaging some spectra above the highest mountain, Olympus Mons: it corresponds to an ozone-free atmosphere (according to the CGCM), with a minimal amount of dust and aerosols. Then, all recorded spectra are divided by this reference spectrum to yield relative spectra. This has the advantage to eliminate the response of the instrument and all solar spectral features (see Figure 20), and to emphasize variations of the apparent albedo (ground +atmospheric/dust/cloud contributions), when they exist.

[125] The result of this exercise is shown in Figure 44, as a spectro-temporal image (or tempo-spectrum): each line is a relative spectrum, time is increasing upward, with one line per second. All five bands were averaged together at each second. During this observation, the spacecraft was drifting from low latitudes to high latitudes of northern hemisphere, and the SZA was increasing with latitude. The further north MEX was, the more ozone absorption band at 250 nm appears in the data. The season was early spring ($L_s = 8.6°$), and for the last spectra, the SZA gets closer to 90° and the signal becomes rather low. There is a brighter region at all wavelengths between 45 and 60° of latitude, that we assign to the higher albedo of CO_2 ice. Otherwise, there are no conspicuous variations of the ground albedo, at least at this orbit. The somewhat higher relative apparent albedo at short wavelengths (below 60° latitude) is due to more Rayleigh scattering than at Olympus Mons (reference spectrum).

[126] The total vertical ozone is retrieved [*Perrier et al.*, 2006] by fitting an observed relative spectrum by a model, which includes two free parameters describing the ground albedo, at 220 and 280 nm, with an assumed wavelength

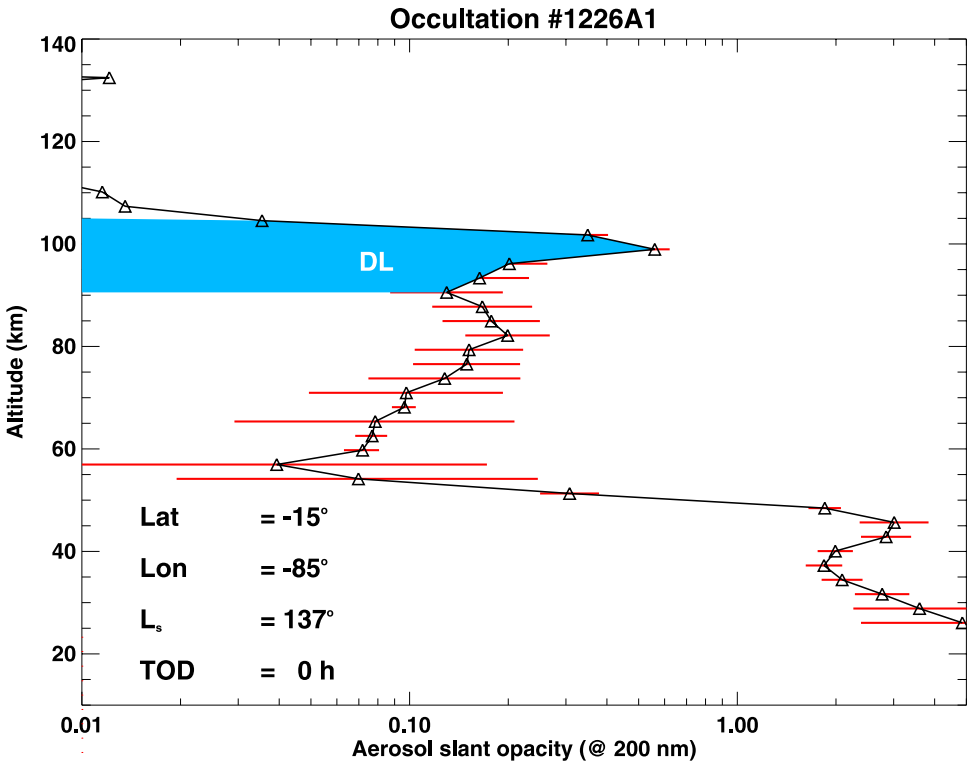

Figure 41. Vertical profile of the aerosol opacity along the line of sight for one occultation sequence at orbit 1226, as a function of the tangent altitude of the LOS (apparent altitude). Optical thickness is given at 200 nm. The vertical extent of the detached layer (DL) is shown for reference, but observation geometry may stretch the image of the layer to altitudes well below its actual lower limit. This high-altitude cloud is interpreted as a CO_2 ice cloud because the temperature profile is very cold, below the condensation of CO_2 [*Montmessin et al.*, 2006a]. Significant diurnal variations can be expected at high altitudes, and clouds may disappear with daylight.

linear dependence in between. At present, observed variations of this albedo reveals ices on the ground, and clouds, rather than mineralogical variations.

[127] A noticeable point on the SPICAM ozone map [*Perrier et al.*, 2006, Figure 11] is the distribution of the available data. Few data are available at high latitudes. This is due both to the large solar zenith angle, and to the need to share observing time with other instruments: SPICAM is usually on at the same time as imagers, favoring the pericenter region, while the high latitudes could only be observed usually far from pericenter. Moreover, there is a lack of data between Ls = 70 and Ls = 90°, related to the period of solar eclipses that decrease power resources. For these various reasons, the coverage in season and latitude is not as complete as desirable. Nonetheless, it is sufficient to describe a number of observed ozone characteristics, and to compare these nadir SPICAM results to the three-dimensional model distribution of ozone of *Lefèvre et al.* [2004]. Detailed comments are given by *Perrier et al.* [2006], with a brief summary below.

[128] The ozone vertical content is found highly variable with season, latitude, geography, and meteorology. It varies from essentially 0 to a maximum of 28 μm-atm. The Martian ozone layer is very thin by Earth standards, corresponding to a maximum of 2.8 Dobson (one Dobson unit = 10 μm-atm), to be compared to a usual Earth's stratosphere value of 300 Dobson units. As a result, the actinic solar flux reaching the ground of Mars in the UV is extremely high (Figure 41) (but the effect of dust for the attenuation of UV flux is not taken into account in this calculation). The season-latitude data map [*Perrier et al.*, 2006, Figure 11] identifies three regions of ozone maxima in the season-latitude map, two near the north poles and one near the South pole. In fact, according to the model map of total ozone of *Lefèvre et al.* [2004], it is clear that the two north pole maxima that we see with SPICAM are connected in time and form only one maximum encompassing Ls = 0 time.

[129] At high latitudes during the ozone seasons (corresponding to winters), there is a large orbit to orbit observed variability. This is also predicted by the model, and due to the irregular shape of the polar vortex, very rich in ozone. The Hellas basin is rich in ozone, as predicted by the model (the lower ozone layer is just thicker, extending at lower altitudes). Detailed comparison data/model will allow us to adjust/improve the models, and therefore the ozone data will be made available to the various modeler groups on request. We may say already that the observed latitude-season variations are well predicted by the model of *Lefèvre et al.* [2004]. However, at high latitudes and when model

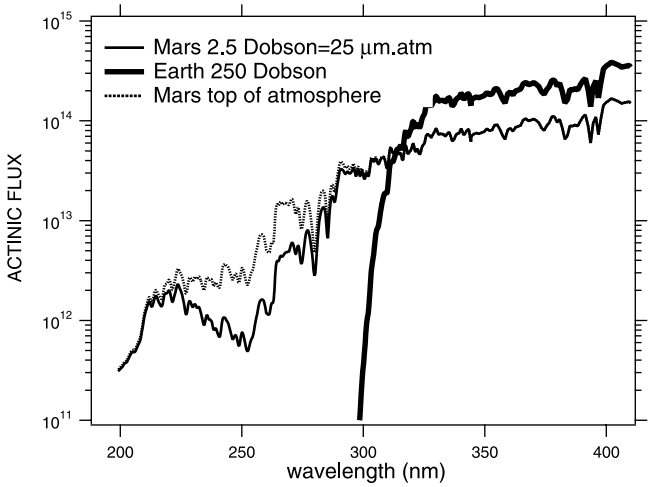

Figure 42. Solar flux in units of photons/(cm^2 s nm) for various cases. Thick solid line: Earth's case with a vertical column of 250 Dobson, SZA = 60°. Solid line: Mars case with 2.5 dobson = 25 μm-atm, the maximum quantity that was found with SPICAM on the day side. Dotted line: at top of Mars atmosphere. This illustrates that ozone on Mars is insufficient to offer a proper protection from solar UV, while on Earth the solar flux is essentially 0 below 300 nm.

predictions of *Lefèvre et al.* [2004] are highest, our measured values are sometimes even higher, in particular in the season Ls = 0–30 (north), and during the southern winter season. Therefore something must be tuned in the model to obtain a better fit to observations.

8.3. Ozone Vertical Profiles From Stellar Occultations

[130] The analysis of atmospheric transmission spectra obtained during stellar occultations yields retrieval of slant densities of CO_2, dust, and ozone, as a function of altitude. Inversion of these vertical profiles allows us to retrieve vertical profiles of local densities, with a resolution in altitude close to 5 km. Ozone results are discussed in detail by *Lebonnois et al.* [2006].

[131] Before Mars Express, there was only one single ozone vertical profile obtained by *Blamont and Chassefière* [1993] by solar occultation on the Phobos 2 mission. The quality was not excellent, partly because the quantity of ozone was low at that local time and season. With the numerous star occultations obtained with SPICAM, on some of them no ozone can be detected, but on some other ones the UV absorption signature is quite conspicuous, as for instance in Figure 45. One limitation is that bright UV stars needed by SPICAM are concentrated near the galactic plane, and the latitude-season sampling is a combination of orbit plane and pericenter drift, resulting in a somewhat uneven sampling.

[132] More than 400 vertical profiles of ozone in the altitude range 20–30 to 70 km were obtained and are analyzed [*Lebonnois et al.*, 2006] as functions of latitude and season (solar longitude) of the observations. The occultations analyzed so far mainly cover southern hemisphere, during autumn and winter (Ls = 8° to 155°). Most of them were taken at night. The upper limit for detection of ozone is a density of roughly 10^8 cm^{-3}, and the error bars are usually of a few 10^8 cm^{-3}, going up to 10^9 cm^{-3} when the profile is especially noisy. The profiles show the presence of the two ozone layers predicted by the model: the upper layer (which exists almost only at night) located in the altitude range 30 to 60 km, which characteristics are highly variable with latitude and season, and the lower, near-surface layer. Because of the dust opacity, low altitudes cannot be reached, and SPICAM can only detect the top of this lower layer, on high-latitudes occultations below 30 km altitude (the amount of dust is found smaller there).

[133] The upper layer is first seen on orbit 247, at Ls = 11°, latitude = 16.8°N with a peak abundance of $(4.7 \pm 0.7) \times 10^8$ cm^{-3} at 52 km altitude. Both north and south of the equator, the ozone abundance at the peak (~45 km altitude) tends to increase from $1–4 \times 10^9$ cm^{-3} until Ls ~ 40°, where it stabilizes around $6–8 \times 10^9$ cm^{-3}. After southern winter solstice (Ls ~ 100°), the peak abundance starts decreasing again, and this ozone layer is no longer detected after Ls ~ 130°, while the model predicts its existence until Ls ~ 175° [*Lebonnois et al.*, 2006]. It seems that the duration of the high-ozone season is shorter than predicted by the model, which implies that season-dependent mechanisms destroying ozone are underestimated in the model. At high latitudes, the ozone amount of the upper layer is also overestimated by the model.

[134] This difference in the seasonal behavior between observations and model may be linked either to the vertical distribution of water vapor and its evolution with season, or to the possible role of heterogeneous chemistry at the surface of dust particles or water ice clouds. SPICAM observations have the potential to explore both hypothesis in more detail in future studies. On some profiles, vertical structures are observed within one of these ozone layers, of uncertain origin, which might be relevant to nonmodeled destruction mechanisms. The observed top altitude and ozone amount of the surface layer is also in general good agreement with the model.

8.4. Oxygen $O_2(^1\Delta_g)$ Emission at 1.27 μm

[135] A strong dayglow 1.27 μm $O_2(^1\Delta_g)$ emission occurs in the Earth's mesosphere, resulting from the photo-dissociation of ozone. On Mars the situation is similar to Earth's mesosphere, and indeed this emission was discovered on Mars from the ground at high spectral resolution by *Noxon et al.* [1976]. SPICAM IR spectrometer of AOTF type has enough spectral resolution to distinguish clearly this emission standing over the solar spectrum continuum backscattered from the ground, as described by *Korablev et al.* [2006]. SPICAM IR routinely observes the $O_2(^1\Delta_g)$ band in nadir and at the limb of Mars, and nadir observations are described by *Fedorova et al.* [2006b]. The intensity may go up to 25 megaRayleigh in the polar regions of the planet. The latitude/season map of this nadir looking intensity show maxima exactly correlated with UV ozone mapping of *Perrier et al.* [2006].

[136] At low altitudes, this O_2 emission is totally or partially quenched by collisions with CO_2 molecules, and it is often admitted that this emission is relevant to ozone above 20 km of altitude. Detailed calculations were, however, performed by *Perrier* [2003], showing that this emission comes also partially from altitudes below 20 km. This low altitude contribution to the near IR emission must

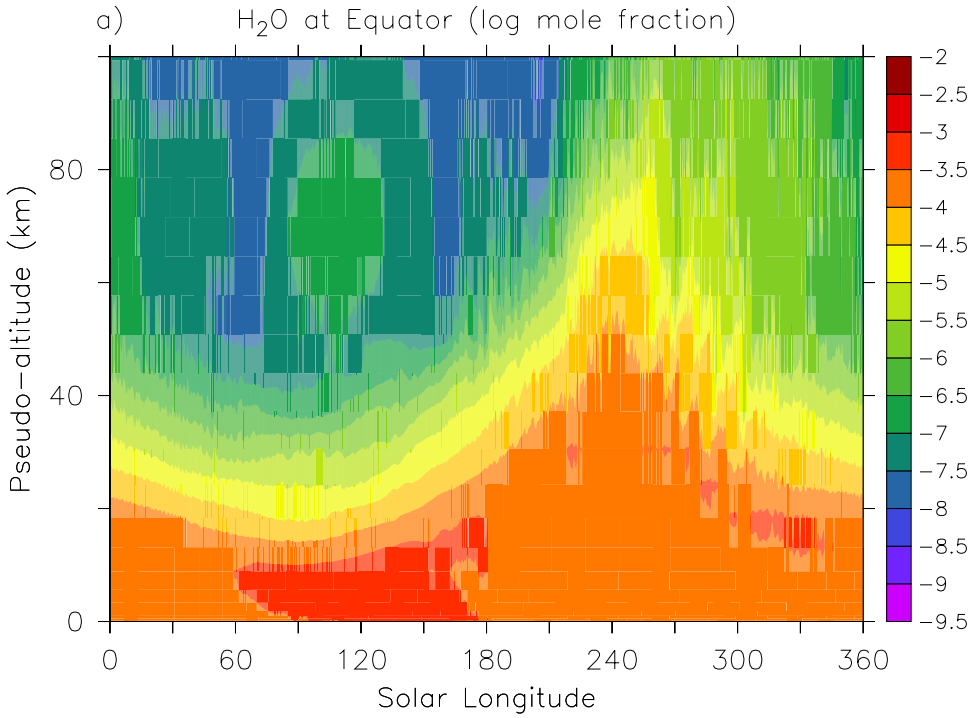

Figure 43a. Evolution of the vertical distribution of H_2O in the General Circulation Model [*Lefèvre et al.*, 2004] at equator, zonally averaged, as a function of solar longitude. The hygropause could be defined as the yellow layer, corresponding to an H_2O mixing ratio between 10^{-4} and $10^{-4.5}$ (adapted from Figure 2a of *Lefèvre et al.* [2004]).

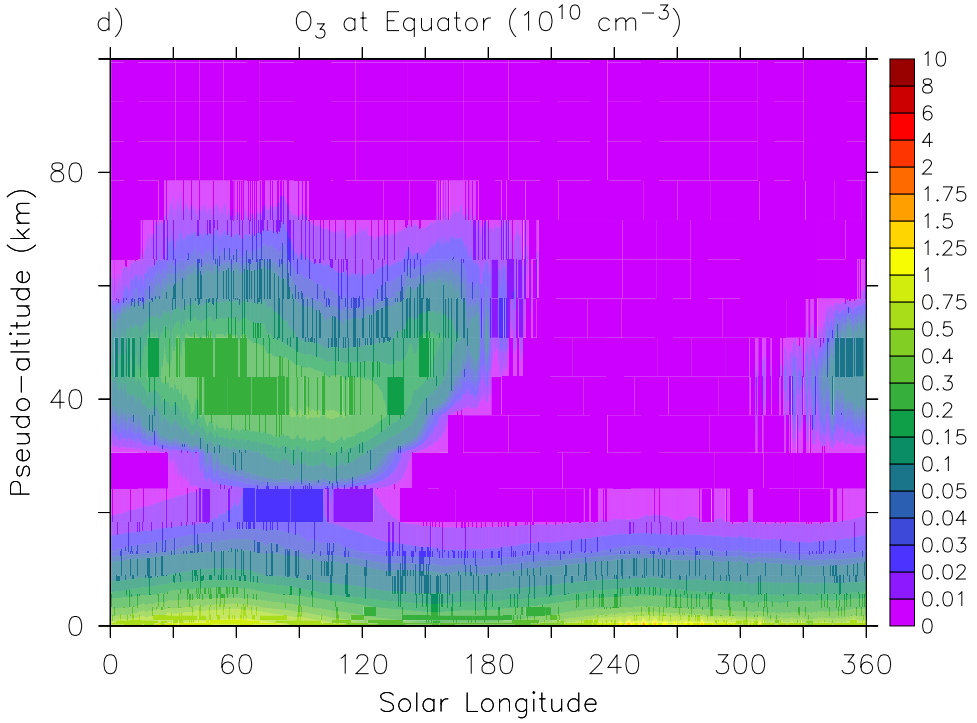

Figure 43b. Evolution of the vertical distribution of ozone in the General Circulation Model [*Lefèvre et al.*, 2004] at equator, zonally averaged, as a function of solar longitude. The upper layer of ozone (30–60 km) is destroyed when water vapor increases at these altitudes (Figure 43a) (adapted from Figure 2d of *Lefèvre et al.* [2004]).

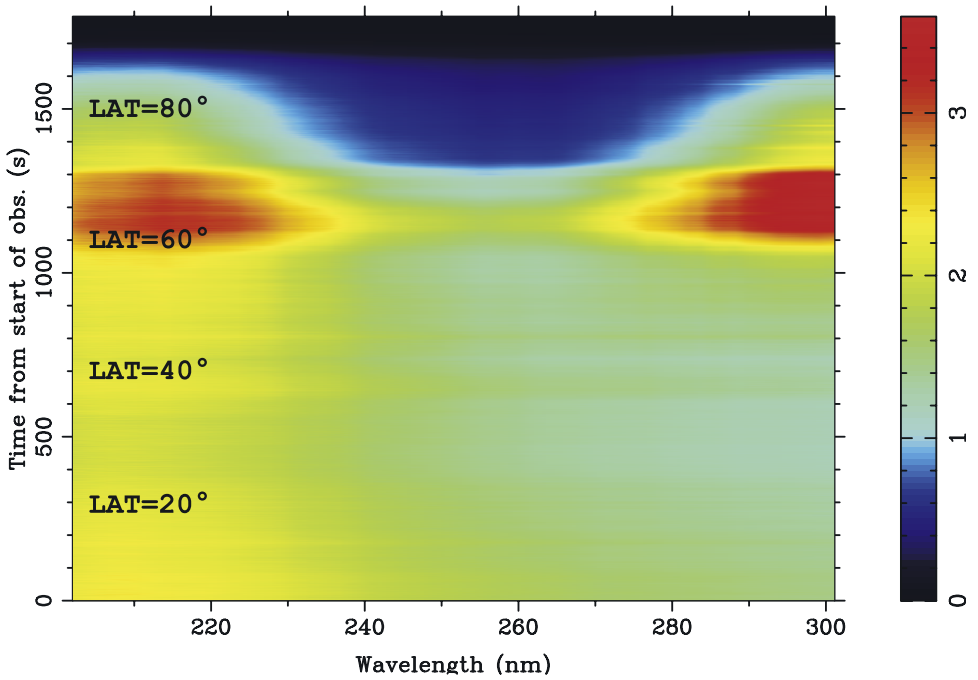

Figure 44. Examples of relative spectra: spectra of orbit 231 divided by the reference spectrum above Olympus Mons. The color code indicates the spectral intensity relative to Olympus Mons Spectrum. The large trough centered at 255 nm is due to ozone absorption. During this observation, the spacecraft is looking from low latitudes of northern hemisphere to high latitudes. The trough depth of ozone absorption band at 250 nm and corresponding ozone quantity is increasing when going north. Note the brighter region at latitudes 45–60°, due to CO_2 or H_2O frost on the surface, increasing the albedo. The further decline at higher latitudes is due to the decrease of SZA angle.

therefore be also taken into account when detailed comparisons of model with data will be made.

9. Conclusions

[137] Several measurements provided by SPICAM are *absolutely unique* and would not be provided otherwise. Some of them are listed here:

[138] 1. The (unexpected, but hoped for) discovery of two types of nightglow: aurora and NO emission, providing insights on magnetic field and upper atmosphere circulation.

[139] 2. SPICAM has collected the first climatology of ozone, both total ozone and vertical distribution with stellar occultations (night side). It is also the first time that ozone is detected from orbit from $O_2(^1\Delta_g)$ at 1.27 μm (day side). The first step of comparison with a sophisticated 3D model is done: the gross features of ozone field are actually well captured by the model, but there are some discrepancies which need to be addressed for further adjustment of the model. Once the model is tuned to reproduce the data (validated), it offers the possibility to calculate with confidence a large number of other species, difficult (H_2O_2) or impossible to measure directly (i.e., HOx radicals), for a full description of the Martian environment (connected to life sustainability and human exploration).

[140] 3. The density/temperature profiles obtained with SPICAM will provide important constraints for building meteorological and dynamical atmospheric models, from the surface to the thermosphere. SPICAM is the only way to access by remote sensing altitudes from 80 km up to 150 km, the region used for aerocapture and aerobraking. As predicted [*Bertaux et al.*, 2000, 2004], stellar occultations gave us a unique chance to detect clouds on the night side, with the discovery of CO_2 condensation clouds at 90 km of altitude.

[141] 4. A new population of small dust particles, with radius 0.01 to 0.1 nm are detected, both in extinction (by occultations) and from scattered solar radiation, at altitudes > 20 km. Much smaller than the dust particles detected from the surface of Mars (1.7 μm), or from orbit in the infra-red, they dominate the UV radiation field, both in extinction and scattering of solar radiation. They must play an important role in the thermal behavior of the atmosphere, at least at $z >$ 20 km.

[142] 5. The remote sensing of the ionosphere from natural emissions, and interaction with the solar wind is not included in planned missions to Mars.

[143] 6. The mapping of H_2O with the AOTF NIR spectrometer is fully demonstrated [*Korablev et al.*, 2006]. With a mass of only 0.75 kg, this instrument should fly as a low-cost passenger on all future missions to Mars.

[144] SPICAM is applying to Mars the most successful methods for the study of Earth's atmosphere: backscatter UV and IR spectroscopy, and solar/stellar occultation limb sounding. One remarkable aspect is the fact that all these results are obtained with a 4.7 kg instrument only. It is fair to say that the success of SPICAM is also due to the design of Mars Express spacecraft, which has a remarkable built-in capability of orientation in any direction (provided that flight rules are respected).

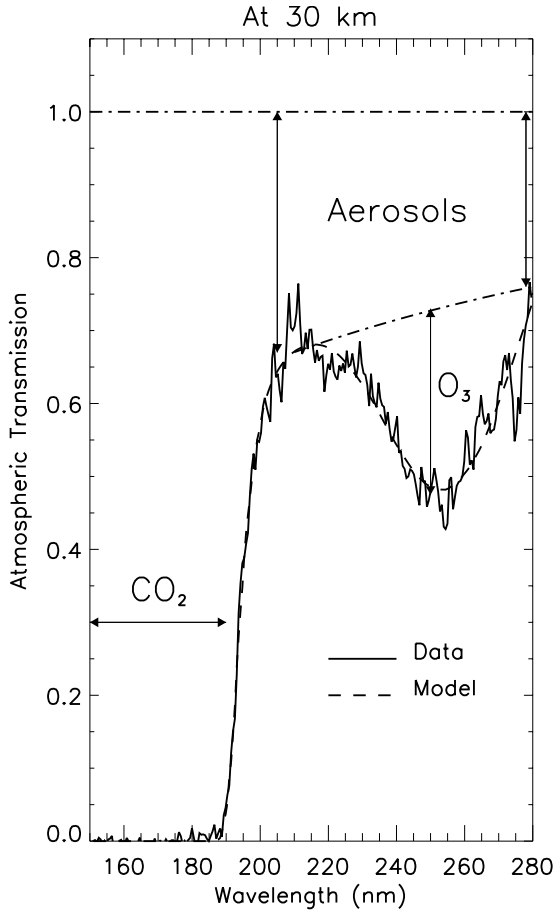

Figure 45. Spectral transmission recorded at 30 km of altitude during polar night (one single 1 s measurement). The ozone absorption trough is well seen, superimposed to the dust continuum above 200 nm of wavelength. Below 190 nm, there is a total absorption by CO_2.

[145] It is already clear that the atmosphere of Mars, as well as of the Earth, experiences a strong interannual variability and the study of the atmosphere of Mars must be pursued at every Mars mission opportunity. The extension of the Mars Express mission for a full second Mars Year is an excellent opportunity, which we hope will be continued further in the future.

[146] **Acknowledgments.** Mars Express is a space mission from ESA (European Space Agency). We wish to express our gratitude to all ESA members who participated in this successful mission, and in particular to Michel Denis and his team at ESOC for the delicate controlling of the spacecraft, René Pischel and Tanja Zeghers at ESTEC for careful planning exercises, and Agustin Chicarro for scientific coordination. We thank also Astrium for the design and construction of the spacecraft and in particular Alain Clochet, responsible for the scientific payload. We thank our collaborators at the three institutes for the design and fabrication of the instrument (Service d'Aéronomie/France, BIRA/Belgium, and IKI/Moscow). We wish to thank CNRS and CNES for financing SPICAM in France. We wish to thank the Space Division of the Belgian Federal Science Policy Office for supporting this project through the ESA PRODEX program. The Russian team acknowledges support of RFFI grant 04-02-16856-a. We express our gratitude to Francis Rocard at CNES and to Eric Villard for special measurements on the second flight model of SPICAM while preparing SPICAV for Venus Express. We have a special thought for Vassilli Ivanovitch Moroz, one of our co-investigators, who promoted so much planetary exploration in USSR and in Russia, and who passed away in 2004. The names and affiliations of the SPICAM team are as follows: Jean-Loup Bertaux (1), O. Korablev (2), D. Fonteyn (3), S. Perrier (1), A. Fedorova(2), F. Montmessin(1), F. Leblanc(1), S. Lebonnois(4), F. Lefèvre, E. Quémerais (1), P. Rannou (1), J. Y. Chaufray(1), F. Forget (4), B. Sandel (5), A. Stern (6), C. Muller (3), E. Dimarellis (1), A. Reberac (1), E. Van Ransbeeck(3), B. Gondet(8), A. Kiselev(2), A. Rodin(2), A. Stepanov(2), Yu. Kalinnikov(2), A. Grigoriev(2), A. Hauchecorne (1), M. Cabane (1), E. Chassefière (1), G. Cernogora (1), A. C. Levasseur-Regourd (1), M. De Maziere (3), E. Neefs (3), P. C. Simon (3), D. Fussen(3), D. Nevejans(3), E. Arijs(3), F. Hourdin (4), O. Talagrand (4), O. Witasse(7), E. Kyrölä(9), J. Tamminen(9). (1) Université de Versailles Saint-Quentin-UVSQ, Service d'Aéronomie du CNRS/IPSL, BP 3 Verrières-le-Buisson, 91371 France; (2) Space Research Institute (IKI), 84/32 Profsoyuznaya, 117810 Moscow, Russia; (3) Belgian Institute for Space Aeronomy, 3 av. Circulaire, B-1180 Brussels, Belgium; (4) Laboratoire de Météorologie Dynamique, 4 place Jussieu, 75252 Paris Cedex 05, Paris, France; (5) Lunar and Planetary Laboratory, Univ. of Arizona, 1541 E. University Blvd., Tucson, AZ 85721, USA; (6) South-West Research Institute, Geophys., Astrophys., and Planet. Sci., 1050 Walnut Ave., Suite 400, Boulder, CO 80302-5143, USA; (7) ESTEC/SCI-SR postbus 299, 2200 AG Noordwijk, NL, Europe; (8) Institut d'Astrophysique Spatiale, Orsay Campus, 91405, France; (9) Finnish Meteorological Institute, P.O. Box 503 Fin-00101 Helsinki, Finland.

References

Acuña, M. H., et al. (2001), Magnetic field of Mars: Summary of results from the aerobraking and mapping orbits, *J. Geophys. Res.*, *106*, 23,403–23,417.

Barth, C. A., and C. W. Hord (1971), Mariner ultraviolet spectrometer: Topography and polar cap, *Science*, *173*, 197–201.

Barth, C. A., J. B. Pearce, K. K. Kelly, L. Wallace, and W. G. Fastie (1967), Ultraviolet emissions observed near Venus from Mariner V, *Science*, *158*, 1675–1678.

Barth, C. A., C. W. Hord, J. B. Pearce, K. K. Kelly, G. P. Anderson, and A. I. Stewart (1971), Mariner 6 and 7 ultraviolet spectrometer experiment: Upper atmosphere data, *J. Geophys. Res.*, *76*, 2213–2227.

Barth, C. A., C. W. Hord, A. I. Stewart, A. L. Lane, M. L. Duck, and G. P. Anderson (1973), Mariner 9 ultraviolet spectrometer experiment: Seasonal variation of ozone on Mars, *Science*, *179*, 795–796.

Barth, C. A., A. I. F. Stewart, S. W. Bougher, D. M. Hunten, S. J. Bauer, and A. F. Nagy (1992), Aeronomy of the current Martian atmosphere, in *Mars*, edited by H. H. Kieffer et al., Univ. of Ariz. Press, Tucson.

Bertaux, J.-L., et al. (2000), The study of the Martian atmosphere from top to bottom with SPICAM Light on Mars Express, *Planet. Space Sci.*, *48*, 1303–1320.

Bertaux, J.-L., et al. (2004), SPICAM Light: An experiment to study the global structure and composition of the Martian atmosphere, in *Mars Express—The Scientific Payload*, *Eur. Space Agency Spec. Publ.*, *ESA-SP 1240*, 95–120.

Bertaux, J.-L., et al. (2005a), First observation of nightglow in the upper atmosphere of Mars: The NO bands in UV and implications for atmospheric transport, *Science*, *307*, 566–569.

Bertaux, J.-L., F. Leblanc, O. Witasse, E. Quémerais, J. Lilensten, A. S. Stern, B. Sandel, and O. Korablev (2005b), Discovery of aurora on Mars, *Nature*, *435*, 790–794.

Bibring, J. P., et al. (2004), Perennial water ice identified in the south polar cap of Mars, *Nature*, *428*, 627–630.

Blamont, J. E., and E. Chassefière (1993), First detection of ozone in the middle atmosphere of Mars from solar occultation measurements, *Icarus*, *104*, 324–336.

Blamont, J. E., E. Chassefière, J. P. Goutail, B. Mege, M. Nunes-Pinharanda, G. Soushon, V. A. Krasnopolsky, A. A. Krysko, and V. I. Moroz (1989), Vertical structure of dust and ozone in the Martian atmosphere deduced from solar occultation measurements, *Nature*, *341*, 600–603.

Bougher, S. W., R. G. Roble, E. C. Ridley, and R. E. Dickinson (1990), The Mars thermosphere: 2. General circulation with coupled dynamics and composition, *J. Geophys. Res.*, *95*, 14,811–14,827.

Chassefière, E., J. E. Blamont, V. A. Krasnopolsky, O. I. Korablev, S. K. Atreya, and R. A. West (1992), Vertical structure and size distributions of Martian aerosols from solar occultation measurements, *Icarus*, *97*, 46–69.

Chaufray, J.-Y., R. Modolo, F. Leblanc, and G. Chanteur (2005), Non thermal oxygen escape at Mars at low and high solar activities, paper presented at IAGA 2005 Sci. Assemb., Int. Assoc. of Geomagn. and Aeron., Toulouse, France.

Clancy, R. T., D. O. Muhleman, and G. L. Berge (1989), Global changes in the 0–70 km thermal structure of the Mars atmosphere derived from 1975 to 1989 microwave CO spectra, *J. Geophys. Res.*, *95*, 14,543–14,554.

Clancy, R. T., A. W. Grossman, M. J. Wolff, P. B. James, D. J. Rudy, Y. N. Billawala, B. J. Sandor, S. W. Lee, and D. O. Muhleman (1996), Water

vapor saturation at low altitudes around Mars aphelion: A key to Mars climate?, *Icarus*, *122*, 36–62.
Clancy, R. T., M. J. Wolff, and P. B. James (1999), Minimal aerosol loading and global increases in atmospheric ozone during the 1996–1997 Martian northern spring season, *Icarus*, *138*, 49–63.
Conrath, B. J., J. C. Pearl, M. D. Smith, and P. R. Christensen (1998), MGS TES results: Characterization of the Martian atmospheric thermal structure, paper presented at 30th Annual Meeting of the Division for Planetary Sciences, Madison, Wisc.
Conrath, B. J., J. C. Pearl, M. D. Smith, and P. R. Christensen (1999), Mars Global Surveyor TES results: Atmospheric thermal structure retrieved from limb measurements, paper presented at 31st Annual Meeting of the Division for Planetary Sciences, Padua, Italy.
Encrenaz, T., B. Bézard, T. K. Greathouse, M. J. Richter, J. H. Lacy, S. K. Atreya, A. S. Wong, S. Lebonnois, F. Lefèvre, and F. Forget (2004), Hydrogen peroxide on Mars: Evidence for spatial and seasonal variations, *Icarus*, *170*, 424–429.
Fedorova, A., O. Korablev, J.-L. Bertaux, A. Rodin, A. Kiselev, and S. Perrier (2006a), Mars water vapor abundance from SPICAM IR spectrometer: Seasonal and geographic distributions, *J. Geophys. Res.*, *111*, E09S08, doi:10.1029/2006JE002695.
Fedorova, A., O. Korablev, S. Perrier, J.-L. Bertaux, F. Lefevre, and A. Rodin (2006b), Observation of O_2 1.27 μm dayglow by SPICAM IR: Seasonal distribution for the first Martian year of Mars Express, *J. Geophys. Res.*, *111*, E09S07, doi:10.1029/2006JE002694.
Feldman, P. D., H. W. Moos, J. T. Clarke, and L. Lane (1979), Identification of the UV nightglow from Venus, *Nature*, *279*, 221–222.
Forget, F., F. Hourdin, and O. Talagrand (1996), Simulation of the Martian atmospheric polar warming with the LMD general circulation model, *Ann. Geophys.*, *14*, C797.
Forget, F., F. Hourdin, R. Fournier, C. Hourdin, O. Talagrand, M. Collins, S. R. Lewis, P. L. Read, and J. Huot (1999), Improved general circulation models of the Martian atmosphere from the surface to above 80 km, *J. Geophys. Res.*, *104*(E10), 24,155–24,176.
Forget, F., S. Lebonnois, M. Angelats i Coll, E. Quémerais, J. L. Bertaux, F. Montmessin, E. Dimarellis, A. Reberac, M. Lopez-Valverde, and F. Gonzalez Galindo (2006), Mars atmosphere density and temperature between 50 and 130 km observed by Mars Express SPICAM stellar occultation, paper presented at Second International Workshop on Mars Atmosphere Modelling and Observations, Cent. Natl. d'Etudes Spatiales, Granada, Spain, March.
Guibert, S. (2005), Applications de la spectroscopie à l'étude de l'atmosphère de Mars et à la recherche de planètes extra-solaires, Ph.D. thesis, Univ. Paris 6–Pierre et Marie Curie, Paris, 17 Oct.
Hapke, B. (1981), Bidirectional reflectance spectroscopy: 1. Theory, *J. Geophys. Res.*, *86*, 3039–3054.
Hauchecorne, A., et al. (2005), First simultaneous global measurements of nighttime stratospheric NO_2 and NO_3 observed by Global Ozone Monitoring by Occultation of Stars (GOMOS)/Envisat in 2003, *J. Geophys. Res.*, *110*, D18301, doi:10.1029/2004JD005711.
Hinson, D. P., R. A. Simpson, J. D. Twicken, G. L. Tyler, and F. M. Flasar (1999), Initial results from radio occultation measurements from Mars Global Surveyor, *J. Geophys. Res.*, *104*(E11), 26,997–27,012.
Keating, G. M., et al. (1998), The structure of the upper atmosphere of Mars: In situ accelerometer measurements from Mars Global Surveyor, *Science*, *279*, 1672–1676.
Keating, G. M., M. Theriot, R. Tolson, S. Bougher, F. Forget, and J. Forbes (2003), Global measurement of the Mars upper atmosphere: In-situ accelerometer measurements from Mars Odyssey 2001 and Mars Global Surveyor, *Lunar Planet. Sci.*, *XXXIV*, Abstract 1142.
Korablev, O. I., V. A. Krasnopolsky, A. V. Rodin, and E. Chassefière (1993), Vertical structure of Martian dust measured by the solar occultation from Phobos spacecraft, *Icarus*, *102*, 76–87.
Korablev, O. I., J.-L. Bertaux, and J. P. Dubois (2001), Occultation of stars in the UV: Study of the atmosphere of Mars, *J. Geophys. Res.*, *106*, 7597–7610.
Korablev, O., et al. (2006), SPICAM IR acousto-optic spectrometer experiment on Mars Express, *J. Geophys. Res.*, *111*, E09S03, doi:10.1029/2006JE002696.
Krasnopolsky, V. A. (1993), Photochemistry of the Martian atmosphere (mean conditions), *Icarus*, *101*, 313–332.
Krasnopolsky, V. A., et al. (1989), Phobos-2: Solar occultation spectroscopic measurements of the Martian atmosphere at 1.9 and 3.7 μm, *Nature*, *341*, 603–604.
Krasnopolsky, V. A., O. I. Korablev, V. I. Moroz, A. A. Krysko, J. E. Blamont, and E. Chassefière (1991), Infrared solar occultation sounding of the Martian atmosphere by the Phobos spacecraft, *Icarus*, *94*, 32–44.
Leblanc, F., and R. E. Johnson (2001), Sputtering of the Martian atmosphere by solar wind pick-up ions, *Planet. Space Sci.*, *49*, 645–656.
Leblanc, F., J. Y. Chaufray, J. Lilensten, O. Witasse, and J.-L. Bertaux (2006), Martian dayglow as seen by the SPICAM UV spectrograph on Mars Express, *J. Geophys. Res.*, *111*, E09S11, doi:10.1029/2005JE002664.
Lebonnois, S., E. Quémerais, F. Montmessin, F. Lefèvre, S. Perrier, J.-L. Bertaux, and F. Forget (2006), Vertical distribution of ozone on Mars as measured by SPICAM/Mars Express using stellar occultations, *J. Geophys. Res.*, *111*, E09S05, doi:10.1029/2005JE002643.
Lefèvre, F., S. Lebonnois, F. Montmessin, and F. Forget (2004), Three-dimensional modeling of ozone on Mars, *J. Geophys. Res.*, *109*, E07004, doi:10.1029/2004JE002268.
Magalhães, J. A., J. T. Schofield, and A. Seiff (1999), Results of the Mars Pathfinder atmospheric structure investigation, *J. Geophys. Res.*, *104*, 8943–8955.
Markiewicz, W. J., R. M. Sablotny, H. U. Keller, N. Thomas, D. Titov, and P. H. Smith (1999), Optical properties of the Martian aerosols as derived from Imager for Mars Pathfinder midday sky brightness data, *J. Geophys. Res.*, *104*, 9009–9017.
Modolo, R., J.-Y. Chaufray, G. M. Chanteur, and F. Leblanc (2005), Response of the Martian environment to an IMF variation and influence of the solar EUV flux, paper presented at IAGA 2005 Sci. Assemb., Int. Assoc. of Geomagn. and Aeron., Toulouse, France.
Montmessin, F., E. Quémerais, J. L. Bertaux, O. Korablev, P. Rannou, and S. Lebonnois (2006a), Stellar occultations at UV wavelengths by the SPICAM instrument: Retrieval and analysis of Martian haze profiles, *J. Geophys. Res.*, *111*, E09S09, doi:10.1029/2005JE002662.
Montmessin, F., et al. (2006b), Sub-visible CO_2 ice clouds detected in the mesosphere of Mars, *Icarus*, *183*, 403–410.
Nair, H., M. Allen, A. D. Anbar, and Y. L. Yung (1994), A photochemical model of the Martian atmosphere, *Icarus*, *111*, 124–150.
Noxon, J. F., W. A. Traub, N. P. Carleton, and P. Connes (1976), Detection of O_2 airglow emission from Mars and the Martian ozone abundance, *Astrophys. J.*, *207*, 1025–1035.
Owen, T., K. Biemann, D. R. Ruschnek, J. E. Biller, D. W. Howarth, and A. L. Lafleur (1977), The composition of the atmosphere at the surface of Mars, *J. Geophys. Res.*, *82*, 4635–4639.
Parkinson, T. D., and D. M. Hunten (1972), Spectroscopy and aeronomy of O_2 on Mars, *J. Atmos. Sci.*, *29*, 1380–1390.
Perrier, S. (2003), L'ozone dans l'atmosphère martienne: Etude de l'émission infra-rouge et de l'absorption dans l'UV proche, stage de DEA Astrophysique et Instrumentations Associées, internal publication, Serv. d'Aéron. du CNRS, Verrières-le-Buisson, France.
Perrier, S., J. L. Bertaux, F. Lefèvre, S. Lebonnois, O. Korablev, A. Fedorova, and F. Montmessin (2006), Global distribution of total ozone on Mars from SPICAM/MEX UV measurements, *J. Geophys. Res.*, *111*, E09S06, doi:10.1029/2006JE002681.
Poulet, F., J.-P. Bibring, J. F. Mustard, A. Gendrin, N. Mangold, Y. Langevin, R. E. Arvidson, B. Gondet, C. Gomez, and the Omega Team (2005), Phyllosilicates on Mars and implications for the early Mars history, *Nature*, *438*, 623–627.
Quémerais, E., and J.-L. Bertaux (2002), Radiometric calibration of the SWAN instrument, in *The Radiometric Calibration of SOHO*, *ISSI Sci. Rep. SR-002*, edited by A. Pauluhn, M. C. E. Huber, and R. von Steiger, pp. 203–209, Int. Space Sci. Inst., Bern.
Quémerais, E., J.-L. Bertaux, O. Korablev, E. Dimarellis, C. Cot, B. R. Sandel, and D. Fussen (2006), Stellar occultations observed by SPICAM on Mars Express, *J. Geophys. Res.*, *111*, E09S04, doi:10.1029/2005JE002604.
Rannou, P., S. Perrier, J.-L. Bertaux, F. Montmessin, O. Korablev, and A. Rébérac (2006), Dust and cloud detection at the Mars limb with UV scattered sunlight with SPICAM, *J. Geophys. Res.*, *111*, E09S10, doi:10.1029/2006JE002693.
Rodin, A. V., O. I. Korablev, and V. I. Moroz (1997), Vertical distribution of water in near-equatorial troposphere of Mars: Water vapor and clouds, *Icarus*, *125*, 21–29.
Rodin, A. V., R. T. Clancy, and R. J. Wilson (1999), Dynamical properties of Mars water ice clouds and their interactions with atmospheric dust and radiation, *Adv. Space Res.*, *23*, 1577–1585.
Roscoe, H. K., R. A. Freshwater, R. Wolfenden, R. L. Jones, D. J. Fish, J. E. Harries, and D. J. Oldham (1994), Using stars for remote sensing of the Earth's stratosphere, *Appl. Opt.*, *33*, 7126–7131.
Sandel, B. R., and A. L. Broadfoot (1986), Statistical performance of the intensified charge coupled device, *Appl. Opt.*, *25*, 4135–4140.
Seiff, A., and D. B. Kirk (1977), Structure of the atmosphere of Mars in summer in mid-latitudes, *J. Geophys. Res.*, *82*, 4364–4378.
Smith, G. R., and D. M. Hunten (1990), Study of planetary atmospheres by absorptive occultations, *Rev. Geophys.*, *28*, 117–143.
Stewart, A. I. F., and C. A. Barth (1979), Ultraviolet night airglow of Venus, *Science*, *205*, 59–62.
Stewart, A. I. F., C. A. Barth, C. W. Hord, and A. L. Lane (1972), Mariner 9 Ultraviolet Spectrometer Experiment: Structure of Mars' upper atmosphere, *Icarus*, *17*, 469–474.

Stewart, A. I. F., D. E. Anderson Jr., L. W. Esposito, and C. A. Barth (1979), Ultraviolet spectroscopy of Venus: Initial results from the Pioneer Venus orbiter, *Science*, *203*, 777–779.

Wilson, R. J. (1997), A general circulation model simulation of the Mars polar warming, *Geophys. Res. Lett.*, *24*, 123–126.

Wuttke, M. W., H. U. Keller, W. J. Markiewicz, E. Petrova, K. Richter, and N. Thomas (1997), Properties of dust in the Mars atmosphere: A revised analysis of Phobos/KRFM data, *Planet. Space Sci.*, *45*, 281–288.

J.-L. Bertaux, J. Y. Chaufray, E. Dimarellis, F. Leblanc, F. Lefèvre, F. Montmessin, S. Perrier, E. Quémerais, P. Rannou, and A. Reberac, Université de Versailles Saint-Quentin-UVSQ, Service d'Aéronomie du CNRS/IPSL, BP 3, F-91371 Verrières-le-Buisson, France. (bertaux@aerov.jussieu.fr)

A. Fedorova and O. Korablev, Space Research Institute (IKI), 84/32 Profsoyuznaya, 117810 Moscow, Russia.

D. Fonteyn, Belgian Institute for Space Aeronomy, 3 Avenue Circulaire, B-1180 Brussels, Belgium.

F. Forget and S. Lebonnois, Laboratoire de Météorologie Dynamique, 4 Place Jussieu, F-75252 Paris Cedex 05, France.

S. Guibert, Planetarium de Strasbourg, Rue de l'Observatoire, F-67000 Strasbourg, France.